

# High-Fidelity Multidisciplinary Sensitivity Analysis for Coupled Fluid-Solid Interaction Design

A Dissertation submitted in partial fulfillment  
of the requirements for the degree of  
Doctor of Philosophy

by

Koorosh Gobal  
B.S.M.E., Sharif University of Technology, 2012

2016  
Wright State University

Wright State University  
COLLEGE OF GRADUATE STUDIES

October 5, 2016

**I HEREBY RECOMMEND THAT THE DISSERTATION PREPARED UNDER MY SUPERVISION BY Koorosh Gobal ENTITLED High-Fidelity Multidisciplinary Sensitivity Analysis for Coupled Fluid-Solid Interaction Design BE ACCEPTED IN PARTIAL FULFILLMENT OF THE REQUIREMENTS FOR THE DEGREE OF Doctor of Philosophy.**

---

Ramana V. Grandhi, Ph.D.  
Dissertation Director

---

Frank W. Ciarallo, Ph.D.  
Director, Ph.D. in Engineering Program

---

Robert E.W. Fyffe, Ph.D.  
Vice President for Research and  
Dean of the Graduate School

Committee on  
Final Examination

---

Ramana V. Grandhi, Ph.D.

---

Mitch Wolff, Ph.D.

---

Ha-Rok Bae, Ph.D.

---

Robert A. Canfield, Ph.D.

---

Raymond M. Kolonay, Ph.D.

---

Christopher M. Koehler, Ph.D.

## ABSTRACT

Gobal, Koorosh. Ph.D., Department of Mechanical Engineering, Wright State University, 2016.  
*High-Fidelity Multidisciplinary Sensitivity Analysis for Coupled Fluid-Solid Interaction Design.*

In many engineering disciplines such as aerospace, marine, automotive, and biomedical engineering, the consideration of the coupling between the fluid and structural systems is necessary for quality engineering analysis. Therefore, the need for such analysis in the design is continuously increasing. The primary motivation for this work is to develop a sensitivity analysis tool that is capable of calculating accurate sensitivities without significant modification of the source codes for simulations based on non-body conformal grids. The majority of work done on the coupled fluid-solid simulations are based on computational grids that conform to solid boundaries. This becomes a restriction for complex boundary shapes or large deformation of the solid domain. The hurdles associated with body-conformal techniques are mainly due to additional cost related to mesh deformation and the effect of mesh movement on the sensitivity calculation. Therefore, we propose to use a particular family of non-body conformal techniques often known as Immersed Boundary (IB) methods for modeling the flow over immersed boundaries. The Continuum Sensitivity Analysis (CSA) is added on top of the IB method which calculates the sensitivity of the flow variables, velocity, and pressure. These variables are modeled with Navier-Stokes (NS) equations and their sensitivities are calculated with respect to change in the shape of the solid boundary. This technique is implemented in the calculation of the sensitivity of the coupled fluid-structure system subject to different shape design variables. The sensitivity of various coupled FSI benchmark problems such as vortex induced vibration of an elastically mounted cylinder and pitch and plunge airfoil motion is calculated with respect to shape parameters. These results are verified using the complex step method which gives accurate sensitivities up to machine precision. This work is the first implementation of CSA for continuous IB methods for viscous flow (Navier-Stokes) models.

# Contents

<b>1</b>	<b>Introduction</b>	<b>1</b>
1.1	Motivation . . . . .	1
1.2	Literature Review . . . . .	3
1.2.1	Sensitivity Analysis . . . . .	3
1.2.2	Immersed Boundary Method . . . . .	11
1.2.3	Sensitivity Analysis for IB Method . . . . .	15
1.3	Research Contribution . . . . .	16
<b>2</b>	<b>Design Sensitivity Analysis</b>	<b>18</b>
2.1	General Formulation . . . . .	18
2.2	Benchmark Cases . . . . .	20
2.2.1	Heat transfer benchmark case . . . . .	21
2.2.2	Solid mechanics benchmark case . . . . .	22
2.3	Discrete Sensitivity Analysis . . . . .	23
2.3.1	Formulation . . . . .	23
2.3.2	Implementation on heat transfer problem . . . . .	24
2.3.3	Implementation on solid mechanics problem . . . . .	28
2.4	Continuum Sensitivity Analysis . . . . .	32
2.4.1	Formulation . . . . .	32
2.4.2	Implementation on heat transfer problem . . . . .	37
2.4.3	Implementation on solid mechanics problem . . . . .	41
2.5	Summary . . . . .	42
<b>3</b>	<b>Immersed Boundary Method</b>	<b>44</b>
3.1	Introduction . . . . .	45
3.2	Governing Equations . . . . .	47
3.3	Fluid Dynamics Benchmark Case . . . . .	48
3.4	Immersed Boundary Classification . . . . .	50
3.5	Discrete Forcing Method . . . . .	51
3.5.1	Indirect Forcing Method . . . . .	51
3.5.2	Direct Forcing Method . . . . .	55
3.6	Continuum Forcing Method . . . . .	62

3.6.1	Classical IB Method . . . . .	65
3.6.2	Virtual Boundary Method . . . . .	71
3.6.3	Penalization Method . . . . .	76
3.7	Application in Continuum Sensitivity Analysis . . . . .	83
3.8	Summary . . . . .	84
<b>4</b>	<b>Shape Sensitivity Analysis Using Immersed Boundary Method</b>	<b>86</b>
4.1	Regularized Heaviside/Delta Function . . . . .	88
4.2	Sensitivity Analysis Formulation . . . . .	93
4.3	Shape Sensitivity Analysis for 1D problem . . . . .	97
4.4	Shape Sensitivity of Flow Over a Cylinder . . . . .	107
4.5	Shape Sensitivity of Flow through a Nozzle . . . . .	116
4.6	Summary . . . . .	121
<b>5</b>	<b>Shape Sensitivity Analysis for Coupled Fluid-Structure Interaction Design</b>	<b>123</b>
5.1	Fluid-Structure Interaction . . . . .	124
5.1.1	Governing Equations . . . . .	126
5.1.2	Multidisciplinary Coupling . . . . .	127
5.2	Multidisciplinary Shape Sensitivity Analysis . . . . .	129
5.3	Demonstration Cases . . . . .	131
5.3.1	Vortex Induced Vibration . . . . .	131
5.3.2	Pitch and Plunge Airfoil Motion . . . . .	139
5.3.3	Flapping and Bending of a Monofin . . . . .	146
5.4	Summary . . . . .	150
<b>6</b>	<b>Summary Remarks and Future work</b>	<b>152</b>
6.1	Research Contribution . . . . .	154
6.2	Future Work . . . . .	155
<b>Bibliography</b>		<b>157</b>

# List of Figures

1.1	Sensitivity calculation techniques. . . . .	3
1.2	Example of conforming and nonconforming meshes. . . . .	12
1.3	Modified mesh near the solid boundary for cut-cell method. . . . .	15
2.1	General computational domain $\Omega$ with boundary $\Gamma$ . . . . .	19
2.2	One dimensional domain with heat conduction. . . . .	21
2.3	Axial bar under distributed loading. . . . .	22
2.4	One dimensional computational domain for the heat conduction problem. .	25
2.5	Comparison between the analytical and finite difference solutions for 1D heat equation for different number of nodes. . . . .	26
2.6	Comparison between discrete sensitivity analysis and analytical results for different number of nodes. . . . .	28
2.7	Changing the bar length by fixing the interior computational nodes and only moving the boundary (red) node. Node numbers are represented by $i$ and element numbers by $(i)$ . . . . .	29
2.8	Mesh convergence of the finite elements analysis for axial bar. . . . .	30
2.9	Mesh convergence of the discrete sensitivity analysis for the axial bar. .	32
2.10	Comparison between continuum sensitivity analysis and analytical results for different number of nodes. . . . .	40
2.11	Mesh convergence of the continuum (CSA) and discrete (DSA) sensitivity equations for axial bar problem. The results for the convergence of the analysis (FEA) is also included in this graph. . . . .	42
3.1	1D benchmark case for IB method. . . . .	49
3.2	Indirect forcing approach for boundary representation. Desired velocity values at nodes 1 and 2 are interpolated from wall velocity and results from nodes 3 and 4. . . . .	52
3.3	Comparison between IB and analytical results for different wall locations. .	53
3.4	Comparison between IB and analytical results for different number of nodes.	54
3.5	Comparison between IB and analytical results for different wall velocities. .	55
3.6	Nodes representation in the vicinity of an immersed boundary used in the ghost-cell approach. . . . .	56

3.7	Discretized domain for the ghost cell IB method where the “wall” is represented using hashed box. . . . .	57
3.8	Comparison between IB and analytical results for different number of nodes. . . . .	60
3.9	Comparison between IB and analytical results for different wall locations. . . . .	61
3.10	Comparison between IB and analytical results for different wall velocities. . . . .	62
3.11	Comparison between different formulations of $\phi$ . . . . .	65
3.12	Comparison between IB and analytical results for different number of nodes and delta functions for Couette flow problem. . . . .	68
3.13	Comparison between IB and analytical results for different wall velocities. . . . .	70
3.14	Comparison between IB and analytical results for different wall stiffness values. . . . .	71
3.15	Comparison between IB and analytical results for different number of nodes. . . . .	74
3.16	Comparison between IB and analytical results for different wall velocities. . . . .	75
3.17	Comparison between IB and analytical results for different values for constants $\alpha$ and $\beta$ . . . . .	76
3.18	Flow through a porous pipe. . . . .	77
3.19	The Heaviside function. . . . .	79
3.20	Comparison between IB and analytical results for different number of nodes. . . . .	80
3.21	Comparison between IB and analytical results for different inlet velocities. . . . .	81
3.22	Comparison between IB and analytical results for different porosity values. . . . .	82
4.1	Eulerian and Lagrangian nodes for representing the fluid and solid domains. The Eulerian and Lagrangian nodes are represented by black squares and red circles, respectively. . . . .	87
4.2	Comparison of different regularized Heaviside functions ( $\mathcal{H}_i$ ) and step function ( $\mathcal{S}$ ). . . . .	89
4.3	Effect of control parameter $\eta$ on the RH function. . . . .	90
4.4	Comparison between different regularized delta functions ( $\mathcal{D}_i$ ). The integral of all these functions over $x \in (-\infty, \infty)$ is equal to one. . . . .	91
4.5	Effect of control parameter $\eta$ on the RD function. . . . .	92
4.6	Results mapping between the Eulerian and Lagrangian computational nodes. . . . .	96
4.7	Effect of Regularized Heaviside (RH) and step functions on the solution accuracy. . . . .	98
4.8	RSME value for the sensitivity analysis (SA) and governing equation (GE). The thick lines represent the actual values for the RSME error and the thin lines represent the least-square approximation of the best fit. . . . .	100
4.9	Comparison between the velocity sensitivity profile of CSA and analytical results in the domain. $w_{wall}$ is the location of the stationary wall and $n$ is the number of nodes used to discretize the domain. . . . .	101
4.10	Improving the sensitivity results by using higher order boundary representation. . . . .	102
4.11	Effect of Regularized Delta (RD) and delta function on the solution accuracy. . . . .	103
4.12	Doublet function of Equation (4.23). . . . .	104

4.13	RSME value for the sensitivity analysis (SA) and governing equation (GE). The thick lines represent the actual values for the RSME error and the thin lines represent the least-square approximation of the best fit. . . . .	105
4.14	Velocity sensitivity profile between the two plates. . . . .	106
4.15	Effect of higher order boundary definition on the sensitivity analysis. . . . .	106
4.16	Physical domain with dimensions for flow over cylinder. . . . .	107
4.17	Convergence results for $Re = 100$ . . . . .	108
4.18	Convergence plots for $Re = 100$ . . . . .	109
4.19	Velocity and pressure contours for $Re = 100$ . . . . .	110
4.20	Velocity components on the solid boundary for $Re = 100$ . . . . .	110
4.21	Physical domain with dimensions for flow over cylinder. . . . .	111
4.22	Verification of the flow variable sensitivities with respect to change in the cylinder radius for different location in the domain. . . . .	113
4.23	Convergence rate for the sensitivities ( $Re = 100$ ). . . . .	114
4.24	Sensitivity contours for $Re = 100$ . . . . .	115
4.25	Comparison between pressure sensitivity results on the boundary for $Re =$ $100$ . . . . .	116
4.26	Effect of design variable on the shape of the nozzle. . . . .	117
4.27	Mesh convergence study for the governing equation. The dashed line rep- resent the fitted curve through points. . . . .	118
4.28	Mesh convergence study for the governing equation. . . . .	119
4.29	Contour plots for flow through nozzle ( $Re = 100$ ). . . . .	119
4.30	Sensitivity contours. . . . .	120
4.31	Verification of sensitivity results for the nozzle. . . . .	121
5.1	Eulerian (○) and Lagrangian (□) nodes for pressure values near and on the immersed boundary. . . . .	128
5.2	Fluid-solid interaction analysis using IB method flow chart. . . . .	129
5.3	Coupled multidisciplinary sensitivity analysis flowchart. . . . .	131
5.4	Physical domain for the vortex induced vibration problem. . . . .	132
5.5	Strouhal number for a single cylinder. . . . .	133
5.6	Number of Lagrangian points effect on the shedding frequency. . . . .	134
5.7	Time history of cylinder center displacement. . . . .	136
5.8	Unsteady u-velocity contours for flow around cylinder at $Re = 100$ and $Re = 500$ . . . . .	137
5.9	Time history of cylinder center displacement sensitivity. . . . .	138
5.10	Unsteady u-velocity contours for flow around cylinder at $Re = 100$ and $Re = 500$ . . . . .	139
5.11	Effect of circle location on Joukowsky airfoil shape. . . . .	141
5.12	Physical domain and elastic structure for the pitching and plunging airfoil. .	141
5.13	Airfoil shape used for FSI calculation. . . . .	142
5.14	Airfoil displacement and rotation results due to aerodynamic loads. . . . .	143
5.15	U-velocity time snapshots for airfoil on an elastic structure. . . . .	144
5.16	Airfoil displacement and rotation sensitivity results due to change in camber.	145
5.17	U-velocity sensitivity time snapshots for airfoil on an elastic structure. . .	146

5.18	Physical domain for the bending monofin.	147
5.19	Time history of the monofin tip displacement in cross-flow.	148
5.20	U-velocity time snapshots for elastic monofin.	148
5.21	Pressure time snapshots for elastic monofin.	149
5.22	Time history of the monofin tip displacement in cross-flow.	150

# List of Tables

2.1	Absolute error value for different number of nodes. . . . .	26
2.2	RMSE value for different number of nodes. . . . .	28
2.3	Comparison between the governing and sensitivity equations. . . . .	39
2.4	RMSE value for different number of nodes. . . . .	40
3.1	RMSE value for different wall locations for Couette flow problem. . . . .	53
3.2	RMSE value for different number of nodes for Couette flow problem. . . . .	54
3.3	RMSE value for different wall velocities. . . . .	55
3.4	RMSE value for different number of nodes. . . . .	61
3.5	RMSE value for different wall locations. . . . .	61
3.6	RMSE value for different wall velocities. . . . .	62
3.7	RMSE values for different number of nodes and delta functions. . . . .	69
3.8	RMSE values for different wall velocities. . . . .	70
3.9	RMSE values for different wall stiffness values. . . . .	71
3.10	RMSE values for different number of nodes. . . . .	74
3.11	RMSE values for different wall velocities. . . . .	75
3.12	Different values used for investigating the effect of $\alpha$ and $\beta$ . . . . .	76
3.13	RMSE values for different number of nodes. . . . .	80
3.14	RMSE values for different inlet velocities. . . . .	81
3.15	RMSE values for different porosity values. . . . .	82
4.1	Comparison between the true and interpolated results using the RD function at arbitrary Lagrangian location, $X$ . . . . .	96
5.1	Comparison of the shedding frequency using IB method and literature. . . .	133

# Acknowledgment

# **Chapter 1**

## **Introduction**

### **1.1 Motivation**

Fluid-structure interaction (FSI) problems play an important role in many scientific and engineering fields, such as automotive, aerospace, and biomedical industry. Despite the wide application, a comprehensive study of FSI systems still remains a challenge due to their strong coupling, nonlinearity, and multi-physics nature. For most FSI problems, analytical solutions of responses are not available and physical experiments are limited in scope, expensive to conduct, and are time consuming. Therefore, in order to get more insight in the physics involved in the complex interaction between fluids and solids, numerical simulations are typically used. The numerical solutions are conducted using Computational Fluid Dynamics (CFD) models for the flow field and Finite Element Analysis (FEA) for the structural response. Nevertheless, the prohibitive amount of computations has been one of the major issues in the design optimization of such coupled multidisciplinary systems. The other bottle neck has been generating an appropriate computational domain that represents the fluid and solid regions with desired fidelity. The effort and time required to take a geometry from a CAD package, refining the model and generating a computational mesh is

usually a large portion of the overall human time required for the simulation. This cannot be automated easily for complex and moving domains. Therefore, techniques that decouple the mesh topology from the shape of the solid boundary can drastically simplify the simulation of flow over complex bodies. The Immersed Boundary (IB) method addresses these challenges for complex body shapes by introducing a new approach to define the solid boundaries.

In aerospace and automotive systems, configurations are optimized for achieving maximum performance and design targets. Due to the large amount of computations involved in the FSI simulation, the gradient-based methods are the best candidates for design optimization of such problems. Sensitivity analysis is an integral part of gradient-based methods. Although there are analytical techniques for efficient and accurate sensitivity calculation, they have not been implemented in commercial CFD packages. Therefore, most gradient optimization techniques depend on a finite difference method for sensitivity calculation when solving a FSI problem. It is well known that finite difference may suffer from low accuracy and high cost.

The motivation for the research proposed in this document is in two areas. First, we want to have sensitivity analysis capabilities that can treat the CFD solvers as a black box. We can potentially solve both the governing equations and the sensitivity response using the same code. Second, a robust analysis technique for the coupled FSI system based on IB method is formulated. The current approach of IB is not suited for the sensitivity analysis due to the discontinuities of representing the solid boundary in its formulation. This will be explained in more detail in the following chapters.

## 1.2 Literature Review

### 1.2.1 Sensitivity Analysis

Sensitivity analysis consists of computing derivatives of the solution of governing equations, i.e. the sensitivity of displacement, velocity, or pressure with respect to one of the several independent design variables, i.e. shape of boundaries or cross-sectional and size of elements. There are various applications for sensitivity information such as aircraft trajectory optimization [1], improving the accuracy of surrogate models as in gradient enhanced Kriging [2] or uncertainty quantification[3]. However, our main motivation is the use of this information in gradient-based optimization. The calculation of gradients is often the most expensive step in the optimization cycle, therefore, efficient methods for accurate calculation of sensitivities are vital to the optimization process. As shown in Figure 1.1, methods for sensitivity calculation can be put into three major categories: i) numerical, ii) analytical, and iii) automatic differentiation.

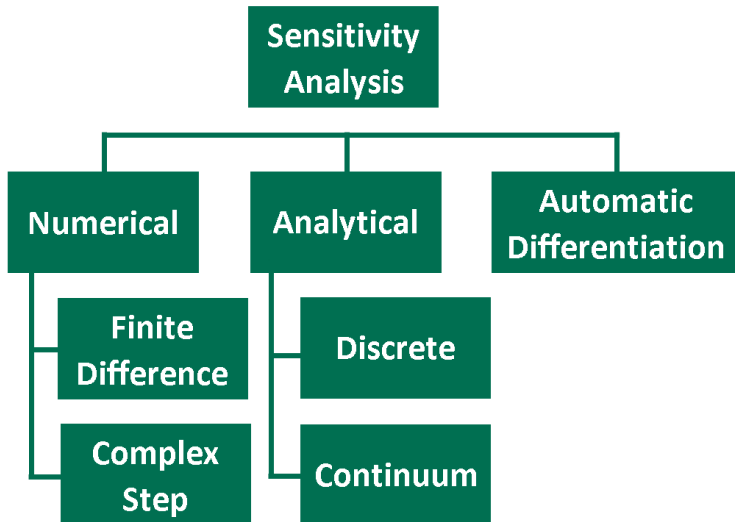


Figure 1.1: Sensitivity calculation techniques.

The Finite Difference (FD) method is probably the easiest method to implement using a commercial software for calculating the sensitivity of a variable. The fact that they can

be implemented even when a given computational model is treated as a black box makes most gradient-based optimization algorithms perform finite differences by default when the user does not provide the required gradients. However, the computational cost associated with finite difference scheme for large systems can become very high. For a system with  $n$  number of design variables, the analysis has to be performed  $n + 1$  times to calculate the design sensitivities. Furthermore, to ensure the accuracy, convergence study needs to be done for selecting an appropriate step size for the finite difference. The inaccuracy of finite differencing could result in convergence difficulties and inaccurate optimum results [4].

Complex Step (CS) method avoids the loss of precision in finite differences approximation by employing complex arithmetic [5]. The complex step derivative is defined as shown in Equation (1.1).

$$\mathcal{F}'(u; b) = \frac{\text{Im}[\mathcal{F}(u; b + ih)]}{h} \quad (1.1)$$

where  $\mathcal{F}(u; b)$  is the function of interest such as the airfoil lift that depends on a response variable,  $u$  i.e. free-stream velocity, and design variable,  $b$ , i.e. shape of the airfoil. Complex step approximates the sensitivities by perturbing the design variable by an imaginary value of  $ih$  and then evaluating the imaginary portion of the resulting response. Using the complex step method, we can choose a small step size for  $h$  without loosing accuracy due to no subtraction involved in CS formulation. However, many commercial packages such as ANSYS or NASTRAN cannot handle complex arithmetic which makes the implementation of complex step method infeasible. Moreover, the high cost of finite difference is still associated with the complex method as well.

Automatic differentiation (AD) is based on the systematic application of the differentiation on computer programs [6]. In the AD approach, the chain rule of differentiation is applied to every line in the program assuming that the computer program consists of a sequence of explicit functions that act successively on some variables. Therefore, by differentiating each of these functions and applying the chain rule, it is possible to calculate the sensitivities.

There has been extensive research on utilizing AD for optimization. Bischof et al. used AD for calculating the sensitivities using a CFD solver. They used ADIFOR for differentiating the source code of their CFD code (TLNS3D) which later was used for calculating the sensitivity of a transonic flow to change in the boundary conditions. Hascout et al., also used AD for a sonic boom reduction under a supersonic aircraft. In all of these works in order to implement AD, access is needed to the source code and modification of the solver extensively to calculate the sensitivities. This makes the use of this method for commercial codes impractical since the source code is usually not available.

The shortcomings of numerical and AD techniques demand more sophisticated methods for sensitivity calculation. These techniques are generally known as analytical methods. Formulation of the analytical sensitivities requires derivation of analytic sensitivity equations. These are obtained by differentiating the governing equations with respect to design variables such as shape of the boundaries. Analytical methods can be further categorized based on how the sensitivity equations are derived and solved. Typically, the continuum equations of the system are solved using an approximate method which discretizes the governing equations. The Discrete Sensitivity Analysis (DSA) technique differentiates the discretized governing equations with respect to design variables to acquire the analytical sensitivity equations [7]. The Continuum Sensitivity Analysis (CSA) differentiates the continuum equations for formulating the sensitivity equations. This system of equations is later discretized and solved for analytical sensitivities.

Regardless of continuum or discrete approach for deriving the sensitivity equations, these can be solved using two approaches: i) the direct method and ii) the adjoint method. This needs to be explained before talking about the sensitivity calculating techniques in detail. To better explain these two methods, let us use the finite element formulation for the displacement method of analysis.

$$KU = F \quad (1.2)$$

where  $K$  is the stiffness matrix that represents a structure,  $U$  is the displacement vector,

and  $F$  is the load vector. The sensitivity of a response,  $R$ , (e.g. stress, displacement) with respect to a design variable,  $b_i$ , is determined by using chain rule for differentiation as shown in Equation (1.3).

$$\frac{dR}{db_i} = \frac{\partial R}{\partial b_i} + \frac{\partial R}{\partial U} \frac{\partial U}{\partial b_i} \quad (1.3)$$

The best way to calculate the displacement sensitivity in Equation (1.3) is to differentiate the governing Equation of (1.2) with respect to design variable  $b_i$ .

$$\frac{\partial K}{\partial b_i} U + K \frac{\partial U}{\partial b_i} = \frac{\partial F}{\partial b_i}$$

The above equation is rewritten as

$$\frac{\partial U}{\partial b_i} = K^{-1} \underbrace{\left[ \frac{\partial F}{\partial b_i} - \frac{\partial K}{\partial b_i} U \right]}_{\text{pseudo-loads}} \quad (1.4)$$

The response sensitivity,  $dR/db_i$ , is calculated by substituting Equation (1.4) in (1.3). The *direct* method first calculates the displacement sensitivity,  $\frac{\partial U}{\partial b_i}$ , and uses that to calculate  $\frac{\partial R}{\partial U} \frac{\partial U}{\partial b_i}$  to form the response sensitivity. This method is performed once for each design variable. The *adjoint* method first calculates  $[K^{-1}]^T \left( \frac{\partial R}{\partial U} \right)^T$  and then takes the dot product with the pseudo-load to form the second part of the response derivative. This method is performed once for each response. Therefore, if the number of responses are smaller than the design variables, the adjoint method will have better performance in terms of simulation cost [8].

The discrete sensitivity analysis has been historically the method of choice to calculate the high-accurate sensitivity when the details of analysis such as discretization approach and matrix assembly of discretized equations are available [9]. This method has been adopted by the structural optimization community and applied to fluid-solid interaction problems as well. Reuther et al., used the discrete method for aerodynamic shape

optimization of a complex aircraft configuration [10]. They used Euler flow as the aerodynamics theory where they optimized different configurations for transonic and supersonic regimes only focusing on fluid pressure. Martins et al. developed an adjoint method for sensitivity analysis for an aero-structural aircraft design framework where the sensitivities were computed using a coupled adjoint approach. The framework was used on a supersonic business jet to calculate the sensitivity of drag with respect to the Outer Mold Line (OML) of the aircraft. They updated the shape of the wing airfoils by using Hicks-Henne functions. These airfoils were then linearly lofted to generate the wing. The advantage of Hicks-Henne functions is that when they are applied to a smooth airfoil, it remains smooth. In their work, the discretization details of the solver needed to be known to calculate the sensitivities since they used DSA [11]. Newman et al. used this approach for aerodynamic shape sensitivity analysis and design optimization of geometrically complex configurations [12]. In their work, the flow is modelled using nonlinear Euler equations where the fluid domain is discretized using unstructured grid. They used highly efficient Gauss-Seidel and GMRES solvers for the solution of linear aerodynamics equations. The mesh deformation due to change in the optimization loop was performed by considering the mesh as a system of interconnected springs. They had to calculate the grid sensitivities by differentiating the grid adaptation algorithms which adds to the cost of the sensitivity analysis. Moreover, mesh deformation algorithms do not always result in usable domain for solving governing equations.

For cases where the boundary deformation is large, mesh deformation fails due to tangled meshes or negative cell volumes [13]. Jameson et al. also used unstructured grid for aerodynamic shape optimization [14]. They used adjoint formulation to calculate the aerodynamic shape sensitivities of a complete aircraft configuration. In their work, the flow is modelled using the Euler equation and the mesh deformation is performed using the spring method. Using DSA they were able to calculate the sensitivities of pressure coefficient of the aircraft wing with respect to its shape and use this data to optimize the shape of the

wing. However, their method cannot be implemented in a commercial solver without access to a source code. Moreover, mesh deformation is still used in this approach which reduces the robustness of their technique. As a matter of fact, source code modification is essential in all other related research papers published in the area as well [15, 16, 17, 18]. However, the source code is usually inaccessible and very complex. Therefore, there is a great interest in sensitivity calculation techniques which require minimal knowledge of the analysis code. This can be achieved using the sensitivity formulation that operates on the governing equations before they are discretized. These methods are commonly known as Continuum Sensitivity Analysis (CSA) methods [19].

CSA involves solving a set of partial differential equations called the Continuum Sensitivity Equations (CSEs) to get the analytical sensitivities. When deriving the CSEs, the governing equations can either be differentiated in local or total form. The local formulation only reflects the effect of design variable change on the response at a specific point in space. On the other hand, the total formulation of sensitivities takes the movement of physical points due to change in the shape of the domain into account.

Choosing between local and total differentiation depends on the Lagrangian or Eulerian representation of the governing equations. In continuum mechanics, displacement and velocity are vectors. In any application, we have the choice of writing these vectors as functions of the position of material particles before deformation. This is called the Lagrangian description of motion and is really helpful for visualizing the deformations. This technique is mostly adopted in solid mechanics where we track the material points as the deformations are usually assumed to be small. However, in fluid flow problems, it is generally hard to identify a reference configuration and the deformations are large, so it is preferable to write the displacement and velocities as functions of the deformed position of the particles. These quantities are now defined for a particular point in space that does not move with the particles. This is called the Eulerian description of motion. As CSA has matured over the years, the computational fluids community adopted the local CSEs since its formulation is

consistent with the Eulerian formulation of the governing equations [20, 21]. The design optimization community has adopted the total formulation for the CFD sensitivities since its formulation is consistent with the Lagrangian formulation of structural mechanics. Nevertheless, the total and local formulations for the sensitivities can be converted from one form to the other. This will be explained in more detail in next chapter.

In summary, sensitivity analysis in general is more matured for structural problems than for fluid dynamics. Nevertheless, neither of these disciplines typically employ CSA for sensitivity calculation. The main reason for this is the need for higher-order derivatives on boundaries that can be hard to approximate [22]. Aurora and Haug [23], followed by Dems and Mroz [24], were among the first to develop the concept of CSA for structural optimization. They modeled the sensitivities as functionals allowing them to convert the sensitivity integrals over the entire domain to the integrals over the boundaries. Although using this approach is possible to reduce the simulation cost, accurate values of functionals are required at the boundaries. This is not always achievable, especially for finite element analysis where the solution accuracy drops near the boundaries. The lack of applicability of CSA in structural optimization is due to the complicated definition of the boundary conditions and maturity of discrete methods for the sensitivity calculation and implementation in commercial finite element packages. In recent years, Cross and Canfield [22] developed specific local CSA formulation to handle these issues. They used Spatial Gradient Reconstruction (SGR) technique to approximate the gradient with higher-order accuracy near the boundaries. This is essential for calculating accurate sensitivities.

The first application of CSA in optimization problems for fluid dynamics is the work by Jameson [25] on adjoint formulation for aerodynamic shape optimization. Borggaard and Burns [26] implemented a direct formulation for shape sensitivity analysis of inviscid supersonic flows over rigid bodies. Stanley and Stewart [27] applied CSA in a fluid mechanics discipline with a goal of aerodynamic design. Pelletier and Etienne have applied CSA to numerous fluid-structure interaction (FSI) problems [28] focused mainly on sensi-

tivities of fluid flow parameters near the structure. Liu and Canfield have employed CSA for shape optimization of nonlinear structures subjected to an aeroelastic gust response [29]. They used the finite element method to solve the potential flow around an airfoil and applied CSA to find the airfoil pressure coefficient sensitivity with respect to the maximum camber.

In almost all of the research done on sensitivity calculation of flow field to shape design variable, body conformal grids were used. The conforming mesh methods consider the interface conditions as physical boundary conditions, which treat the interface location as part of the solution and requires meshes that conform to the interface. Using this approach it is possible to represent the solid boundary shape with a good accuracy. However, due to the coupling of fluid mesh topology and solid boundary shape, with the movement and/or deformation of the solid structure, re-meshing (or mesh-updating) is needed. This is a major problem when dealing with coupled fluid-structure analysis or shape optimization of any kind. Although conforming mesh methods have been widely used in many FSI problems, they are cumbersome, if not impossible, to apply to problems with large deformations [30]. The other shortcoming of body-conformal grids is the effect of mesh deformation on sensitivity analysis. Since the computational domain is affected by change in the shape of the boundaries, it is required to calculate the mesh sensitivities [31] for discrete sensitivity analysis. This adds to the computational effort for calculating sensitivities.

The shortcoming of a robust grid generation and the additional cost of calculating mesh sensitivities motivated an important research effort to develop a technique that does not require the fluid domain's mesh modification throughout the optimization iterations. One of the possible candidates to achieve this goal is the use of Immersed Boundary (IB) methods to decouple the fluid mesh from the solid domain geometry.

## 1.2.2 Immersed Boundary Method

Traditionally the analysis techniques for flow over complex bodies are based on body-fitted multi-block or unstructured grid methods. However, in the last decade another class of techniques, called the immersed boundary methods, has been introduced. The term immersed boundary was first used by Peskin [32] to simulate the blood flow through heart valves. What distinguishes this method from the other methods for representing the solid boundaries is that the flow is solved on the Cartesian grid that does not necessarily conform to the boundaries. Therefore, the mesh generation is greatly simplified and in case of moving/deforming boundaries, there is no need to update the mesh during simulation. A separate formulation is used to impose the effect of the boundaries on the governing equations.

Now consider the simulation of flow past a circular cylinder as shown in Figure 1.2. Generating structured or unstructured grids is achieved in two steps. First, a surface grid covering the boundaries is generated. This is then used as a boundary condition to generate a grid in the volume occupied by the fluid. The differential form of the governing equations is then transformed to a curvilinear coordinate system aligned with the grid lines [33]. The governing equations are then discretized on this curvilinear grid and solved using appropriate technique.

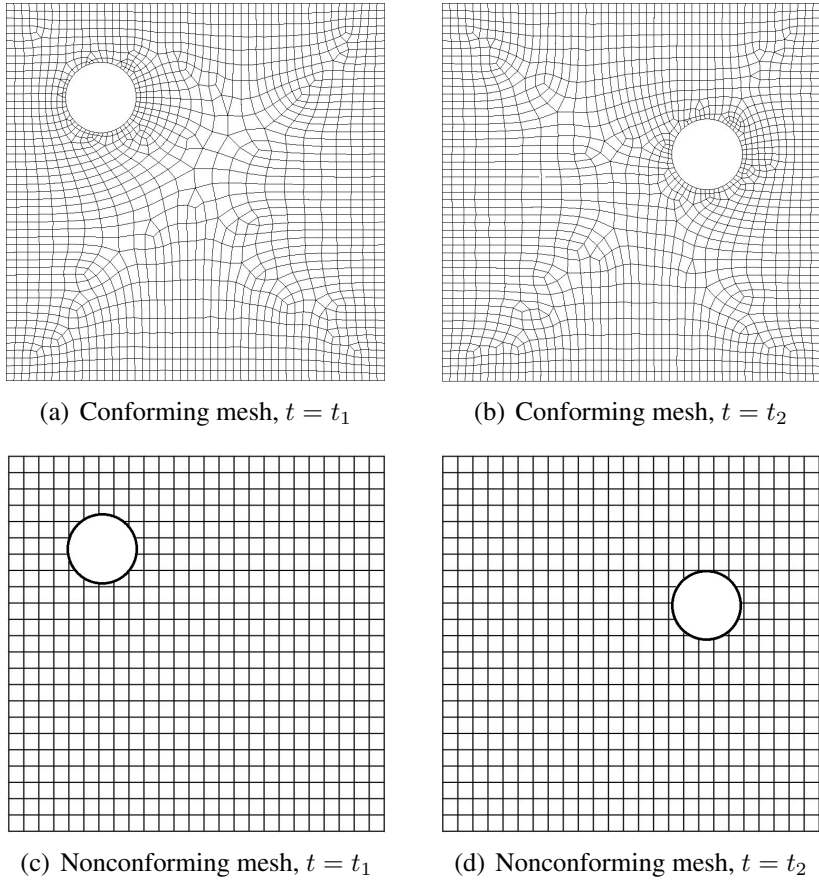


Figure 1.2: Example of conforming and nonconforming meshes.

Non-body-conformal Cartesian grid can also be utilized for this simulation as shown in Figure 1.2. In this approach, the IB would still be represented through some means such as a surface grid, but the Cartesian volume grid would be generated with no regard to this surface grid. Thus, the solid boundary would cut through this Cartesian volume grid. Because the grid does not conform to the solid boundary, incorporating the boundary conditions would require modifying the equations in the vicinity of the boundary. Assuming that such a procedure is available, the governing equations would then be discretized using a finite-difference, finite-volume, or finite-element technique without resorting to coordinate transformation or complex discretization operators.

Depending on how the effect of solid boundaries are imposed, IB methods can be divided into three categories: i) continuous forcing, ii) discrete forcing, and iii) cut-cell

method.

The continuous forcing method was originally used by Peskin [32] and later further developed by other researchers [34, 35, 36]. In this approach, the boundary configuration is described by a curve  $x(s, t)$  (Lagrangian nodes) where the location of each point on this boundary is governed by its equations of motion. The forces that the curve  $x(s, t)$  exerts on the fluid is calculated by the constitutive law of the curve  $x(s, t)$  that relates the displacements to stress values. These stress values are transferred to the Navier-Stokes (NS) (Eulerian nodes) for the fluid by means of a Dirac delta function. Practical implementation of this method rests in representing the Dirac delta function as a discrete function that has the same properties. This method is applied to a variety of problems, including Cardiac blood flow [37], animal locomotion [38], multiphase flows [39], and particle sedimentation [40].

Peskin's method is well suited for elastic boundaries. For stiff boundaries, the constitutive laws of the solid boundaries will result in instabilities in the solution of governing equations [41]. The virtual boundary method of Goldstein [42] enables us to handle these rigid boundaries. The main idea of this approach is the same as Peskin's method where the solid boundary is treated as a virtually existing surface embedded in the fluid. The force on this surface is calculated by the requirement that the fluid velocity should satisfy the no-slip condition. Since this body force is not known a priori, it is calculated in a feedback way.

The penalization method is also categorized under the continuous forcing approaches to the IB problem. This technique is based on the Brinkman equation that describes the fluid flow through a porous medium. The Brinkman equation is analogous to Fourier's laws in heat conduction and Ohm's law in the field of electrical engineering [43]. This approach was first proposed by Arquis and Caltagirone [44] where they imposed the boundary conditions by adding the penalization terms to the momentum equations. The main idea of this approach is to model the solid obstacles as a porous medium with porosity of  $\mathcal{K}$ . Porosity is a measure of void spaces in a material. Therefore, by selecting low values for

porosity, the porous domain acts as a solid wall. It has been demonstrated that the solution of the penalized incompressible NS equations converge to the exact solution as the porosity approaches zero [45]; however, in the practical implementation, extremely low values for porosity will result in systems with a very large stiffness that are numerical instability. To apply the porosity within the solid domain, a Heaviside function is used by other researchers [46, 47].

The continuous forcing approach is very attractive for flows on both rigid and elastic boundaries due to its ease of implementation. This technique can be added to an already available commercial package such as ANSYS Fluent for CFX with a limited effort. One of the shortcomings of this approach is the smoothing of the forcing function near the boundary. This can result in inability for sharp representation of the immersed boundary in cases such as compressible flows. However, accuracy for representing the boundaries can be improved by refining the mesh and using higher-order force mapping schemes.

Mohd-Yusof formulated the discrete formulation of IB method [48] for addressing the time penalties associated with the simulation involving moving boundaries. The main idea of this technique is same as the virtual boundary method where a force term is added to momentum equations to represent the solid boundary. However, the momentum equation manipulation is done in discrete manner. In the work of Mohd-Yusof [48] and Verzicco et al. [49] this is done by modifying the discretization stencil in the vicinity of the boundary curve so that the velocity values on this boundary satisfy a pre-defined condition. The major advantage of this approach is the absence of user specified parameters; however, its implementation depends strongly on the discretization approach used for the analysis. Therefore, it cannot be easily implemented nonintrusively with commercial codes. This implementation of discrete forcing method has been applied to many different problems such as turbulent flow inside an internal combustion engine [49], flow past 3D bluff bodies [50], and flow in a cylindrical stirred tank [51].

In the cut-cell methods, the grid cells are cut by the solid boundary and reshaped so

that they form a boundary-conforming, unstructured grid. This is shown in Figure 1.3.

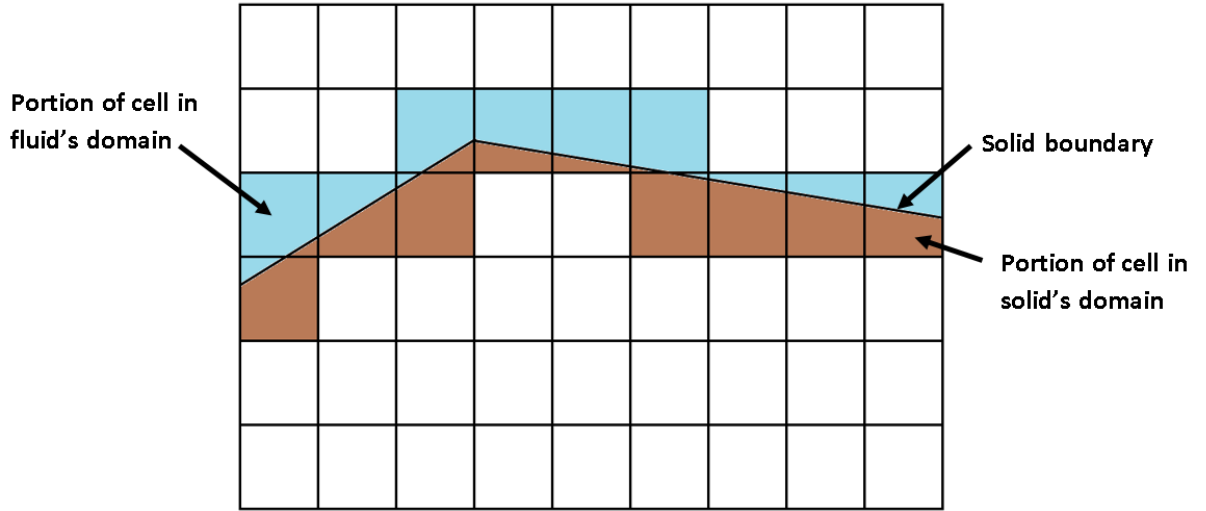


Figure 1.3: Modified mesh near the solid boundary for cut-cell method.

The cut-cell method was first introduced by Clarke [52] for inviscid flows. This method has been applied to both collocated and staggered grids [53], however most applications were focused on 2D flows [54, 55]. This is because of the many possibilities for the geometrical shape of the cut-cell, that makes the flux calculation and therefore numerical implementation is extremely difficult.

### 1.2.3 Sensitivity Analysis for IB Method

The body of the research done in the immersed boundary community has been concentrated on the improvement of method accuracy and resolving the stability issues. However, there has not been much effort in the sensitivity calculation by using an IB formulation. There has been some research on the sensitivity analysis using the penalization framework. Borrhval and Petersson applied the penalization method for topology optimization of fluids in Stokes flow [56]. They used the discrete sensitivity analysis to calculate the sensitivity of fluid pressure to the shape of the boundaries. They used this technique to optimize the shape of a diffuser and a pipe bend. They verified their methodology for outflow problems

as well, where they optimized the shape of solid domain to maintain the least possible pressure drop by constraining the penalized region volume. Challis and Guest investigated the level set formulation for the topology optimization of fluids in Stokes flow [57]. They used the penalization technique to formulate the no-slip condition on the solid boundaries. They implemented the topological sensitivities in their solver where they used power dissipation minimization to optimize the shape of a diffuser and a connecting 3D pipe. The penalization method is probably the easiest of the IB methods to implement. This is because it does not have a free parameter such as in virtual boundary method and does not depend on the discretization such as discrete forcing methods. Moreover, no interpolation is needed for applying penalization method to a computational domain. In the penalization method, the fluid and solid domains are differentiated based on a scalar function (porosity) which is very similar to the density-based approaches in the topology optimization community [58]. This is probably the biggest reason for researchers to use penalization technique for shape optimization using IB method, since the available techniques from topology optimization community can be used [59, 60]. Similar to topology optimization, the shortcoming of penalization technique is in its accuracy for representing the boundaries. Since the nodes are assigned with the porosity values, it is extremely difficult if not impossible to control the exact location of the immersed boundary when it does not coincide with the computational nodes. Moreover, the current demonstration problems for the penalization technique are only applicable to low Reynolds numbers flow.

### 1.3 Research Contribution

Design optimization for coupled fluid-solid interaction problems is a challenging effort. The current state-of-art technique handles the MDO problem by using unstructured grid and using DSA for sensitivity calculation. However, these techniques cannot be used along with arbitrary software packages without a deep understanding of how the governing equa-

tions are formulated and discretized within the solver. Moreover, due to the use of body-conformal grids for fluid domain discretization, additional cost and effort are introduced in both the analysis and sensitivity calculation. Approximating the mesh sensitivities and mesh deformation are two examples for this extra calculation. This research presents a specific formulation for immersed boundary method along the continuum sensitivity analysis for satisfying both of the issues regarding mesh deformation and sensitivity implementation [61]. The specific contributions of this research are as follows:

- Two different classes of continuous immersed boundary methods are explained and used within CSA framework to calculate the sensitivity of different flow parameters with respect to shape design variables. The immersed boundary method is based on relaxed Dirac delta functions to transfer the data between the fluid and structure domains; however, this formulation cannot be used within the CSA framwork. A smooth representation for Dirac delta function is developed for this purpose.
- This research is the first application of CSA for sensitivity analysis of fully coupled FSI simulation modeled with the IB technique. IB method enables us to have a robust FSI simulation and also creates high-fidelity solution of the NS equations. The sensitivity analysis builds on top of this framework so it can be used for shape design optimization using gradient-based optimization techniques.
- The use of continuum immersed boundary methods for sensitivity analysis of flows with moderate to high Reynolds numbers is another contribution of this work. Most of the previous works done in this area regarding the sensitivity analysis are based on flows with lower Reynolds numbers such as Stokes flows.

# Chapter 2

## Design Sensitivity Analysis

In this chapter, the concept of discrete and continuum sensitivity formulations is discussed, and the general approach for deriving the sensitivity equations are presented. Then, the difference between the local and total formulation of the sensitivity response is discussed and finally, the independence of continuum sensitivity analysis from the discretization step is proven. This enables us to reuse the solver for the governing equations to calculate the sensitivity response. Discrete sensitivity formulation is not capable of using the same solver for both the solution of governing equations and sensitivity analysis. The two sensitivity analysis techniques are applied to a heat transfer benchmark problem where the sensitivity of response to the shape of the domain is calculated. This problem is also used in the following chapter for implementation of different immersed boundary methods.

### 2.1 General Formulation

A general shape for the computational domain is defined in Figure 2.1. The response variable on this domain can represent a fluid, i.e. pressure or velocity, or a solid, i.e. displacements. Nevertheless, in any of these cases, the response is calculated by solving

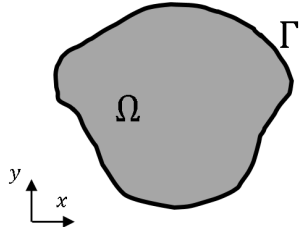


Figure 2.1: General computational domain  $\Omega$  with boundary  $\Gamma$ .

a governing equation subjected to boundary conditions. In this research, the governing equation and the boundary conditions are represented in the functional form.

$$\mathbf{A}(\mathbf{u}, t; \mathbf{b}) = \mathbf{f}(\mathbf{x}, t; \mathbf{b}) \quad \text{on} \quad \Omega \quad (2.1a)$$

$$\mathbf{B}(\mathbf{u}, t; \mathbf{b}) = \mathbf{g}(\mathbf{x}, t; \mathbf{b}) \quad \text{on} \quad \Gamma \quad (2.1b)$$

where  $\mathbf{A}$  is the governing equation, such as Navier-Stokes equations for the fluid or elastic equations for the solid domain, and  $\mathbf{B}$  is the boundary condition.  $\mathbf{u}$  is the response variable such as displacement or pressure.  $t$  is time,  $\mathbf{b}$  is the design variable such as shape or size, and  $\mathbf{x}$  is the spatial coordinate.  $\mathbf{f}$  and  $\mathbf{g}$  are the values of the governing equation and boundary conditions. It should be noted that in this formulation, the function  $\mathbf{u}$  is only implicitly dependent on the design variable  $\mathbf{b}$ . This is important when deriving the sensitivity equations later in this chapter. This implicit dependence is represented by using the semicolon symbol in the definition of  $\mathbf{A}$  and  $\mathbf{B}$ .

For a general problem formulation, the total sensitivity of the response variable,  $\mathbf{u}$ , with respect to the  $i$ -th design variable,  $b_i$ , is written as:

$$\frac{D\mathbf{u}}{Db_i} = \underbrace{\frac{\partial \mathbf{u}}{\partial b_i}}_{\text{local derivative}} + \underbrace{\frac{\partial \mathbf{u}}{\partial \mathbf{x}} \cdot \frac{\partial \mathbf{x}}{\partial b_i}}_{\text{convective term}} \quad (2.2)$$

The total derivative is known as the material derivative in continuum mechanics [62]. This

total sensitivity defines the change of response variable,  $\mathbf{u}$ , to design variable and space dependent changes. The material derivative consists of the local derivative,  $\partial\mathbf{u}/\partial b_i$ , plus the convective term,  $\partial\mathbf{u}/\partial\mathbf{x} \cdot \partial\mathbf{x}/\partial b_i$ . The local derivative is the measure of response variable change at a fixed location due to change in the design parameter. Whereas, the convective term accounts for the movement of points in space due to change in the design variable. This is especially applicable to shape sensitivity analysis where the change in design variable will cause the material points to move [22].

The convective term consists of two separate gradients: i)  $\partial\mathbf{u}/\partial\mathbf{x}$  which represents the spatial gradient of the response variable, and ii)  $\partial\mathbf{x}/\partial b_i$  that defines the sensitivity of the location of computational nodes with respect to changes in the design variable. The response gradient,  $\partial u/\partial x$ , is calculated from the analysis results using the finite difference approach or derivatives of shape functions in FEA formulation. The calculation of the domain sensitivity,  $\partial\mathbf{x}/\partial b_i$ , requires more attention.

A standard approach for calculating the domain sensitivity is to employ the techniques that are used to deform the body-conformal mesh in CFD/FEA simulations. These methods are commonly based on representing the computational grid as a system of springs that are connect to each other at the nodes. This system is modeled and solved using structural analysis techniques, where the sensitivities can be easily implemented. This is effectively a shape sensitivity analysis for a structural problem [63]. This step is removed from the analysis if the computational domain is not affected by the design variable, when  $\partial x/\partial b$  is equal to zero [61]. This is one of the reasons to use the immersed boundary calculation, since it reduces the cost of simulation. This is discussed in more details in Chapter 3.

## 2.2 Benchmark Cases

To compare the discrete and continuum sensitivity analysis formulations, two problems from different disciplines are selected. As a simplified representation for the fluid/thermal

systems, the one-dimensional heat transfer analysis in a beam is selected. This problem is used by different researchers for investigating sensitivity analysis for nonlinear systems [64], thermal design, and monitoring [65, 66]. The special interest in this problem is due to the availability of analytical solution to verify the numerical results of the sensitivity analysis. For the solid mechanics problem, a finite element model of an axial bar with a distributed load is selected [67]. This problem is used by different researchers as a demonstration case for sensitivity analysis [22, 68].

### 2.2.1 Heat transfer benchmark case

The temperature distribution in a one-dimensional domain is governed by the Laplace equation as shown in Equation (2.4).

$$\frac{\partial^2 T}{\partial x^2} = \frac{1}{\alpha} \frac{\partial T}{\partial t} \quad (2.3)$$

Where  $T$  is temperature,  $x$  is a spatial variable,  $t$  is time, and  $\alpha$  is thermal diffusivity. For this problem we are only interested in a steady state solution of the system; therefore, the right-hand-side of Equation (2.3) is equal to zero. Thus, the governing equation for this problem is written as:

$$\frac{\partial^2 T}{\partial x^2} = 0 \quad (2.4)$$

The boundary conditions are defined as constant temperatures at the two ends of the domain as  $T_0$  and  $T_L$ . The domain length is selected as  $L$ . This is shown in Figure 2.2. The

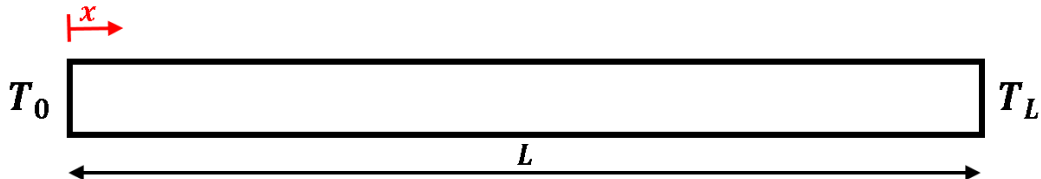


Figure 2.2: One dimensional domain with heat conduction.

analytical solution for this problem is available as

$$T = \frac{T_L - T_0}{L}x + T_0 \quad (2.5)$$

The analytical sensitivity of the temperature with respect to the beam's length is calculated by differentiating Equation (2.5) to  $L$ .

$$\frac{\partial T}{\partial L} = -\frac{T_L - T_0}{L^2}x \quad (2.6)$$

This is later used for verifying the discrete and continuous sensitivity results.

### 2.2.2 Solid mechanics benchmark case

The benchmark problem was selected from a finite element text book by Szabo, B. and Babuska, I. [67]. The axial bar is shown in Figure 2.3. The length of the bar is selected as  $L = 1$  with an axial stiffness of  $EA = 1$ . The distributed load is selected as a sine wave,  $F_d(x) = \sin(\pi x/L)$ , with an additional axial load at the end,  $F_p = 1/\pi$ . The beam is fixed using a spring stiffness,  $k = 10$ , at  $x = L$ . The governing equation for the displacement

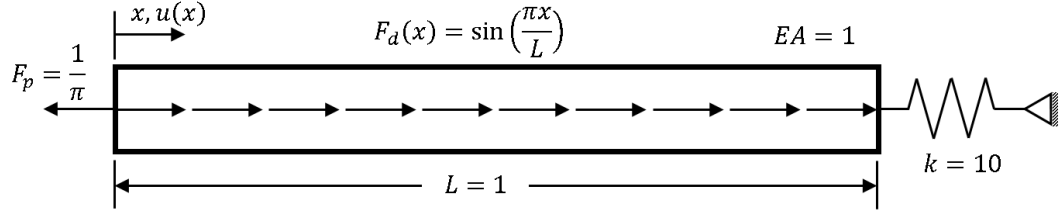


Figure 2.3: Axial bar under distributed loading.

of the axial bar and its corresponding boundary conditions are defined in Equation (2.7). The bar length is selected as the design variable; therefore, it is included explicitly in the

governing equation and boundary condition definitions.

$$\frac{\partial^2 u}{\partial x^2} + \sin\left(\frac{\pi}{L}x\right) = 0 \quad (2.7a)$$

$$\begin{cases} \frac{\partial u}{\partial x}\Big|_{x=0} = \frac{1}{\pi} \\ \frac{\partial u}{\partial x}\Big|_{x=L} = -10u(L) \end{cases} \quad (2.7b)$$

For this problem, the analytical solution is written as shown in Equation (2.8).

$$u(x; L) = \frac{L^2}{\pi^2} \sin\left(\frac{\pi x}{L}\right) + \frac{2L + 10(L-1)(L-x) - 1}{10\pi} \quad (2.8)$$

The displacement equation of (2.8) is differentiated to calculate the sensitivity of displacement to the bar length. The sensitivity equation (2.9) is later used to verify the results of continuum and discrete sensitivity formulations.

$$\frac{\partial u}{\partial L} = \frac{2L}{\pi^2} \sin\left(\frac{\pi x}{L}\right) - \frac{x}{\pi} \cos\left(\frac{\pi x}{L}\right) + \frac{10L - 5x - 4}{5\pi} \quad (2.9)$$

## 2.3 Discrete Sensitivity Analysis

### 2.3.1 Formulation

The derivation of the discrete sensitivity equations starts with the discrete form of the governing equations. For the linear case, the governing equation (2.1a) is discretized as shown in Equation (2.10)

$$[K] [U] = [F] \quad (2.10)$$

Where  $[K]$  is the discrete operator that represents the governing equation;  $[U]$  is the vector of the response variables defined at each of the degrees of freedom, and  $[F]$  is the vector of the applied loads. The sensitivity of this system to design variable  $b$  is derived by differentiating Equation (2.10).

$$[K] \left[ \frac{\partial U}{\partial b} \right] = \left[ \frac{\partial F}{\partial b} \right] - \left[ \frac{\partial K}{\partial b} \right] [U] \quad (2.11)$$

Solving Equation (2.11) yields a solution for sensitivity of response variable,  $\partial U / \partial b$ . This is achievable if the values of  $\partial F / \partial b$  and  $\partial K / \partial b$  are known. It should be noted that  $U$  is calculated by solving the governing equation (2.10). For the case of design independent loads,  $\partial F / \partial b$  is equal to zero; this happens in many situations such as design optimization with pure mechanical loads. This assumption is violated for the cases when changing the design variables alter the loadings on the structure. The best example for this case is the design of thermally loaded structures where, due to thermal expansions, changing the size of elements will affect the thermal loadings [69]. Calculating the  $\partial K / \partial b$  term requires a detailed understanding of the discretization approach. This often requires source code modification that makes this method difficult to implement for commercial codes such as ABAQUS or FLUENT. The discrete method is an accurate approach for calculating the sensitivities as will be demonstrated with the following examples; however, it is almost impossible to implement in general-purpose solvers due to non-accessibility of the source code. The discrete sensitivity analysis is build in couple of analysis tools such as Nastran, ASTROS, and OptiStruct and can be used for sensitivity analysis.

### 2.3.2 Implementation on heat transfer problem

The discrete sensitivity equations are formulated by discretizing the governing equation (2.4) using the finite difference method. It should be noted that finite difference is used for discretization of the continuum governing equation and not for the sensitivity calculation.

Other techniques, such as finite volume or finite elements, can be used for the discretization of the governing equations as well. For this problem, the design variable affects the shape of the domain which is related to the distance between the nodes in a discrete manner. Therefore, for the sake of sensitivity analysis, it is required to keep the nodal distances in the discretized solution as well. The domain is discretized by using six nodes as shown in Figure 2.4. The second derivative of Equation (2.4) needs to be approximated for dis-

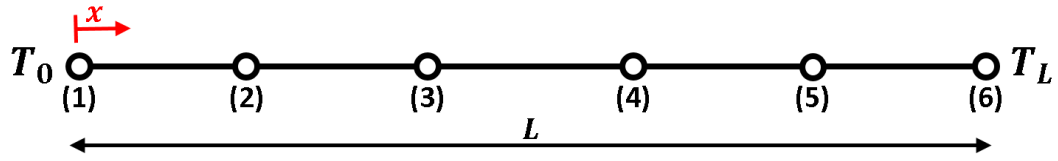


Figure 2.4: One dimensional computational domain for the heat conduction problem.

cretization. This is done by writing the Taylor series expansion of temperature at an arbitrary location  $x_i$ . By using the central difference method, the second order approximation for the second order derivative is written as shown in Equation (2.12).

To maintain the generality, we assume that distance of node  $T_i$  to  $T_{i+1}$  is  $\Delta_i$  and the distance of node  $T_i$  to  $T_{i-1}$  is  $\Delta_{i-1}$ .

$$\frac{\partial^2 T}{\partial x^2} = \frac{T_{i-1}\Delta_{iL} - T_i(\Delta_{iL} + \Delta_{iR}) + T_{i+1}\Delta_{iR}}{\frac{1}{2}[\Delta_{iL}\Delta_{iR}^2 + \Delta_{iL}^2\Delta_{iR}]} \quad (2.12)$$

The discretized governing equation of (2.12) is written in a matrix form as shown in Equation (2.13).

$$\begin{bmatrix} \frac{-2}{\Delta_1\Delta_2} & \frac{2}{\Delta_1\Delta_2+\Delta_1^2} & 0 & 0 \\ \frac{2}{\Delta_2^2+\Delta_2\Delta_3} & \frac{-2}{\Delta_2\Delta_3} & \frac{2}{\Delta_2\Delta_3+\Delta_2^2} & 0 \\ 0 & \frac{2}{\Delta_3^2+\Delta_3\Delta_4} & \frac{-2}{\Delta_3\Delta_4} & \frac{2}{\Delta_3\Delta_4+\Delta_3^2} \\ 0 & 0 & \frac{2}{\Delta_4^2+\Delta_4\Delta_5} & \frac{-2}{\Delta_4\Delta_5} \end{bmatrix} \begin{bmatrix} T_2 \\ T_3 \\ T_4 \\ T_5 \end{bmatrix} = - \begin{bmatrix} \frac{2T_1}{\Delta_2^2+\Delta_1\Delta_2} \\ 0 \\ 0 \\ \frac{2T_6}{\Delta_5\Delta_4+\Delta_5^2} \end{bmatrix} \quad (2.13)$$

To verify the discretization process, we compare the analytical solution of this problem with the result of Equation (2.13) in Figure 2.5. For this problem we choose  $T_1 = 0$ ,  $T_6 = 1$  as the boundary conditions and  $L = 1$ . As shown in this figure, the discrete and continuum results match very well for a different number of nodes. This is done by comparing the absolute maximum error between the analytical and approximate results as shown in Table 2.1.

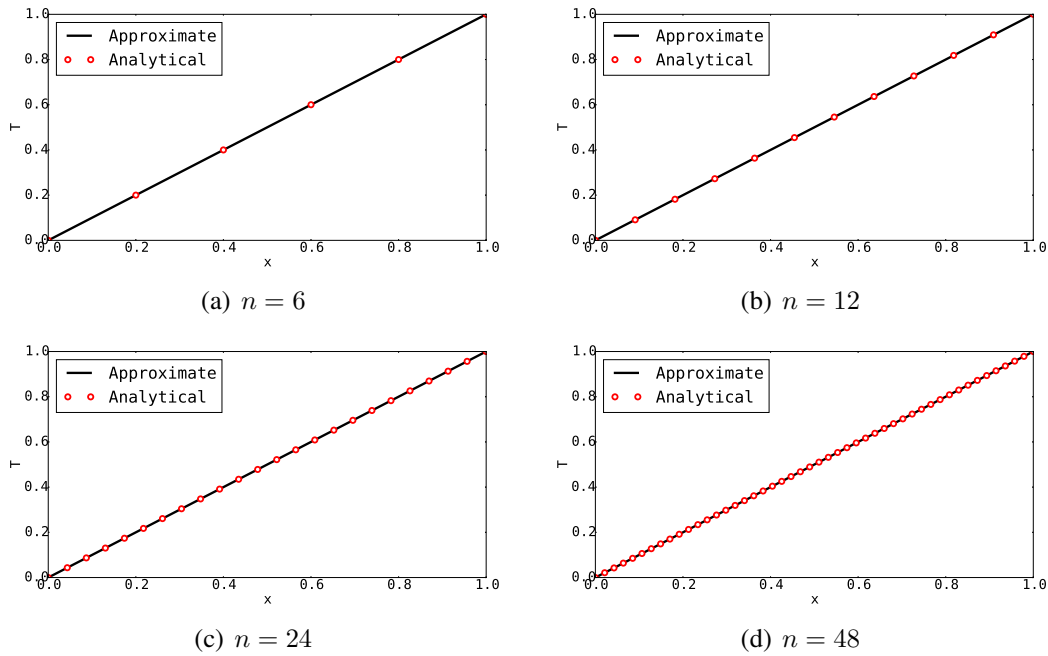


Figure 2.5: Comparison between the analytical and finite difference solutions for 1D heat equation for different number of nodes.

Number of nodes	absolute error
6	$1.85 \times 10^{-16}$
12	$2.03 \times 10^{-16}$
24	$1.27 \times 10^{-15}$
48	$8.55 \times 10^{-15}$

Table 2.1: Absolute error value for different number of nodes.

The discrete sensitivity equations are derived by differentiating the discretized governing equation of (2.13) to the length of the domain. We assume that the change in the length only affects the nodal distance between the last two nodes and the rest remain un-

changed. This means that only the node next to the boundary will move, and the rest of nodes will be stationary. This is required to make sure that the sensitivity at each of the degrees of freedom is only a function of the change in shape not the movement of material nodes; therefore,  $\partial x/\partial b$  is equal to zero.

In order to differentiate Equation (2.13), it is required to calculate the derivative of nodal distances in Equation (2.13) with respect to  $L$ ,  $\partial\Delta_i/\partial L$ . For an equally spaced grid, the nodal distance is written as

$$\Delta = \frac{L}{n - 1}$$

Where  $L$  is the length of the domain and  $n$  is the number of nodes used to discretize the domain. Therefore, the sensitivity of nodal distances to the length of the domain is calculated as:

$$\frac{\partial\Delta}{\partial L} = \frac{1}{n - 1} \quad (2.14)$$

The differentiated form of the discretized Equation (2.13) is written as

$$\begin{bmatrix} -2 & 1 & 0 & 0 \\ 1 & -2 & 1 & 0 \\ 0 & 1 & -2 & 1 \\ 0 & 0 & 1 & -2 \end{bmatrix} \begin{bmatrix} T'_2 \\ T'_3 \\ T'_4 \\ T'_5 \end{bmatrix} = \underbrace{\frac{1}{2} \frac{\partial\Delta}{\partial L} \frac{1}{\Delta}}_{\text{effect of shape change}} \begin{bmatrix} 0 \\ 0 \\ 0 \\ T_6 \end{bmatrix} - \underbrace{\frac{1}{2} \frac{\partial\Delta}{\partial L} \frac{1}{\Delta}}_{\text{effect of shape change}} \begin{bmatrix} 0 & 0 & 0 & 0 \\ 0 & 0 & 0 & 0 \\ 0 & 0 & 0 & 0 \\ 0 & 0 & -3 & 1 \end{bmatrix} \begin{bmatrix} T_2 \\ T_3 \\ T_4 \\ T_5 \end{bmatrix} \quad (2.15)$$

It should be noted that since only the adjacent node to the boundary is affected by shape change, only that element in the matrix derivative has a value.  $T'_i$  represents the sensitivity of temperature to length of the domain.

To verify the results of Equation (2.15), we compared it with the analytical sensitivity results as shown in Figure 2.6. We discretized the domain using 11, 41, 81, and 161 nodes for this purpose; however, this does not affect the solution accuracy. We chose the normalized root-mean-square deviation (NRMSD) for comparing the sensitivity results. This is

defined in Equation (2.16).

$$NRMSE = \frac{\sqrt{\frac{\sum(\hat{y}_t - y)^2}{n}}}{y_{max} - y_{min}} \quad (2.16)$$

Where  $\hat{y}$  is the value calculated using DSA and  $y$  is the true value calculated by the analytical equation. The results for the NRMSE for this problem using different numbers of nodes are shown in Table 2.2.

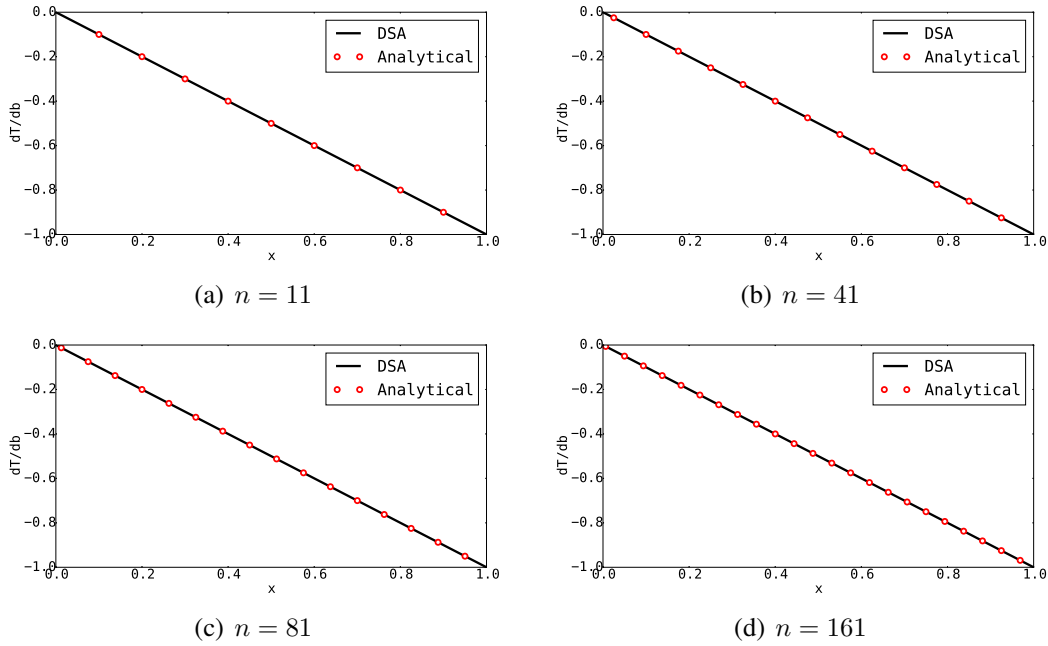


Figure 2.6: Comparison between discrete sensitivity analysis and analytical results for different number of nodes.

Number of nodes	NRMSE
11	$1.68 \times 10^{-16}$
41	$2.49 \times 10^{-15}$
81	$1.49 \times 10^{-15}$
161	$2.85 \times 10^{-15}$

Table 2.2: RMSE value for different number of nodes.

As shown in Figure 2.6 and Table 2.2, the accuracy of discrete sensitivity analysis is not affected by the number of nodes chosen to discretize the domain.

### 2.3.3 Implementation on solid mechanics problem

Finite elements are used to discretized the axial bar problem is shown in Figure 2.3. The governing equation of (2.7a) is discretized using a uniform mesh, linear shape functions, and one point Gauss integration. As mentioned in Section 2.2.2, the design variable is selected as the length of the bar affecting the distances between the nodes. To keep the local and total derivatives equal, we fix the interior computational nodes in space and change the length of the bar by only moving the last node. Therefore, the shape design variable only affects the size of the last element and should be included in the discretized equations. This is shown in Figure 2.7. Since the internal nodes do not move, the design velocity is zero for these nodes.

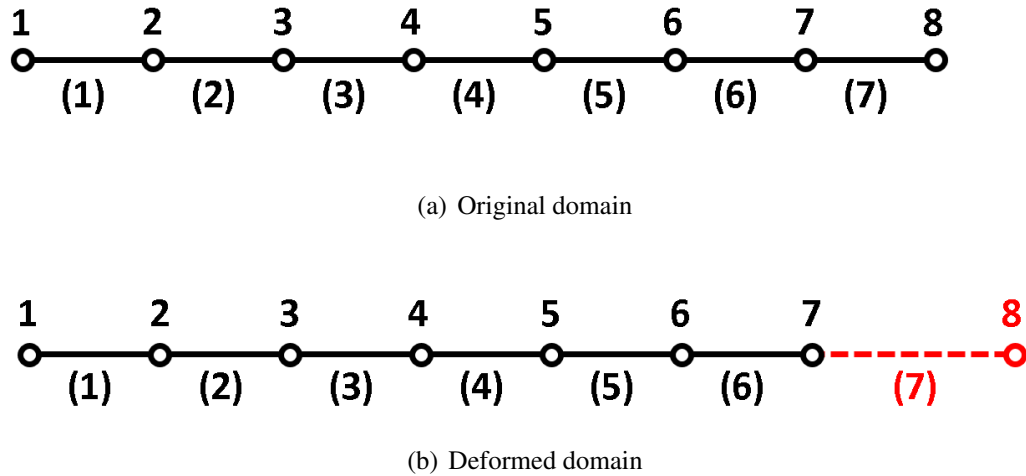


Figure 2.7: Changing the bar length by fixing the interior computational nodes and only moving the boundary (red) node. Node numbers are represented by  $i$  and element numbers by  $(i)$ .

For the case of three elements, the stiffness matrix is written as

$$[K] = EA \begin{bmatrix} 1/l_1 & -1/l_1 & 0 & 0 \\ -1/l_1 & 1/l_1 + 1/l_2 & -1/l_2 & 0 \\ 0 & -1/l_2 & 1/l_2 + 1/l_3 & -1/l_3 \\ 0 & 0 & -1/l_3 & 1/l_3 \end{bmatrix} \quad (2.17)$$

Where  $l_i$  are the lengths of the elements. It should be noted that only  $l_3$  is affected by changing the length of the domain in this formulation of the problem. The discretized equation for this problem is written as shown in Equation (2.18).

$$[K - K_s][U] = [F_d] - [F_p] \quad (2.18)$$

Where  $[K]$  is the stiffness matrix of the bar;  $[K_s]$  is the stiffness of the spring boundary;  $[F_d]$  is the distributed load; and  $[F_p]$  is the point load. The point load is subtracted because of its negative direction for this problem. For the case of  $EA = 1$ ,  $F_d = \sin(\pi x/2)$ ,  $L = 1$ ,  $F_p = 1/\pi$ , and  $K_s = 10$  the solution of Equation (2.18) is compared with the analytical results of the problem as shown in Equation (2.8) in Figure 2.8. We chose Normalized Root-Mean-Square Error (NRMSE) as the metric of comparison. This is calculated as shown in Equation (2.19)

$$NRMSE = \frac{\sqrt{\frac{\sum_{t=1}^n (\hat{y}_t - y)^2}{n}}}{y_{max} - y_{min}} \quad (2.19)$$

where  $\hat{y}_t$  is numerical and  $y$  is the analytical result. The discrete sensitivity equation is derived by differentiating Equation (2.18) with respect to the shape of the domain as shown in Equation (2.20).

$$\left[ \frac{\partial K}{\partial b} - \frac{\partial K_s}{\partial b} \right] [U] + [K - K_s] \left[ \frac{\partial U}{\partial b} \right] = \left[ \frac{\partial F_d}{\partial b} \right] - \left[ \frac{\partial F_p}{\partial b} \right] \quad (2.20)$$

Where  $b$  is the design variable.  $[K_s]$  is not affected by the design variable; therefore, its derivative with respect to  $b$  is equal to zero. The same argument can be made for the point

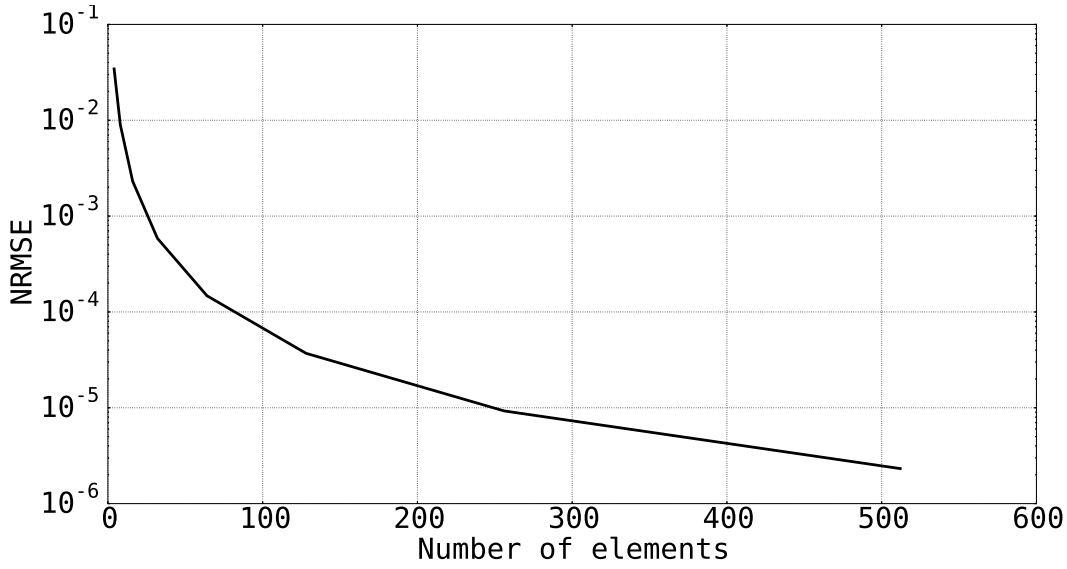


Figure 2.8: Mesh convergence of the finite elements analysis for axial bar.

load  $F_p$ . Using these observations, Equation (2.20) is simplified as:

$$\left[ \frac{\partial U}{\partial b} \right] = [K - K_s]^{-1} \left\{ \left[ \frac{\partial F_d}{\partial b} \right] - \left[ \frac{\partial K}{\partial b} \right] [U] \right\} \quad (2.21)$$

In Equation (2.21),  $[U]$  is known as the result of solving the governing equation (2.18) and  $\frac{\partial F_d}{\partial b}$  is easily calculated since the distributed force is analytically known.  $\frac{\partial K}{\partial b}$  is calculated by differentiating Equation (2.17). It should be noted that the change in bar length,  $L$ , only affects  $l_3$ . Therefore,  $\frac{\partial l_3}{\partial L}$  is equal to one. Finally, the sensitivity of the stiffness matrix to the shape design variable for a simple case of Equation (2.17) is written as:

$$\left[ \frac{\partial K}{\partial L} \right] = -EA \begin{bmatrix} 0 & 0 & 0 & 0 \\ 0 & 0 & 0 & 0 \\ 0 & 0 & 1/l_3^2 & -1/l_3^2 \\ 0 & 0 & -1/l_3^2 & 1/l_3^2 \end{bmatrix} \quad (2.22)$$

The sensitivity results of solving the discrete Equation (2.21) are compared with the analytical result from Equation (2.9). This comparison is shown as NRMSE values in Figure 2.9.

As shown here, the analytical and discrete sensitivity results agree very well. Moreover, the error decreases as we increase the number of elements.

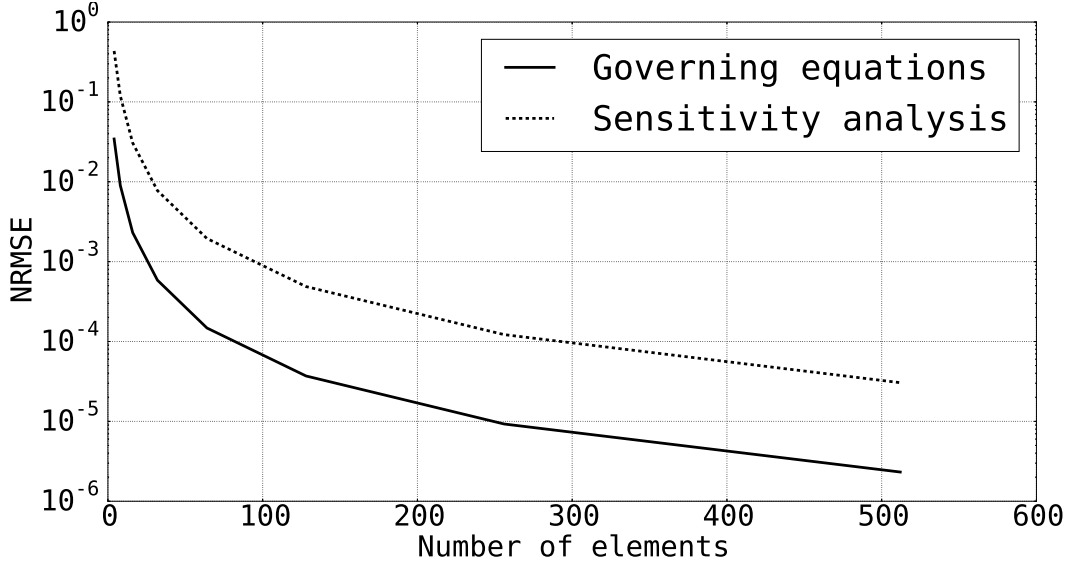


Figure 2.9: Mesh convergence of the discrete sensitivity analysis for the axial bar.

## 2.4 Continuum Sensitivity Analysis

### 2.4.1 Formulation

For a continuous system, the governing equations and boundary conditions are written as

$$A(\mathbf{u}, t; \mathbf{b}) = \mathbf{0} \quad \text{on } \Omega \quad (2.23a)$$

$$B(\mathbf{u}, t; \mathbf{b}) = g(\mathbf{x}, t; \mathbf{b}) \quad \text{on } \Gamma \quad (2.23b)$$

where  $\mathbf{u}$  is the response variable, i.e. displacement or pressure,  $t$  is time,  $x$  is the spatial coordinate, and  $\mathbf{b}$  is the design variable that can be used to control the solution.  $A$  and  $B$  are continuum functions that define the governing equations and boundary conditions, respectively. It should be noted that the governing equation is written in the residual form

where its value needs to be equal to zero when  $u$  is the solution at time  $t$ .  $g$  is the value of the boundary condition of the defined system. To calculate the response sensitivity, the total derivative of Equation (2.23) is required. This is done by determining the local sensitivity of the governing equation followed by converting the local sensitivities to their total form using Equation (2.2).

The governing equation while the boundary condition of (2.23) is differentiated as follows

$$A(u', t; b) + A'(u, t; b) = 0 \quad \text{on } \Omega \quad (2.24a)$$

$$B(\dot{u}, t; b) + \dot{B}(u, t; b) = \dot{g}(x, t; b) \quad \text{on } \Gamma \quad (2.24b)$$

where  $( )'$  indicated local derivative and  $( \cdot )$  indicated total derivative.

$$\begin{aligned} ( )' &= \frac{\partial( )}{\partial b} \\ (\cdot) &= \frac{D( )}{Db} \end{aligned}$$

It should be noted that the governing equations are differentiated in the local form, and the boundary conditions are differentiated in the total form. Local differentiation of the governing equations enables us to treat the solver non-intrusively [22]. However, to capture the effect of shape change, the boundary conditions need to be differentiated in the total form. The boundary condition definition is further simplified by assuming the **B** operator is linear and remains the same throughout the analysis. This is a valid assumption for many practical cases such as structural analysis or computational fluid dynamics. The boundary conditions are typically in the form of known gradient or values, i.e. outflow and free-slip wall for CFD and predefined displacement/force for structural analysis. It should be noted that this assumption is not valid for problems such as contacts. The boundary condition is

written as:

$$\begin{aligned} B(\dot{u}, t; b) &= \dot{g}(x, t; b) \Rightarrow \\ B(u', t; b) &= \dot{g}(x, t; b) - B\left(\frac{\partial u}{\partial x} \cdot \frac{\partial x}{\partial b}, t; b\right) \end{aligned} \quad (2.26)$$

To study the differentiated governing equation (2.24), we will assume two situations: i) linear analysis and ii) nonlinear analysis.

For a linear analysis, the governing of (2.24) is written as:

$$A(u', t; b) = 0 \quad (2.27)$$

This is valid for the linear case because the differential operators of the governing equation do not depend on the response variable,  $u$ . To explain this concept we look at the transient heat conduction in a 1D domain. The governing equations are defined as

$$\frac{\partial^2 T}{\partial x^2} = \frac{1}{\alpha} \frac{\partial T}{\partial t} \quad (2.28)$$

where  $T$  is temperature,  $x$  is spatial coordinate,  $t$  is time, and  $\alpha$  is thermal diffusivity ( $k/\rho c_p$ ). This equation can be differentiated with respect to a design variable  $b$  as shown in the following equation.

$$\frac{\partial}{\partial b} \left( \frac{\partial^2 T}{\partial x^2} \right) = \frac{\partial}{\partial b} \left( \frac{1}{\alpha} \frac{\partial T}{\partial t} \right)$$

Due to linearity of the differential operators we can change the order of differentiation as follows:

$$\frac{\partial^2}{\partial x^2} \left( \frac{\partial T}{\partial b} \right) = \frac{1}{\alpha} \frac{\partial}{\partial t} \left( \frac{\partial T}{\partial b} \right) \quad (2.29)$$

By comparing Equations (2.28) and (2.29) we can see that the differential operators  $\partial^2/\partial x^2$  and  $\partial/\partial t$  remain unchanged. Therefore the same solver can be used for solving this system

of governing equations and for the sensitivity variable,  $\partial T/\partial b$ .

For nonlinear problems, the differential operators are functions of the response variables as well. For example, the incompressible Euler's equation for a 2D flow is derived as

$$\frac{\partial u}{\partial t} + u \frac{\partial u}{\partial x} + v \frac{\partial u}{\partial y} + \frac{\partial p}{\partial x} = 0 \quad (2.30a)$$

$$\frac{\partial v}{\partial t} + u \frac{\partial v}{\partial x} + v \frac{\partial v}{\partial y} + \frac{\partial p}{\partial y} = 0 \quad (2.30b)$$

where  $u$  and  $v$  are the velocity components in  $x$  and  $y$  directions, respectively.  $p$  is pressure,  $t$  is time, and  $x$  and  $y$  are spatial coordinates. We can rewrite Equation (2.30) in terms of differential operators as well.

$$\mathcal{T}u + \mathcal{C}u + \mathcal{G}_x p = 0$$

$$\mathcal{T}v + \mathcal{C}v + \mathcal{G}_y p = 0$$

where  $\mathcal{T}$  is the time derivative operator ( $\partial/\partial t$ ) and  $\mathcal{C}$  is the convective operator

$$\mathcal{C} = u \frac{\partial}{\partial x} + v \frac{\partial}{\partial y} \quad (2.32)$$

and  $\mathcal{G}_x$  and  $\mathcal{G}_y$  are gradient operators in  $x$  and  $y$  respectively ( $\partial/\partial x$  and  $\partial/\partial y$ ). The gradient and time derivative operators are linear; therefore, they can be treated as shown earlier. On the other hand, the convective operator is nonlinear and should be differentiated with respect to the response variables as well. As a result, the sensitivity equations can be written

in the operator form as

$$\mathcal{T}u' + \mathcal{C}'u + \mathcal{C}u' + \mathcal{G}_x p' = 0 \quad (2.33a)$$

$$\mathcal{T}v' + \mathcal{C}'v + \mathcal{C}v' + \mathcal{G}_y p' = 0 \quad (2.33b)$$

where

$$\mathcal{C}' = u' \frac{\partial}{\partial x} + v' \frac{\partial}{\partial y}$$

Several interesting properties of CSA can be explained using Equation (2.33). Importantly, although the original Euler equation is nonlinear due to the multiplication of response variables and their derivatives ( $u$  and  $\partial u / \partial x$ ), the resulting sensitivity equation is linear. This means that the sensitivity equations are easier and quicker to solve compared to the original equations. The challenging expression that needs to be calculated in Equation (2.33) is the convective term derivative.

The first step in solving the sensitivity equations is to find the solution of the governing equations. This enables us to calculate the convective operator,  $\mathcal{C}$ , at each step of sensitivity solution based on the analysis data.  $\mathcal{C}'$  is also calculated at each step of the solution of sensitivity equations based on the solution of the previous time step. For a simple predictor-corrector method used to solving the original governing equations, this can be written as follows for the sensitivity equation in  $x$  direction.

$$\begin{aligned} \bar{u}' &= u'(i) - \Delta t [\mathcal{C}'(i)u(i) + \mathcal{C}(i)u'(i) + \mathcal{G}p'(i)] && : \text{predictor} \\ u'(i+1) &= u'(i) + \frac{\Delta t}{2} - [\mathcal{C}'(i)u(i) + \mathcal{C}(i)u'(i) + \\ &\quad \mathcal{G}p'(i) + \bar{\mathcal{C}}(i)u(i) + \mathcal{C}(i)\bar{u} + \mathcal{G}p'(i)] && : \text{corrector} \end{aligned}$$

Here,  $\bar{\mathcal{C}}$  in the convective operator is evaluated using  $\bar{u}$ . It should be noted that to generate the operator we do not need to know the details of how it has been constructed. We only

supply the required values of the state variables for generating the convective operator; the black-box solver will generate it for us. This input is the response variable when solving the governing equation and is the sensitivity of response variable for sensitivity analysis. Therefore, the solver can still be considered as a black box that we do not modify.

### 2.4.2 Implementation on heat transfer problem

In this section, the continuum sensitivity formulation is used for calculating the sensitivity of temperature with respect to the length of a 1D domain. The domain is defined in Figure 2.2 with the temperature in the domain governed by Equation (2.4). The boundary conditions are defined as  $T_0$  at  $x = 0$  and  $T_L$  at  $x = L$ .

To get the sensitivity equations, governing equations are differentiated in the local form and boundary conditions are differentiated in total form as shown in Equation (2.34).

$$\frac{\partial}{\partial L} \left( \frac{\partial^2 T}{\partial x^2} = 0 \right) \quad (2.34)$$

Since the differential operator is linear, the order of differentiations is changed. This will give us the Equation (2.35) for the sensitivity calculation.

$$\frac{\partial^2}{\partial x^2} \left( \frac{\partial T}{\partial L} \right) = 0 \quad (2.35)$$

The boundary conditions for this problem are written as follows to be consistent with the general formulation of the boundary conditions.

$$\begin{cases} \mathcal{B}T = T_0 & \text{at } x = 0 \\ \mathcal{B}T = T_L & \text{at } x = L \end{cases} \quad (2.36)$$

Where  $\mathcal{B}$  is the operator acting on the boundary. For this problem, it is equal to 1. Equation

(2.36) is differentiated in the total form, since the boundaries are moving. This results in

$$\begin{cases} \dot{\mathcal{B}}T + \mathcal{B}\dot{T} = \dot{T}_0 & \text{at } x = 0 \\ \dot{\mathcal{B}}T + \mathcal{B}\dot{T} = \dot{T}_L & \text{at } x = L \end{cases} \quad (2.37)$$

where  $\mathcal{B}$  and  $\dot{T}_0$  are constants and have zero derivatives.  $\dot{T}$  is written in terms of the local derivative and convective terms using the chain rule. This results in the following definition for the sensitivity equation boundary conditions.

$$\begin{cases} \frac{\partial T}{\partial b} = -\frac{\partial T}{\partial x} \frac{\partial x}{\partial b} & \text{at } x = 0 \\ \frac{\partial T}{\partial b} = -\frac{\partial T}{\partial x} \frac{\partial x}{\partial b} & \text{at } x = L \end{cases}$$

To calculate the mesh sensitivity at the boundary, the dependency of the spatial variable,  $x$ , and the shape of the domain,  $L$ , need to be known. For the 1D domain, this is defined as follows:

$$x = \alpha L$$

This means that every location in the domain can be defined using a nondimensional variable,  $\alpha$ , times the total length of the domain. Using this formulation, the sensitivity of spatial coordinate,  $x$ , with respect to the length of the domain is defined as:

$$\frac{\partial x}{\partial L} = \alpha \quad \text{where} \quad \alpha = \frac{x}{L}$$

By using this relation, the boundary conditions can be written as:

$$\begin{cases} \mathcal{B} \frac{\partial T}{\partial b} = -\frac{\partial T}{\partial x} \frac{x}{L} & \text{at } x = 0 \\ \mathcal{B} \frac{\partial T}{\partial b} = -\frac{\partial T}{\partial x} \frac{x}{L} & \text{at } x = L \end{cases}$$

This can be further simplified by substituting  $x$  in the definition of boundary conditions. We also substitute  $\mathcal{B}$  as 1.

$$\begin{cases} \frac{\partial T}{\partial b} = 0 & \text{at } x = 0 \\ \frac{\partial T}{\partial b} = -\frac{\partial T}{\partial x} & \text{at } x = L \end{cases} \quad (2.38)$$

The last thing to be noted is the spatial derivative of response variable at the boundaries,  $\partial T / \partial x$ . This term appears due to the boundary movement with a change in shape design variable when using the chain rule. This term is calculated from the analysis results by using the same technique used for discretizing the governing equations. For this problem, the finite difference method is used to calculate this derivative from the analysis results.

The governing equation of (2.35) with boundary condition (2.38) is solved using the same solver that we used for solving the original governing equation since these two are effectively having the same form. The comparison between the original governing equation and the sensitivity equation is shown in Table 2.3. The continuum sensitivity analysis

Analysis Type	Equation	Unknown	Discretized form	Discretization
Governing equation	$\partial^2 T / \partial x^2$	$T$	$[K][T] = [F_{BC}]$	Central difference
Sensitivity equation	$\partial^2 T' / \partial x^2$	$T'$	$[K][T'] = [F'_{BC}]$	Central difference

Table 2.3: Comparison between the governing and sensitivity equations.

(CSA) result is verified using the analytical solution of Equation (2.5) as shown in Figure 2.10. Different number of discretization nodes are used for the comparison between the results. For the qualitative comparison between the results, the NRMSD as defined in Equation (2.16) is used. As shown if Figure 2.10 and Table 2.4, the two results match perfectly.

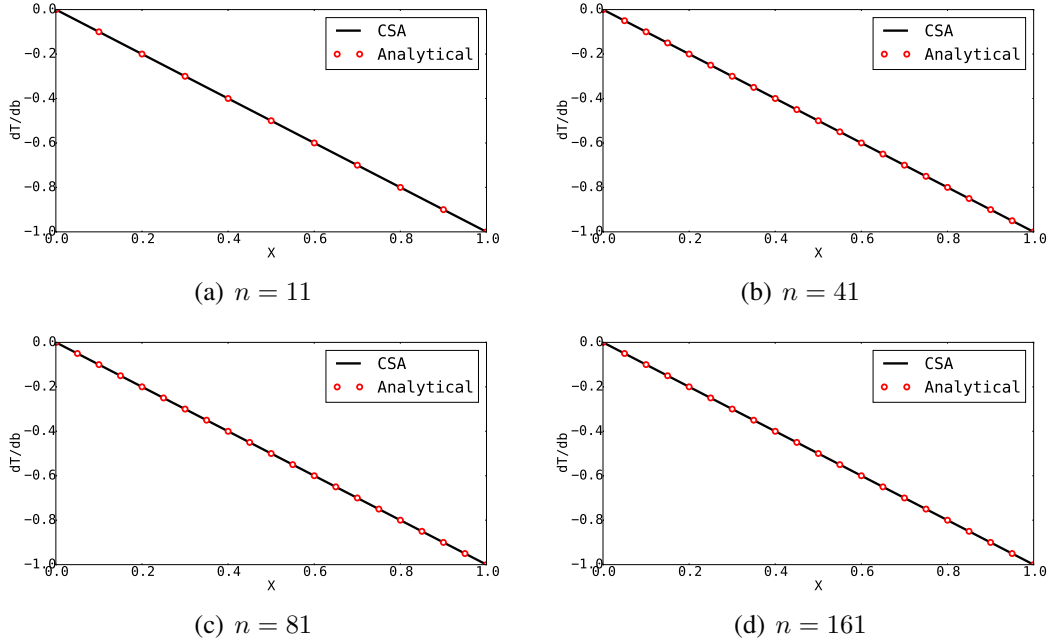


Figure 2.10: Comparison between continuum sensitivity analysis and analytical results for different number of nodes.

Number of nodes	NRMSD
11	$6.96 \times 10^{-17}$
41	$2.02 \times 10^{-15}$
81	$1.43 \times 10^{-15}$
161	$2.77 \times 10^{-15}$

Table 2.4: RMSE value for different number of nodes.

It should be noted that the sensitivity equations are derived and solved in the local form. This does not include the effect of nodes moving in the computational domain. If the analysis requires the sensitivity at the material points, an additional step is required to convert the local sensitivities to their total form using the chain rule as shown in the following equation.

$$\frac{DT}{Db} = \frac{\partial T}{\partial b} + \frac{\partial T}{\partial x} \cdot \frac{\partial x}{\partial b}$$

This will add an extra cost to the simulation due to the additional step for calculating  $\partial x / \partial b$ . The reason this step exists is due to movement of computational nodes as the results of a change in shape. Therefore, if the computational nodes can be fixed, the  $\partial x / \partial b$  term will

be equal to zero. We have achieved this using a non-body conformal technique such as immersed boundary method. This will be explained in the next chapter in more detail.

### 2.4.3 Implementation on solid mechanics problem

To derive the continuum sensitivity equations, the governing equation of (2.7a) is differentiated with respect to the design variable,  $L$ , as shown in Equation (2.39).

$$\frac{\partial^2}{\partial x^2} \left( \frac{\partial u}{\partial L} \right) - \frac{\pi x}{L^2} \cos \left( \frac{\pi x}{L} \right) = 0 \quad (2.39)$$

The boundary conditions are calculated by differentiating the boundary conditions defined in Equation (2.7b). It should be noted that the boundary conditions are differentiated in total form.

$$\begin{cases} \frac{\partial}{\partial x} \left( \frac{\partial u}{\partial L} \right) \Big|_{x=0} = \frac{\partial}{\partial L} \left( \frac{1}{\pi} \right) = 0 \\ \frac{\partial}{\partial x} \left( \frac{\partial u}{\partial L} \right) \Big|_{x=L} = \left\{ K \left[ \frac{\partial u}{\partial L} + \frac{\partial u}{\partial x} \frac{\partial x}{\partial L} \right] - \frac{\partial^2 u}{\partial x^2} \frac{\partial x}{\partial L} \right\} \Big|_{x=L} \end{cases} \quad (2.40)$$

For this problem, the spatial coordinate  $x$  is defined as  $x = \zeta L$  where  $\zeta = x/L$ . Therefore, the design velocity  $\partial x/\partial L$  at  $x = L$  is equal to one. Solving the governing equation (2.39) along with boundary conditions (2.40) leads to the sensitivity values of displacement in the domain,  $\partial u/\partial L$ . Comparing the sensitivity equation and boundary conditions (2.39) and (2.40) to the governing equation and its corresponding boundary conditions of (2.7a) and (2.7b), it is safe to say that these equations are the same. The only difference is their boundary conditions. Therefore, the same numerical solver that was used for solving the governing equation can be used to solve the sensitivity equations without any modifications. The only change would be in the values of the boundary conditions. However, change in the boundary conditions does not alter the structure of the black box solver.

To calculate the sensitivities, the governing equation and boundary conditions of (2.39) and (2.40) are discretized using the finite element method as discussed through equations (2.17) and (2.18). It should be noted that  $[K]$  and  $[K_s]$  are the same matrices that used in Equation (2.17),  $[F_p]$  is equal to zero, and  $F_d = -\frac{\pi x}{L^2} \cos\left(\frac{\pi x}{L}\right)$ . For verification, the results for the sensitivity analysis are compared with the analytical results of sensitivity as defined by Equation (2.9). We used the NRMSE metric to compare the two different results as defined in Equation (2.19). The comparison of the results are shown in Figure 2.11. As shown here, for the interior elements of the structure, the results for both discrete and continuum sensitivity analysis converge with the same rate.

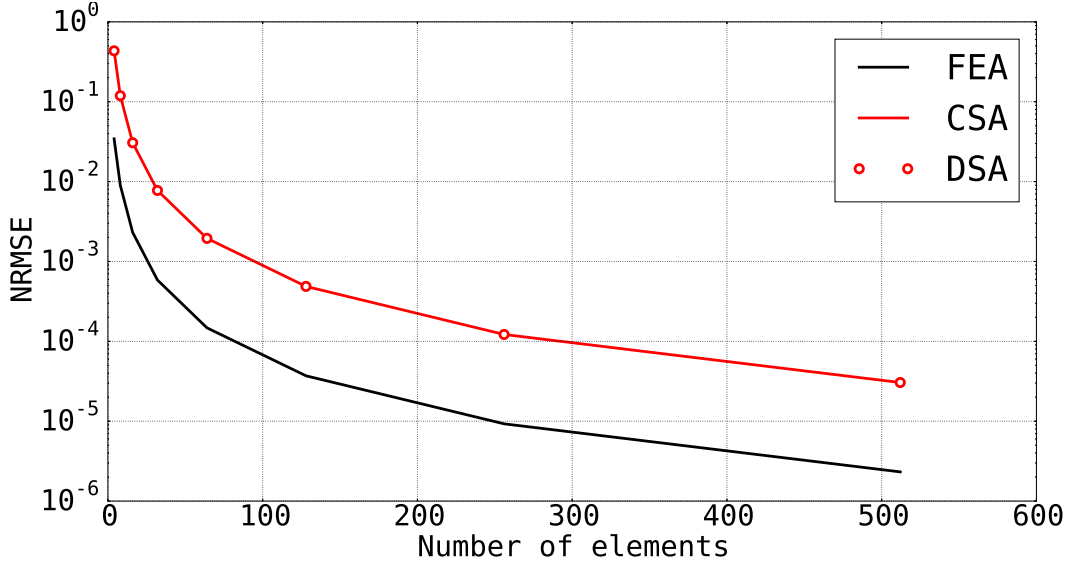


Figure 2.11: Mesh convergence of the continuum (CSA) and discrete (DSA) sensitivity equations for axial bar problem. The results for the convergence of the analysis (FEA) is also included in this graph.

## 2.5 Summary

In summary, we looked at two main approaches used to calculate the sensitivity response of a system. The discrete method is based on differentiating the discretized governing equations whereas in continuum method, the governing equation are differentiated first and then

discretized. We applied these techniques on a simple 1D heat transfer problem and calculated the response sensitivity to shape design parameter. The sensitivities are calculated in the local form for each of these methods and compared with the analytical results where they show good comparison. It is shown that by using the continuum sensitivity analysis, the differential operators used in the solution of governing equations are reused in the sensitivity analysis. This effectively means that the black-box solver used in the simulation step can be reused with new boundary conditions for solving the sensitivity response. Therefore, more details about the analysis needs to be known when using discrete approach compared to the continuum. Continuum sensitivity approach is used in this research due to its ability to treat the analysis as a black-box for solving both the governing equations and the sensitivity response. However, the result of sensitivity analysis is still the local sensitivities, which needs to be transformed to the total form using the chain rule.

# Chapter 3

## Immersed Boundary Method

Immersed boundary methods are a class of techniques in computational fluid dynamics where the governing equations are solved on a Cartesian grid that does not conform to the shape of the body in the flow. This representation of solid boundaries is opposed to well known body-conformal techniques where the computational mesh accurately represents the shape of the domain. The boundary condition on the immersed surfaces are not applied explicitly; instead, an extra forcing function is added to the governing equations or the discrete numerical scheme is updated near the boundary. The immersed boundary technique is, in particular, of interest to us, since it removes the mesh sensitivity calculation from the analysis. In this chapter we talk about different classes of immersed boundary technique and apply them to a simple problem. The applicability of these methods in the continuum sensitivity analysis is also discussed. At the end of this chapter, we chose a couple of immersed boundary techniques for sensitivity analysis implementation.

### 3.1 Introduction

When people started to use computational models in the design of systems, it was usually sufficient to include single physics in the design. The simulations were usually based on structural solvers using finite element analysis (FEA) or computational fluid dynamics (CFD) simulations. The advanced requirements such as higher fuel efficiency, improved controllability, higher stiffness to mass ratios, and lower radar signature have forced the designers to develop more unconventional configurations. For example, one way to reduce the infra-red signature of an aircraft is to remove the engines from underneath the wings and place them inside the aircraft. However, by doing this, a massive heat source will be added to the structure. The thermal expansion due to this excessive heat load needs to be incorporated into the structural analysis of the system. This requires a multidisciplinary analysis combining thermal analysis for heat transfer and structural analysis for thermal expansion, and other structural loads [69]. However, this has not been a traditional design method. Only recently designers have started to look into such configurations.

Multidisciplinary analysis is required for many engineering applications; however, the most frequently used is the interaction of fluid and a deformable structure. This problem is commonly known as a Fluid-Solid Interaction (FSI) problem. FSI problems are dealt with in many different engineering applications such as fluttering and buffeting of bridges [70], the vibration of wind turbine blades [71], and aeroelastic response of airplanes [72]. FSI problems are also seen in arterial blood flow and artificial heart valves [73], flying, and swimming [74]. The conventional approach for simulations with large structural deformation/movement is the Arbitrary Lagrangian-Eulerian (ALE) method. ALE methods are based on body-conforming grids to track the location of the fluid-structure interface. ALE methods have been applied to many FSI problems. However, they are cumbersome, if not impossible, to apply to FSI problems with large deformations for complicated boundary shapes.

Immersed boundary (IB) methods are considered a separate family of methods used

for modeling FSI problems with complex boundary shapes and large deformations. IB methods are based on solving the governing equations for fluids on a fixed grid. Although this computational grid can be structured (Cartesian) or unstructured, most methods are based on structured grids because of the simplicity of grid generation. Moreover, when using a structured grid, extremely efficient computational methods can be utilized to solve the governing equations. In IB approach, the fluid-structure boundaries are represented by a set of independent nodes. The solid boundary effect on the flow is formulated either by introducing fictitious body forces in the governing equations or by locally modifying the structure of the background grid. This means that the computational mesh is modified near the solid domain as the boundary deforms. However, the rest of the computational domain will remain fixed.

IB has several advantages over the ALE technique. The major advantage is the simplification of the task of grid generation. Generating a body-conformal grid for a complex shape is usually very complicated. The objective is to construct a grid that provides adequate local resolution with the minimum number of total grid points. Grid generation requires a significant input from the user and is an iterative process. For complicated boundaries, the unstructured grid approach is better suited; however, the grid quality is reduced for extremely complex geometries. In contrast, for a simulation carried out using an IB method, grid complexity and quality are not affected by the complexity of the geometry.

This advantage becomes even more evident for flows with moving boundaries. The ALE approach requires generating a new mesh or deforming the original mesh to match the new boundary shape at each time step. The solution from the last time step is also required to be projected to this new computational mesh. Both deformation/projection can affect the accuracy, robustness, and the computational cost associated with the simulation. On the other hand, the boundary motion in IB method can be handled with relative ease, because the computational mesh does not depend on the shape of the boundary. Therefore, although a significant progress in simulating flows using ALE methods has been made in

recent years [75, 76, 77], the IB method remains an attractive alternative for such problems due to its simplicity and cost.

In the following sections of this chapter we first look at the governing equations for the fluid and solid domains. Following this, different approaches for modelling the flow using IB method are discussed in detail. We apply different IB techniques to a simplified problem to compare the efficiency and simplicity of implementation. The results are compared with body-conformal solution approach for accuracy. Finally, we assess different IB methods with regards to their applicability of the Continuum Sensitivity Analysis (CSA) framework.

## 3.2 Governing Equations

In the fluid region  $\Omega_f$ , the governing equations for incompressible flow of a Newtonian fluid are known as Navier-Stokes (NS) equations. In the compact indicial notation, the NS equations are written as

$$\frac{\partial u_i}{\partial x_i} = 0 \quad (3.1a)$$

$$\frac{\partial u_i}{\partial t} + \frac{\partial u_i u_j}{\partial x_j} = -\frac{1}{\rho_f} \frac{\partial p}{\partial x_i} + \nu \frac{\partial}{\partial x_j} \left( \frac{\partial u_i}{\partial x_j} \right) + f_i \quad (3.1b)$$

where the repeated indices imply summation and  $i, j = 1, 2, 3$ .  $x_i$  are the spatial coordinates,  $u_i$  are the velocity components of the fluid in  $i$  direction,  $\rho_f$  is the fluids density,  $p$  is the pressure,  $\nu$  is the kinematic viscosity, and  $f_i$  are body forces. These forces are used in the IB technique to represent the effect of immersed boundaries on the fluid. In general purpose CFD solvers, due to the use of an unstructured grid to represent the shape, it is usually required to use mappings (Jacobian) to convert the physical coordinate to a computational coordinate. This will become problematic when we have skewed elements that cause the mapping to become singular. This step is removed in the IB approach, since the governing equations (3.1) are discretized on a Cartesian grid.

The solid domain is modelled using a linear elastic theory in this work. The governing

equations are written as

$$\sigma_{ji,j} + F_i = \rho_s \partial_{tt} d_i \quad (3.2a)$$

$$\epsilon_{ij} = \frac{1}{2} (d_{j,i} + d_{i,j}) \quad (3.2b)$$

$$\sigma_{ij} = C_{ijkl} \epsilon_{kl} \quad (3.2c)$$

where  $\sigma$  is the Cauchy stress tensor,  $\epsilon$  is the strain tensor,  $d$  is the displacement vector,  $C$  is stiffness tensor,  $F$  is the body force, and  $\rho_s$  is the mass density of solid. These governing equations are solved to track the motion of the solid boundary. We had to use  $d$  for displacement so that the notation won't be confused with the  $u$  velocity in the Navier-Stokes equations.

To solve the coupled system of equations of (3.1) and (3.2), we need to have boundary conditions. The boundary conditions of (3.1) are defined as pressure or velocity magnitudes on the outer boundaries of the domain. After solving Equation (3.1), the loads on the structure are calculated by integrating the fluid pressure over the solid boundaries. The resulting force will be the boundary load used for solving Equation (3.2). When the governing equations for the solid region are solved, the displacements of the solid domain are known. This is fed into the CFD solver to update the solid boundary location for the fluid domain. This will change the solution of fluid's solver resulting in different pressure distributions. This process is repeated until convergence is satisfied. The convergence can be defined as a change in the structural deflection for two subsequent steps in a static problem.

### 3.3 Fluid Dynamics Benchmark Case

We define a 1D benchmark problem to investigate different IB formulations in detail. In one dimensional space the equations of incompressible flow are not challenging; also, it is not simple to write a one-dimensional analogue of the IB to capture all of its features. However,

for a simpler one dimensional problem it is easier to understand different formulations of IB method and later apply IB to higher dimensions. Moreover, the sensitivity analysis is better understood. The other reason for working with a simplified model is the availability of analytical results that can be used for verifying the results we get from the numerical solvers. As the final note, for this benchmark case we mainly focused on the fluid domain; the structural behaviour can be easily added to this formulation.

The one dimensional benchmark case is derived by starting with the Navier-Stokes equations. A viscous incompressible fluid in the channel  $0 \leq y \leq 1$ ,  $-\infty < x < \infty$  as shown in Figure 3.1 is considered.

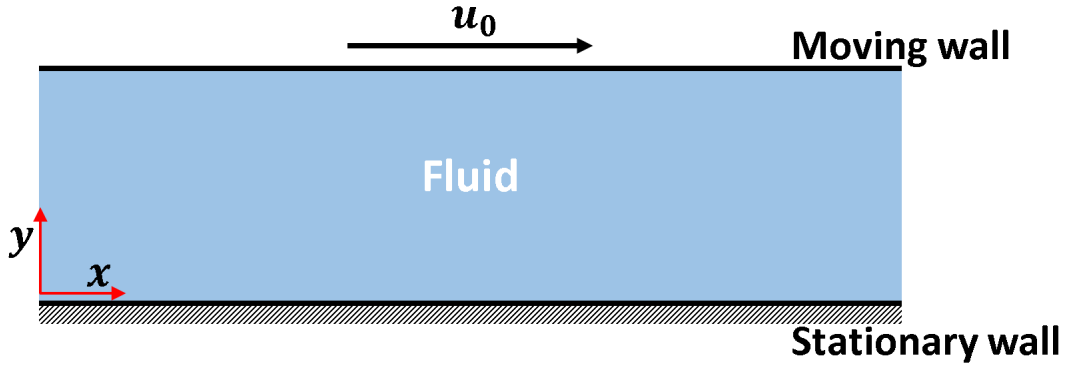


Figure 3.1: 1D benchmark case for IB method.

We can also assume that the boundary conditions are periodic in  $x$ . Assume that there is a horizontal plate running through the length of this channel at  $y = y_0$  and moving with  $u_0$  velocity in the horizontal direction. We assume no-slip condition where the fluid and the plate meet. The wall velocity will force the fluid to accelerate in  $x$  direction due to the viscous stress from the moving plate. We expect no motion in  $y$  direction and drop all terms in the NS equations containing  $u_y$  velocity. Due to the continuity equation (3.1a), there is no variation in  $x$  direction so we can drop all terms that involve  $x$  variation as well. This enables us to simplify the NS equation of (3.1b) to Equation (3.3). It should be noted

that the continuum equation (3.1a) is automatically satisfied.

$$u_t = \mu u_{yy} \quad \text{in } \Omega_f \quad (3.3a)$$

$$\begin{cases} u = u_0 & \text{at } y = 1 \\ u = 0 & \text{at } y = 0 \end{cases} \quad (3.3b)$$

Equation (3.3) is transient in nature; however, its steady state solution can be calculated by setting the time derivative in Equation (3.3) equal to zero. This equation is commonly known as Couette flow in fluid dynamics. The analytical solution for this equation is shown in Equation (3.4).

$$u = u_0 x \quad (3.4)$$

We will use this analytical solution to verify the results of different IB methods defined in the following sections.

## 3.4 Immersed Boundary Classification

In general, IB methods can be classified in three main families: i) discrete forcing, ii) continuum forcing, and iii) cut-cell methods. This classification is based on how the interface conditions are handled in the IB algorithm. In this section we present the essence of each method and attempt to point out their primary advantages and disadvantages. In general, the immersed boundary approach is based on modifying the NS equations for imposing the boundary conditions and leads to one of the three categories.

## 3.5 Discrete Forcing Method

The discrete forcing approach was first introduced by Mohd-Yusof [48] in late nineties. The discrete forcing approach is based on defining the force term in the numerical solution from the known characteristic of the response. For the case of flow over immersed boundaries, this known feature is the flow velocity on the immersed boundary. The general formulation for the discrete forcing method starts with the discretized NS equation

$$\frac{u^{n+1} - u^n}{\Delta t} = RHS^{n+1/2} + f^{n+1/2} \quad (3.5)$$

where  $u^{n+1}$  is the velocity at the next time step,  $u^n$  is the velocity at the current time step,  $\Delta t$  is the time step, and  $RHS^{n+1/2}$  contains both the viscous terms and pressure gradient.  $f^{n+1/2}$  is the forcing term that needs to be calculated in such a way that yields  $u^{n+1} = V$ , where  $V$  is the known velocity of the immersed boundary. Therefore, the force term is calculated as:

$$f^{n+1/2} = -RHS^{n+1/2} + \frac{V - u^n}{\Delta t} \quad (3.6)$$

Equation (3.6) is valid only if the location of the immersed boundary coincides with the computational nodes. Interpolation from the fluid's computational nodes to the immersed boundary is needed for the cases where the two do not coincide. Depending on how this interpolation is done and where the force terms are calculated, the discrete forcing immersed boundary method is put into two main families.

### 3.5.1 Indirect Forcing Method

In the indirect forcing method, the boundary conditions are imposed through a set of forcing terms on nodes near the boundary. These forcing terms are calculated based on the interpolation of a known condition on the immersed boundary from the discretized equations. The forces are applied using delta functions to nodes near the immersed boundary.

The interpolation is done as shown in Figure 3.2.

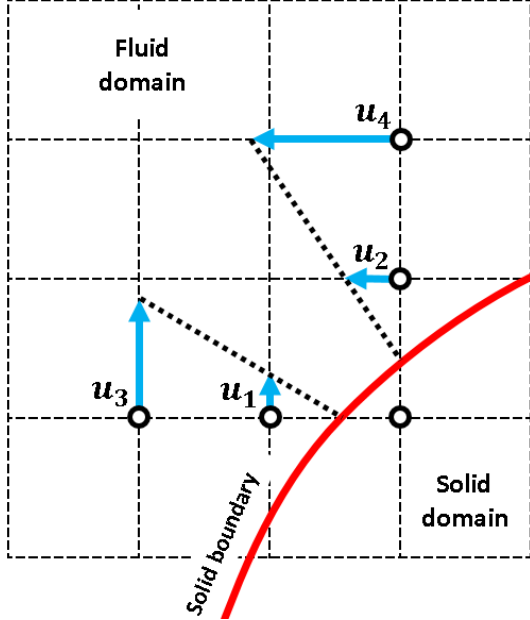


Figure 3.2: Indirect forcing approach for boundary representation. Desired velocity values at nodes 1 and 2 are interpolated from wall velocity and results from nodes 3 and 4.

The force terms are applied on nodes 1 and 2 based on the known zero velocity on the wall and calculated velocities at nodes 3 and 4. Linear interpolation is used to calculate required velocities at nodes 1 and 2, so that it results in zero velocity on the immersed boundary. These known velocities are then employed in Equation (3.6) to calculate the forcing values. This forcing value is then used in Equation (3.5) to compute the velocity field at the following time step.

To investigate the indirect forcing approach, we apply this methodology to the benchmark problem. We investigated three different cases: effect of wall location, the impact of the number of nodes, and effect of wall velocity. In the first case, the wall velocity was  $1\text{m/s}$  with 41 nodes to discretize the domain. The time step of this simulation is selected as  $10^{-3}$ . The governing equations are discretized using the Euler method in time and a second-order finite difference method in space as shown in the following equation.

$$\frac{u(i, n+1) - u(i, n)}{\Delta t} = \frac{u(i-1, n) - 2u(i, n) + u(i+1, n)}{(\Delta x)^2} + f(i, n) \quad (3.7)$$

where  $u(i, n)$  is the fluid velocity at location  $i$  and time  $n$ ,  $\Delta x$  is the nodal distances in space,  $\Delta t$  is the nodal distance in time, and  $f(i, n)$  is the forcing function value at location  $i$  in time  $n$ . The forcing function is calculated using linear interpolation based on zero slip condition on the wall. The results for different locations of the fixed wall are shown in Figure 3.3 and Table 3.1. The wall location is selected as 0.178, 0.351, 0.612, and 0.842. As shown here, the wall location with respect to computational nodes does not affect the solution accuracy.

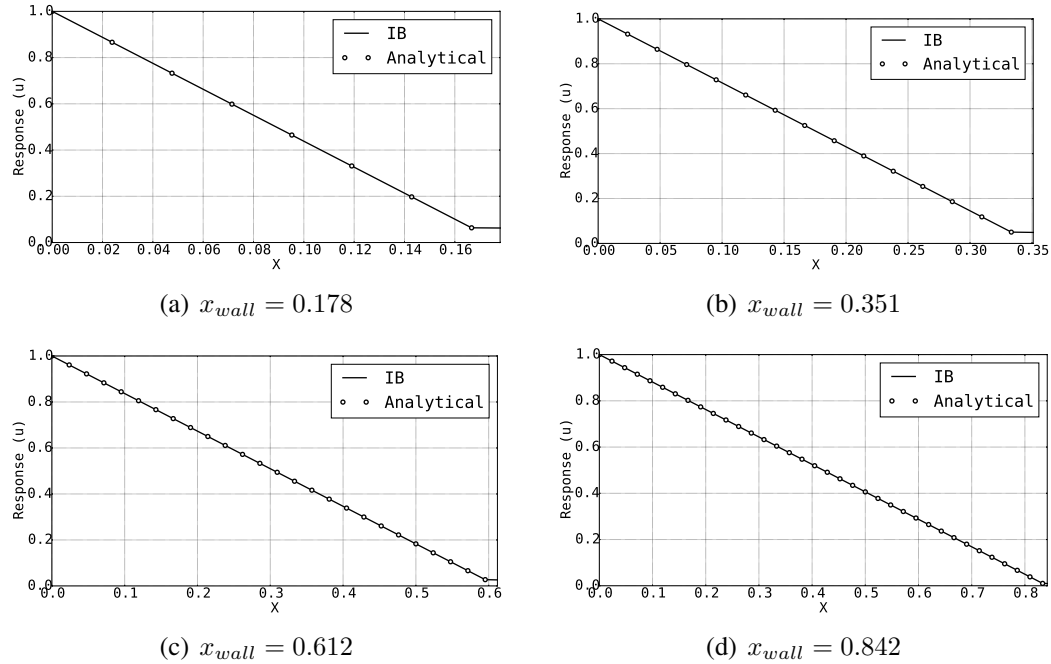


Figure 3.3: Comparison between IB and analytical results for different wall locations.

Wall location	RMSE value
0.178	$1.61 \times 10^{-15}$
0.351	$2.29 \times 10^{-15}$
0.612	$1.72 \times 10^{-15}$
0.842	$3.81 \times 10^{-15}$

Table 3.1: RMSE value for different wall locations for Couette flow problem.

For the second case, we looked at the effect of the number of nodes on the accuracy of the simulation using indirect forcing method. The wall velocity was fixed at  $1m/s$  and

the stationary wall is located at 0.5741. The number of nodes is chosen as 11, 41, 81, and 161. As can be seen in Figure 3.4 and Table 3.2, the number of nodes does not affect the accuracy of indirect forcing approach.

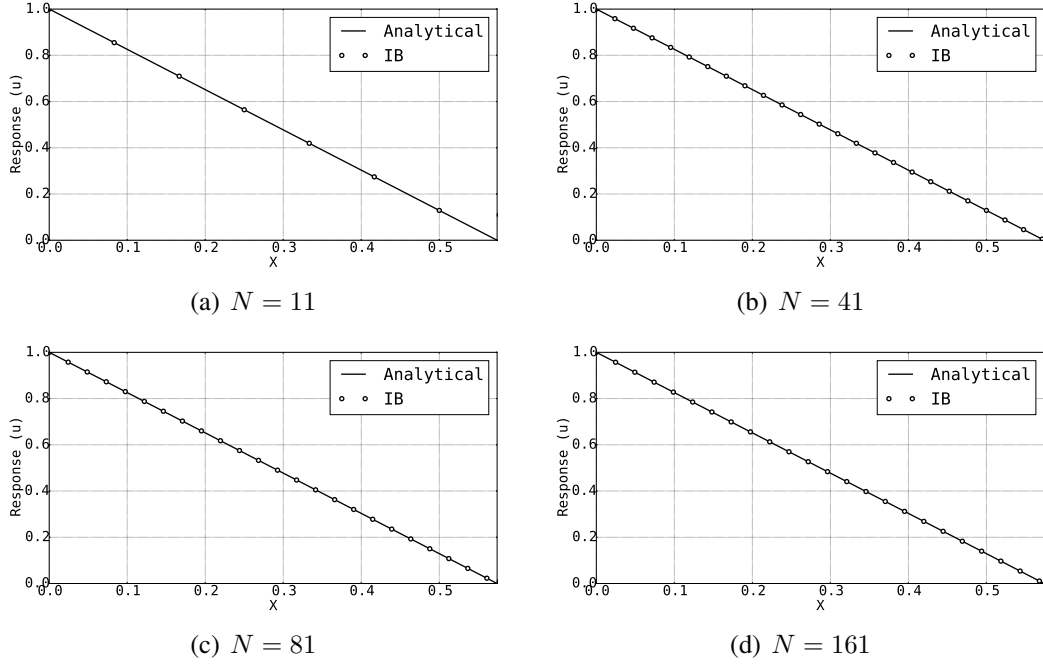


Figure 3.4: Comparison between IB and analytical results for different number of nodes.

Number of nodes	RMSE value
11	$1.20 \times 10^{-15}$
41	$1.50 \times 10^{-15}$
81	$5.64 \times 10^{-15}$
161	$3.76 \times 10^{-15}$

Table 3.2: RMSE value for different number of nodes for Couette flow problem.

For the final case, we looked at the effect of wall velocity on the accuracy of the simulation accuracy. The number of nodes is fixed at 41 and the stationary wall is located at 0.5741. The wall velocity is chosen as  $10m/s$ ,  $100m/s$ ,  $1000m/s$ , and  $10000m/s$ . As can be seen in Figure 3.5 and Table 3.3, the wall velocity does not affect the accuracy of the indirect forcing approach.

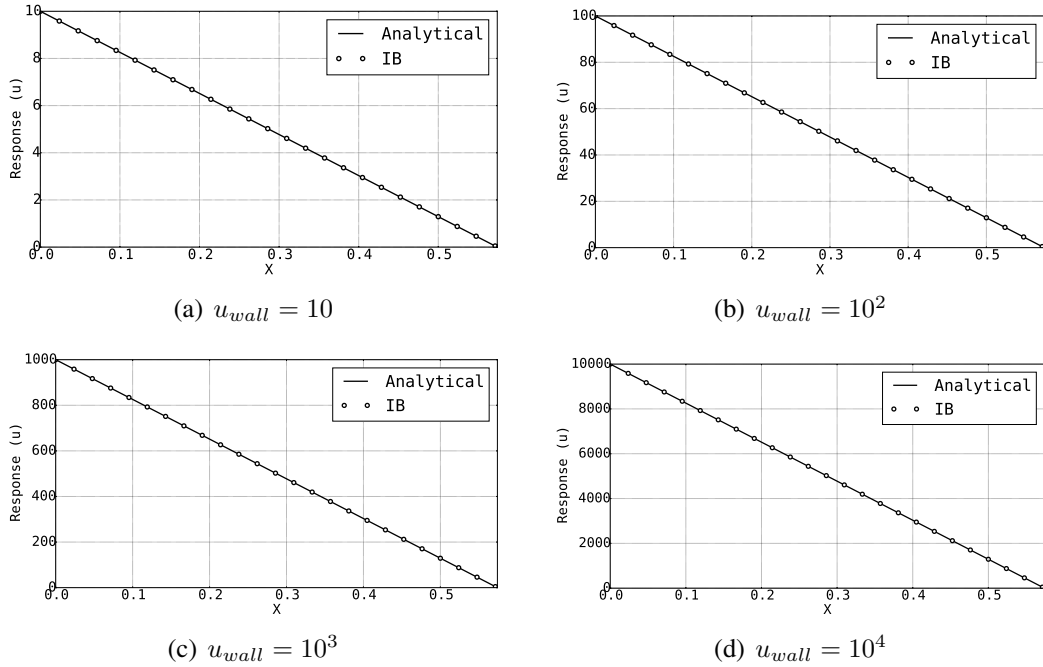


Figure 3.5: Comparison between IB and analytical results for different wall velocities.

Wall velocity	RMSE value
10	$1.49 \times 10^{-14}$
100	$1.52 \times 10^{-14}$
1000	$1.45 \times 10^{-14}$
10000	$1.48 \times 10^{-14}$

Table 3.3: RMSE value for different wall velocities.

### 3.5.2 Direct Forcing Method

In the direct forcing method, the conditions on the immersed boundary are imposed through a set of ghost cells. These are the cells in the solid region that have at least one neighbour in the fluid domain. For example, the node  $\phi$  in Figure 3.6 is a ghost cell.

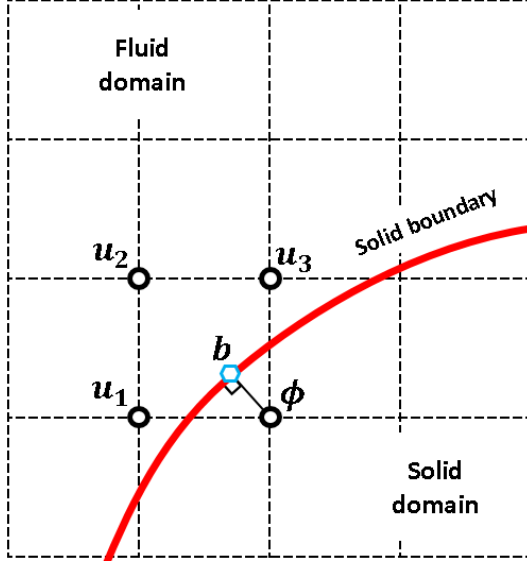


Figure 3.6: Nodes representation in the vicinity of an immersed boundary used in the ghost-cell approach.

For each ghost cell, an interpolation is used to implicitly satisfy the desired value of response on the immersed boundary. The easiest interpolation used is the bilinear interpolation (trilinear in 3D) where the value of  $\phi$  can be defined as

$$\phi = C_1x_1x_2 + C_2x_1 + C_3x_2 + C_4 \quad (3.8)$$

where the four coefficients in Equation (3.8) are calculated based on the values of flow responses at  $U_1$ ,  $U_2$ , and  $U_3$  and the known value at the boundary point,  $b$ . Boundary points  $b$ , is the normal intercept from the ghost node to the immersed boundary. The linear interpolation is well suited for laminar and high Reynolds number flows where the grid points are located in the viscous sublayer [51]. For high Reynolds numbers where higher accuracy is required, higher-order interpolations are used. Majumdat et al suggest an example of such interpolations., where they employed a linear interpolation in the tangential direction and quadratic in the normal direction [78].

In the ghost cell method, the boundary conditions are introduced on the immersed boundary surface directly in the discrete equations. Therefore, the forcing term depends on

the discretization process and its practical implementation is not straightforward compared to the continuous forcing approach that is discussed in the next section. The steps for implementing the ghost cell method can be summarized as follows:

1. Mark computational nodes as fluids, solids, and ghost cells based on their relative location to the boundary
2. For each of ghost cell, define an interpolation scheme based on the neighbouring nodes
3. Update the discretized equations for nodes with ghost cells in their boundaries using the interpolation scheme
4. Solve the resulting equations for the response
5. Update the interpolation scheme and discrete equations based on the new values
6. Iterate until convergence is achieved

The ghost cell method is applied to the benchmark problem introduced in Section 3.3. We chose linear interpolation for this problem, since the velocities are rather small. The effect of the velocity at the moving wall and the number of nodes on the accuracy on the solution is investigated. The IB results are verified using the analytical solution. We derive the ghost cell method by discretizing the domain with six nodes using central difference method. For demonstration we define the wall location between nodes 2 and 3 as shown in Figure 3.7. Thus, node 3 is the ghost cell for this problem.

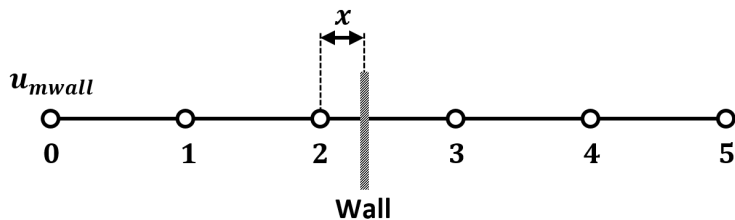


Figure 3.7: Discretized domain for the ghost cell IB method where the “wall” is represented using hashed box.

The solid wall is defined at location  $x$  in the local coordinate of the space between nodes 2 and 3. By using this coordinate and linear interpolation between nodes 2 and 3, the response on the wall is defined as

$$xu_3 + (1 - x)u_2 = u_{mwall} \quad (3.9)$$

Where  $u_i$  is the response at node  $i$  and  $u_{mwall}$  is the predefined velocity at the stationary wall. For this problem, we know that  $u_{mwall}$  is equal to zero; Therefore, the response at the ghost cell,  $u_3$ , needs to be equal to Equation (3.10) to ensure zero velocity on the fixed wall.

$$u_3 = -\frac{1 - x}{x}u_2 \quad (3.10)$$

The second-order central-difference differential operator for this problem is shown in Equation (3.11a). By substituting Equation (3.10) in Equation (3.11a), we modify the differential operator in a way that it incorporates the effect of solid boundary. This modified operator is shown in Equation (3.11b). Since the value of  $u_3$  is known from Equation (3.10), its corresponding equation is removed from Equation (3.11a).

$$L = \begin{bmatrix} 1 & -2 & 1 & 0 & 0 & 0 \\ 0 & 1 & -2 & 1 & 0 & 0 \\ 0 & 0 & 1 & -2 & 1 & 0 \\ 0 & 0 & 0 & 1 & -2 & 1 \end{bmatrix} \quad \text{:original operator} \quad (3.11a)$$

$$L' = \begin{bmatrix} 1 & -2 & 1 & 0 & 0 & 0 \\ 0 & 1 & -2 - (1 - x)/x & 0 & 0 & 0 \\ 0 & 0 & 1 + 2(1 - x)/x & 0 & 1 & 0 \\ 0 & 0 & -(1 - x)/x & 0 & -2 & 1 \end{bmatrix} \quad \text{:modified operator} \quad (3.11b)$$

The differential operator of Equation (3.11b) needs to be updated based on the new location of the wall; this may cause a different column to become zero. As a result, we need to know the discretization technique used in solving the governing equations to implement the ghost cell method. This is usually not possible by means of commercial software.

The Euler method is used for time integration of the discrete equations. In the discrete form, this is written as shown in Equation (3.12a). The time integration also needs to be modified to incorporate the effect of the ghost cell. This is done by including the known value of the ghost cell in the time integration as shown in Equation (3.12b).

$$\begin{bmatrix} 1 & 0 & 0 & 0 \\ 0 & 1 & 0 & 0 \\ 0 & 0 & 1 & 0 \\ 0 & 0 & 0 & 1 \end{bmatrix} \begin{bmatrix} u_1^{n+1} \\ u_2^{n+1} \\ u_3^{n+1} \\ u_4^{n+1} \end{bmatrix} = \begin{bmatrix} 1 & 0 & 0 & 0 \\ 0 & 1 & 0 & 0 \\ 0 & 0 & 1 & 0 \\ 0 & 0 & 0 & 1 \end{bmatrix} \begin{bmatrix} u_1^n \\ u_2^n \\ u_3^n \\ u_4^n \end{bmatrix} + \Delta t L \mathbf{u}^n \quad (3.12a)$$

$$\begin{bmatrix} 1 & 0 & 0 & 0 \\ 0 & 1 & 0 & 0 \\ 0 & 0 & 1 & 0 \\ 0 & 0 & 0 & 1 \end{bmatrix} \begin{bmatrix} u_1^{n+1} \\ u_2^{n+1} \\ u_3^{n+1} \\ u_4^{n+1} \end{bmatrix} = \begin{bmatrix} 1 & 0 & 0 & 0 \\ 0 & 1 & 0 & 0 \\ 0 & -(1-x)/x & 0 & 0 \\ 0 & 0 & 0 & 1 \end{bmatrix} \begin{bmatrix} u_1^n \\ u_2^n \\ u_3^n \\ u_4^n \end{bmatrix} + \Delta t L' \mathbf{u}^n \quad (3.12b)$$

$L'$  is the modified differential operator of Equation (3.11b). It is clear that excessive modification of the discrete solver is required for implementation of the immersed boundary. This discretization method is applied to the benchmark case, where the effect of the number of nodes, location of the stationary wall, and the wall velocity on the solution accuracy is investigated.

For the first case, we look at the effect of the number of nodes. We choose the length of domain as 1m with the wall located at  $x_{wall} = 0.6541$ . The time step is selected as 0.1 with the moving wall velocity as 10m/s. The number of nodes are selected as 11, 41, 81, and 161. We compared the accuracy of the solution with the analytical result. We chose

the normalized root mean square error to compare the analytical and IB results.

$$NRMSE = \sqrt{\frac{\sum_{n=1}^N N (\hat{y}_n - y)^2}{n}} / (y_{max} - y_{min})$$

Where  $\hat{y}_t$  is the predicted value,  $y$  is the actual value, and  $n$  is the number data points. Normalizing by  $y_{max} - y_{min}$  enables us to compare models with different scales. This is especially useful when comparing the results of different wall velocities.

As shown in Figure 3.8 and Table 3.4, the number of nodes does not affect the solution accuracy. It is possible to get acceptable accuracies even with a low number of nodes. This is because the boundary condition is satisfied exactly at the wall location due to the ghost cell.

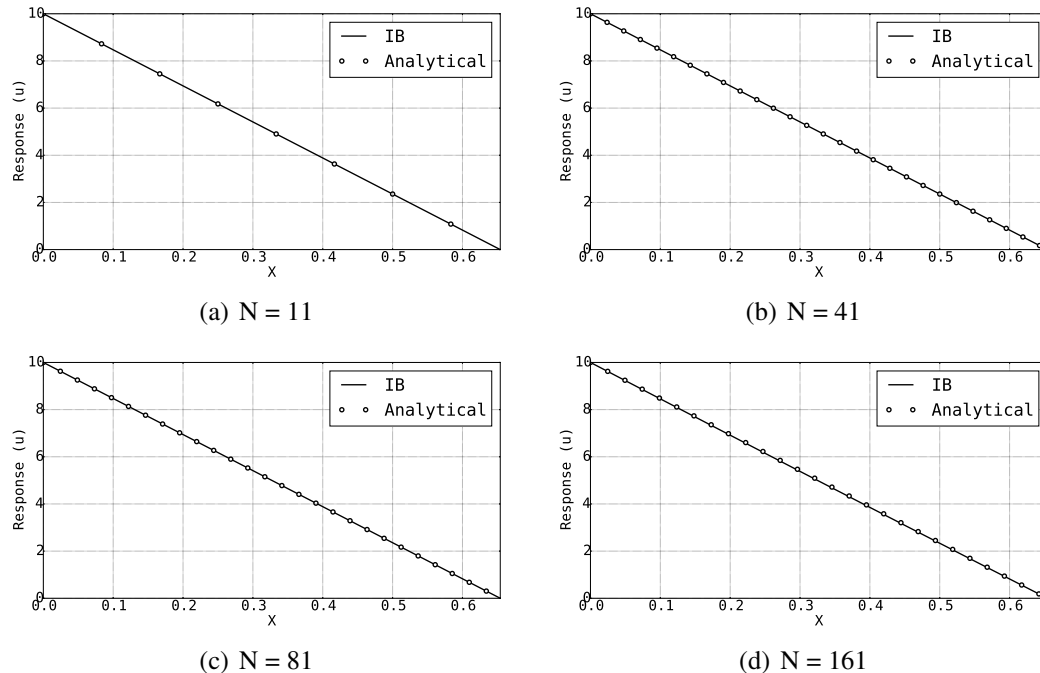


Figure 3.8: Comparison between IB and analytical results for different number of nodes.

Number of nodes	RMSE value
11	$1.49 \times 10^{-15}$
41	$2.08 \times 10^{-15}$
81	$4.19 \times 10^{-10}$
161	$9.94 \times 10^{-10}$

Table 3.4: RMSE value for different number of nodes.

The same problem is solved by fixing the number of nodes at 41 and changing the location of the fixed bar to see its effect on the solution. The wall is located at 0.124, 0.379, 0.723, and 0.936 where none of these locations coincide with the computational nodes. As shown in Figure 3.9 and Table 3.5, the solution accuracy is not affected by wall location as well.

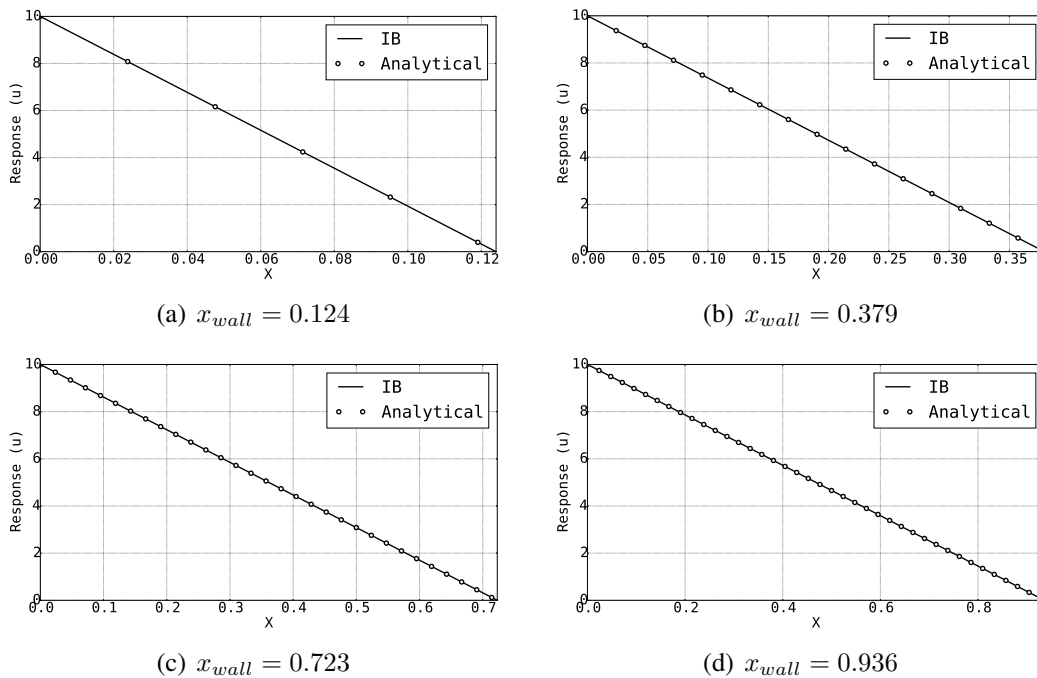


Figure 3.9: Comparison between IB and analytical results for different wall locations.

Wall location	RMSE value
0.124	5.49E-17
0.379	3.16E-15
0.723	2.72E-14
0.936	4.99E-14

Table 3.5: RMSE value for different wall locations.

In the final investigation we looked at the effect of wall velocity of the solution accuracy. For this case, the number of nodes is fixed at 41 and the stationary wall is located at  $x_{wall} = 0.479$ . The moving wall velocity is selected as 100, 1000, 10000, and 100000. As shown in Figure 3.10 and Table 3.6, the wall velocity does not affect the accuracy of the solution.

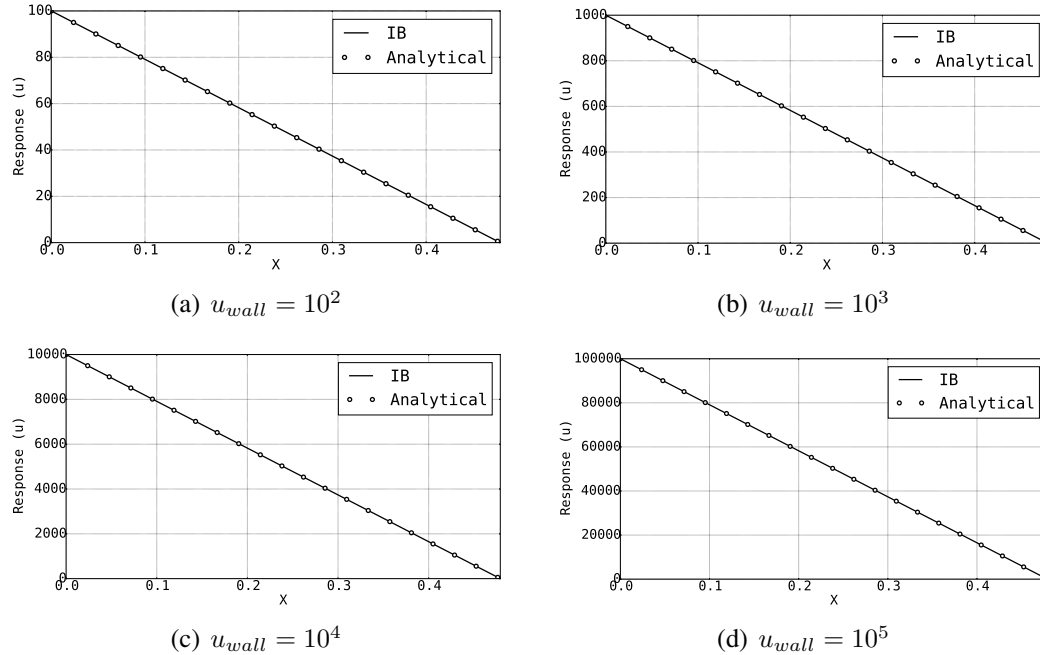


Figure 3.10: Comparison between IB and analytical results for different wall velocities.

Wall velocity	RMSE value
100	$8.89 \times 10^{-15}$
1000	$8.36 \times 10^{-15}$
10000	$8.31 \times 10^{-15}$
100000	$8.62 \times 10^{-15}$

Table 3.6: RMSE value for different wall velocities.

## 3.6 Continuum Forcing Method

In this implementation of the immersed boundary, a forcing equation is added to the continuous governing equation (3.1b) to represent the effect of the boundary. The continuous IB

technique is the original method developed by Peskin [79] for coupled simulation of blood flow due to the contraction of heart muscle. In this approach, the immersed boundary is represented by a set of elastic fibers; their locations are tracked in a Lagrangian fashion by a collection of massless points. These points move with the local fluid velocity. Therefore, the location of the  $k$ -th Lagrangian point,  $X_k$ , is governed by the following equation

$$\frac{\partial X_k}{\partial t} = u(X_k, t) \quad (3.13)$$

Where  $u$  is the velocity of the fluid at location  $X_k$ . The location of fluid nodes,  $x$ , does not necessarily coincide with the location of the Lagrangian points. Thus, it is required to map the velocities from the Eulerian domain, where the fluid's equations of motion are solved, to Lagrangian nodes. In a pure continuum problem, this can be done using the Dirac delta functions. The property of the Dirac delta function that enables the mapping between the Euler and Lagrangian domains is shown in the following equation.

$$\int_{\Omega_f} f(x) \delta(x - X_k) d\Omega = f(X_k) \quad (3.14)$$

As can be seen here, by convolving the function of interest and the delta function, we can evaluate our function of interest at any location where the delta function is defined. Although this is the central idea of mapping data to the Lagrangian domain, this approach becomes unstable in practice [80]. In the practical implementation of immersed boundary method, the effect of the delta function needs to be expanded to a couple of nodes around  $X_k$ . This is achieved by relaxing the delta function. The relaxed delta function is referred to as regularized delta function [81]. The regularized delta function is defined using Equation (3.15) in three dimensions.

$$\delta_h(x_1, x_2, x_3) = \frac{1}{dx_1 \cdot dx_2 \cdot dx_3} \phi\left(\frac{x_1 - \eta_1}{dx_1}\right) \phi\left(\frac{x_2 - \eta_2}{dx_2}\right) \phi\left(\frac{x_3 - \eta_3}{dx_3}\right) \quad (3.15)$$

where  $x_i$  is the spatial coordinate in each direction,  $\eta_i$  is the location where the delta function is defined, and  $dx_i$  is the grid size in each direction. In the above equation  $i$  can be 1, 2, or 3. The  $\phi$  function is defined in Equation (3.16). As shown here, there are different ways of defining this function. The input of  $\phi$  function is  $r$  which is defined as  $(x_i - \eta_i)/dx_i$ .

$$\phi(r) = \begin{cases} 1 - |r| & |r| \leq 1 \\ 0 & \text{otherwise} \end{cases} \quad (3.16a)$$

$$\phi(r) = \begin{cases} \frac{1}{3} (1 + \sqrt{-3r^2 + 1}) & |r| \leq 0.5 \\ \frac{1}{6} (5 - 3|r| - \sqrt{-3(1 - |r|)^2 + 1}) & 0.5 \geq |r| \leq 1.5 \\ 0 & \text{otherwise} \end{cases} \quad (3.16b)$$

$$\phi(r) = \begin{cases} \frac{1}{8} (3 - 2|r| + \sqrt{1 + 4|r| - 4r^2}) & 0 \leq |r| \leq 1 \\ \frac{1}{8} (5 - 2|r| + \sqrt{-7 + 12|r| - 4r^2}) & 1 \leq |r| \leq 2 \\ 0 & \text{otherwise} \end{cases} \quad (3.16c)$$

$$\phi(r) = \begin{cases} \frac{61}{112} - \frac{11}{42}|r| - \frac{11}{56}|r|^2 + \frac{1}{12}|r|^3 + \frac{\sqrt{3}}{336}(243 + 1584|r| - 748|r|^2 - 1560|r|^3 + 500|r|^4 + 336|r|^5 - 112|r|^6)^{1/2} & 0 \leq |r| \leq 1 \\ \frac{21}{16} + \frac{7}{12}|r| - \frac{7}{8}|r|^2 + \frac{1}{6}|r|^3 - \frac{3}{2}\phi(|r| - 1) & 1 \leq |r| \leq 2 \\ \frac{9}{8} - \frac{23}{12}|r| + \frac{3}{4}|r|^2 - \frac{1}{12}|r|^3 + \frac{1}{2}\phi(|r| - 2) & 2 \leq |r| \leq 3 \\ 0 & \text{otherwise} \end{cases} \quad (3.16d)$$

Equation (3.16a) is the 2-point delta function that calculates the linear interpolation between the points [34]. Equation (3.16b) shows the 3-point delta function used by Roma et al. [82] and Equations (3.16c) and (3.16d), used by Peskin [83] are 4-point and 6-point delta functions, respectfully. The comparison between the shape of different  $\phi(r)$  functions

are shown in Figure 3.11.

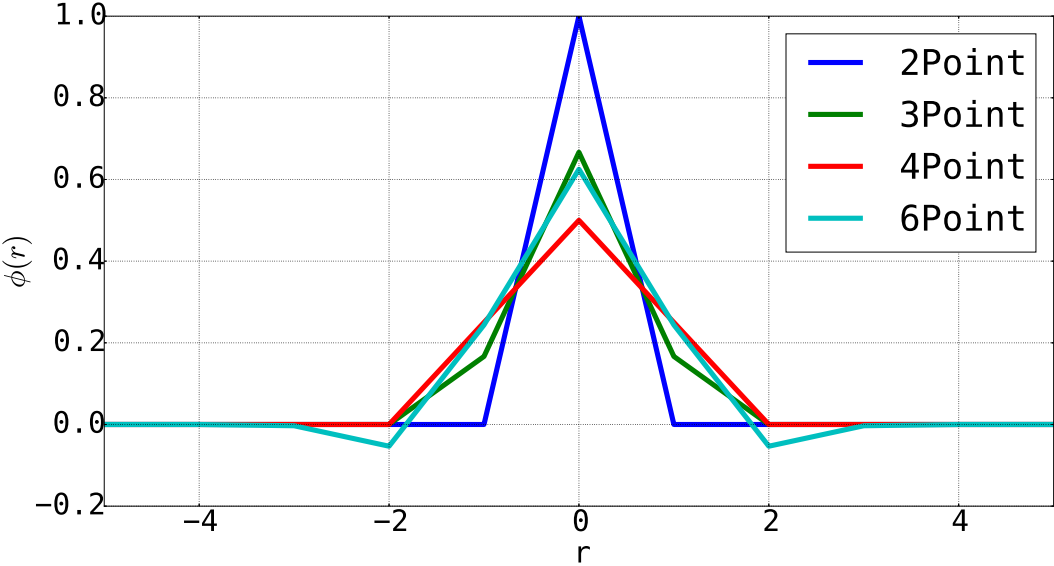


Figure 3.11: Comparison between different formulations of  $\phi$

Now we can write the mapping from the Eulerian nodes of the fluid solver to Lagrangian nodes as shown in Equation (3.17).

$$u(X_k) = \int_{\Omega} u(x) \delta(x - X_k) dx \quad (3.17)$$

Where  $\Omega$  is the computational domain,  $u(x)$  is the velocity at the Eulerian nodes,  $x$  is the Eulerian nodes coordinate,  $u(X_k)$  is the velocity at the desired Lagrangian node, and  $X_k$  is the coordinate of the Lagrangian node. Most continuum forcing approaches are the same up to this point. They differ depending on the way they calculate the forcing terms.

### 3.6.1 Classical IB Method

In the classical IB method, the forces at the immersed boundaries are calculated using appropriate constitutive laws, i.e. Hooke's law. This can be expressed as follows.

$$f(X_k) = \mathcal{M}(X_k) \quad (3.18)$$

Where  $\mathcal{M}$  is an operator that describes the properties of the boundaries. This force is calculated at the Lagrangian points and needs to be transferred back to the Eulerian nodes. This is done using the same delta functions mentioned previously to map the Eulerian results to Lagrangian. This method is well suited for a case of elastic bodies; but, it will fail for the cases of rigid boundaries or when the rigidity of boundaries is much more than the fluid. The origin of this problem is due to the high cycle oscillations that occur near the boundaries.

This approach is applied to the demonstration problem defined in Section 3.3. We modelled the location of the fixed boundary using the classical IB method and verified the results using analytical formulas for this problem. The forcing function is added to the right-hand-side of the governing equation as follows.

$$\frac{\partial u}{\partial t} = \frac{\partial^2 u}{\partial y^2} - f(t) \quad (3.19)$$

Where  $f(t)$  is the forcing function used to model the boundary. This equation is discretized using the Crank-Nicholson method as:

$$u^{n+1} = u^n + \frac{\Delta t}{2} \left( \frac{\partial^2 u^{n+1}}{\partial x^2} + \frac{\partial^2 u^n}{\partial x^2} \right) - \Delta t f^n \quad (3.20)$$

The steps to solve this equation and model the stationary wall using the IB method are as follows:

1. Define the initial condition as  $u^0$  and set  $f^0$  equal to zero
2. Calculate the velocity at the following time step,  $u^1$ , using Equation (3.20)
3. Based on the new velocity at  $n = 1$ , calculate the velocity at the location where the stationary wall is supposed to be,  $X$ , using  $\delta$  function ( $U$ )
4. Calculate the distance that this node will move in the current time step:  $X^{n+1} =$

$$X^n + U\Delta t$$

5. Based on the new location of the node, calculate the forces as:  $F = K(X^{n+1} - X^0)$ , where  $X^0$  is the desired location of the wall and  $K$  is the stiffness of wall.
6. Map the force at the Lagrangian location  $X$  to its neighbouring Eulerian points using  $\delta$  function
7. Reiterate until the convergence is satisfied

For the classical IB method, the accuracy of the results to the number of nodes, wall velocity, and stiffness used to model the wall is investigated. The immersed boundary simulation is compared with the analytical solution of this problem. I chose the normalized root mean square error to compare the analytical and IB results.

For the first investigation, I selected the wall stiffness as  $10^2$  and its location selected as  $x_{wall} = 0.51885$ . We chose this location so that it does not coincide with the location of computational nodes. The time step is chosen as  $10^{-5}$  and the wall velocity is fixed at  $1m/s$ . For this simulation, we used both 2-point and 4-point delta functions to transfer results between Lagrangian and Eulerian nodes. The computation domain is discretized using 11, 41, 81, and 161 nodes. The results of IB method is verified with analytical results.

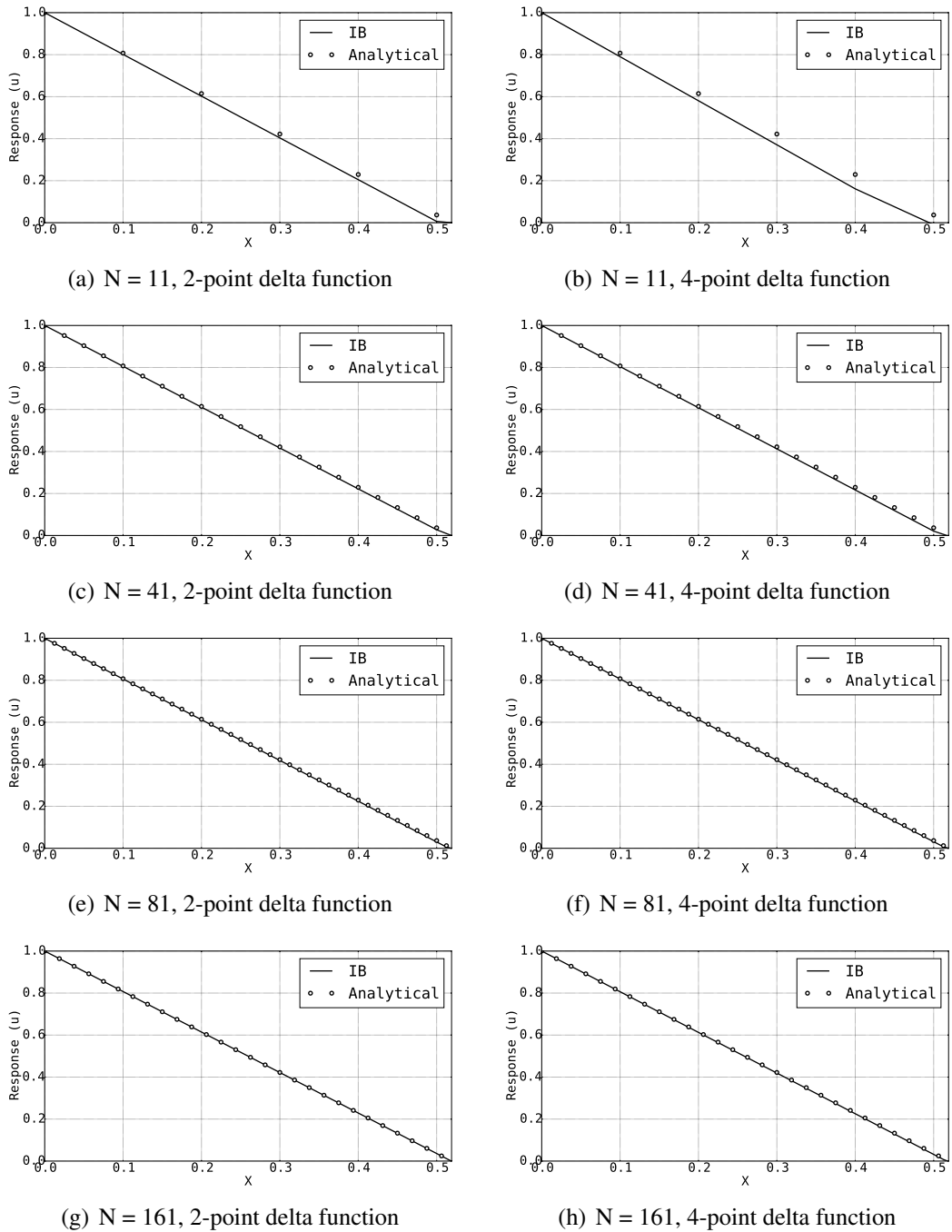


Figure 3.12: Comparison between IB and analytical results for different number of nodes and delta functions for Couette flow problem.

Number of nodes	RMSE value	
	2-point delta function	4-point delta function
11	0.0105	0.0292
41	0.0035	0.002
81	0.0026	0.0022
161	0.00023	0.0002

Table 3.7: RMSE values for different number of nodes and delta functions.

As shown in Figure 3.12 and Table 3.7, by increasing the number of nodes, the error in IB result decreases. However, changing the delta function from 2-point to 4-point does not significantly affect the accuracy of the solution. The higher order delta function can also reduce the accuracy of the solution for a very low number of nodes (here 11).

For the second investigation we looked at the effect of changing the moving wall velocity on the solution accuracy. For this simulation we fixed the number of nodes to 81, set the stiffness value to  $10^2$ , the wall location at 0.51885, and the time step as  $10^{-5}$ . For this problem we only focused on 2-point delta function. We chose the wall velocity as  $10m/s$ ,  $10^2m/s$ ,  $10^3m/s$ , and  $10^4m/s$ . As shown in Figure 3.13 and Table 3.8, the method is capable of handling flow with different velocities without a loss in accuracy of the results. However, the simulation time grows with increases in wall velocity.

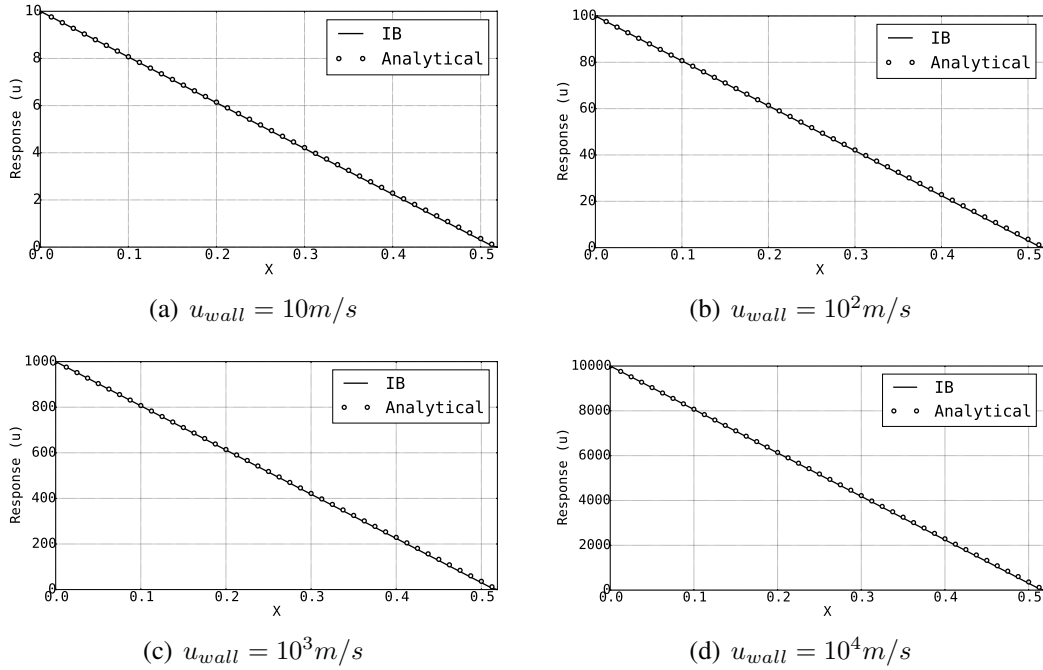


Figure 3.13: Comparison between IB and analytical results for different wall velocities.

Wall velocity (m/s)	RMSE
10	0.0024
$10^2$	0.0024
$10^3$	0.0024
$10^4$	0.0024

Table 3.8: RMSE values for different wall velocities.

For the last case study of classical IB method, we looked at the effect of the wall stiffness on the accuracy of the solution. For this case, we fixed the wall location at  $x_{wall} = 0.51885$  and defined the wall velocity as  $10\text{ m/s}$ . The time step is selected as  $10^{-5}\text{ s}$ . We looked at the wall stiffness of  $0.1\text{ N/m}$ ,  $1\text{ N/m}$ ,  $10\text{ N/m}$ , and  $100\text{ N/m}$ . As shown in Figure 3.14 and Table 3.9, wall stiffness has a considerable effect of the solution result. Therefore, a convergence study for the wall stiffness value is usually required if one wants to model the stiff boundaries.

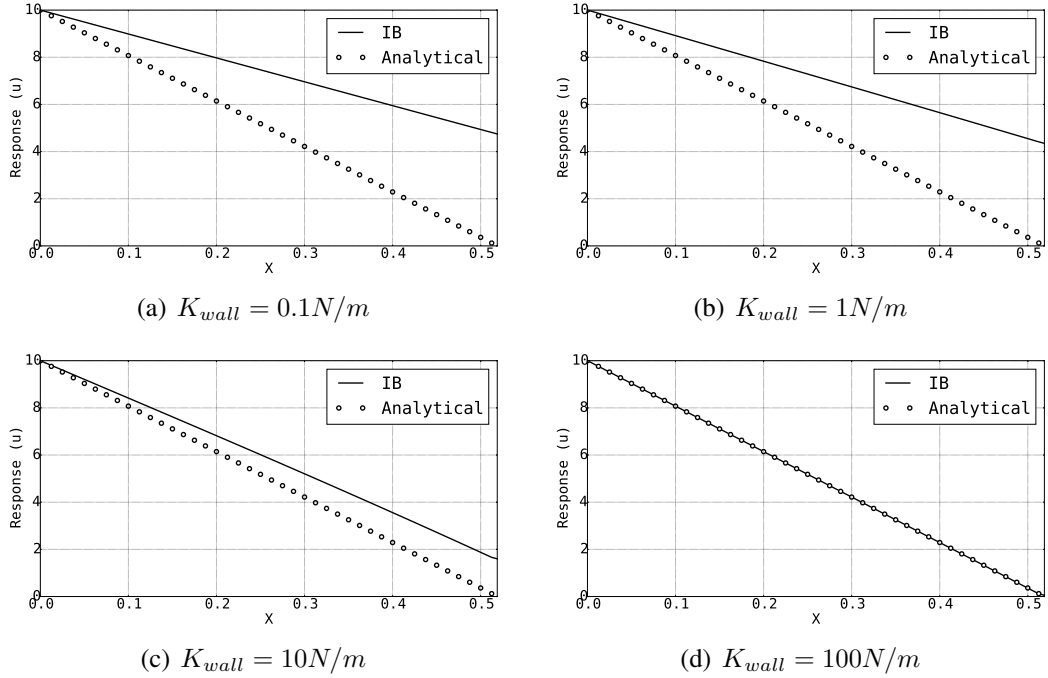


Figure 3.14: Comparison between IB and analytical results for different wall stiffness values.

Wall stiffness (N/m)	RMSE
0.1	0.1912
1	0.1759
10	0.0665
100	0.001

Table 3.9: RMSE values for different wall stiffness values.

### 3.6.2 Virtual Boundary Method

The virtual boundary method is a different approach to imposing the effect of immersed boundary through force terms. This method is well suited for both the rigid and elastic boundaries. The difference between this approach and the classical IB method is that it does not require the solution of the constitutive equations to calculate the force terms. This method is based on the work of Goldstein et al. [42] to simulate the flow around the rigid

bodies. The forcing term in the virtual boundary method is defined as

$$F(X_k, t) = \alpha \int_0^t [u(X_k, t) - U(X_k, t)] dt + \beta [u(X_k, t) - U(X_k, t)] \quad (3.21)$$

where  $F$  is the required force at the  $k$ -th Lagrangian point,  $u(X_k, t)$  is the velocity calculated from the Eulerian nodes using the  $\delta$  function, and  $U(X_k)$  is the desired velocity at the Lagrangian point  $X_k$ . The coefficient  $\alpha$  and  $\beta$  are selected to best enforce the boundary condition at the immersed solid boundary, this is done by doing convergence studies on these values. Equation (3.21) is essentially a way to provide feedback control to the system to make sure that the desired velocity ( $U(X_k, t)$ ) is achieved at the immersed boundary. From a physical standpoint, this equation represents a damped oscillator [51].

As before, we apply this technique to the demonstration problem defined in Section 3.3. We use the Crank-Nicholson method to discretize the equations as shown in the following equation:

$$\frac{u^{n+1} - u^n}{\Delta t} = \frac{1}{2} \left( \frac{\partial^2 u^{n+1}}{\partial x^2} + \frac{\partial^2 u^n}{\partial x^2} \right) \quad (3.22)$$

Where  $n$  is the current time step. The steps to solve this problem using the virtual boundary method can be defined as follows

1. Define the initial condition as  $u^0$  and set  $f^0$  equal to zero
2. Calculate the velocity at the next time step,  $u^1$ , using Equation (3.20)
3. Map the velocity results to the Lagrangian nodes using the  $\delta$  function
4. Based on the new velocity at  $n = 1$  evaluate Equation (3.21)
5. Map the force at the Lagrangian location  $X$  to its neighbouring Eulerian points using  $\delta$  function
6. Reiterate until the convergence is satisfied

Comparing the virtual boundary method to the classical IB method, we can see that fewer steps are required for this formulation. Moreover, there is no need to solve the constitutive equation for the solid domain that reduces the total computational cost.

Like the classical IB method, we investigate the effect of mesh size, moving wall velocity, and values for  $\alpha$  and  $\beta$  constants of the solution accuracy. The numerical results are verified with the analytical solution of this problem. We use the RMSE value as a metric to compare the results.

We looked at the effect of mesh size on the solution accuracy of the virtual boundary method. For this case, the moving wall velocity is fixed at  $10m/s$  with the location of the fixed wall at  $x_{wall} = 0.726$ . The time step for this simulation is chosen as  $10^{-5}$  with  $\alpha = -1000$  and  $\beta = -10$ . We chose the number of nodes as 11, 41, 81, and 161. The total length of the domain is selected as  $1m$ . As shown in Figure 3.15 and Table 3.10, by increasing the number of nodes, the simulation results become more accurate. However, the convergence is reached using less number of nodes compared to the classical IB method of the last section. This means that the computational effort to get the same accuracy compared to classical IB method is much less when using the virtual boundary method due to less number of computational nodes.

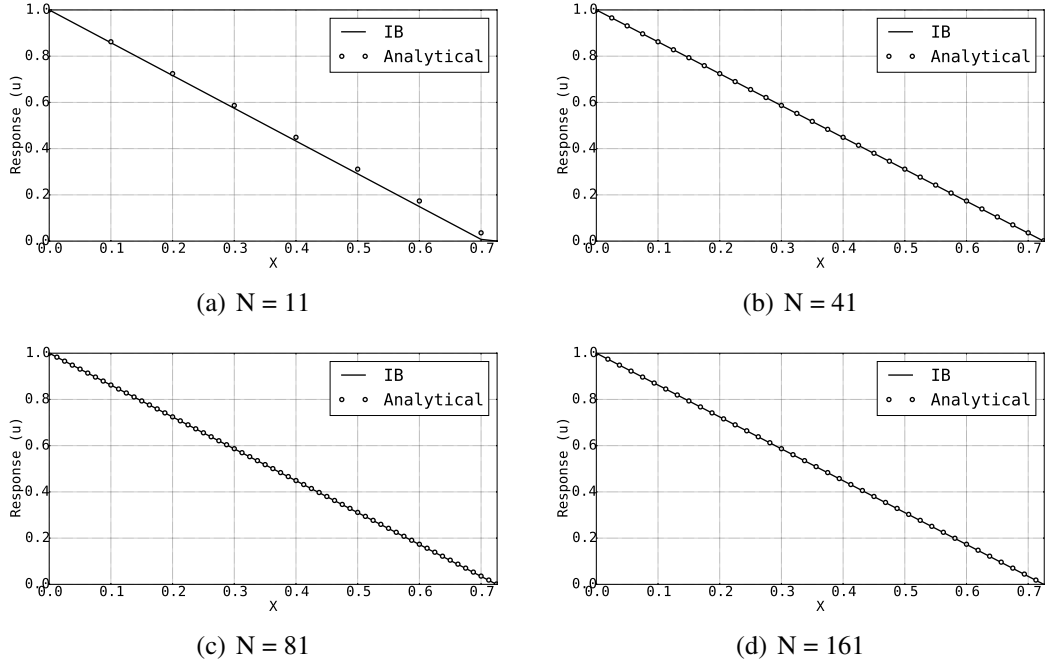


Figure 3.15: Comparison between IB and analytical results for different number of nodes.

Number of nodes	RMSE
11	0.012
41	0.00065
81	0.00063
161	0.00058

Table 3.10: RMSE values for different number of nodes.

We looked at the effect of wall velocity on the solution accuracy. As before, the length of the domain is fixed at  $1m$  with the wall defined at  $x_{wall} = 0.726$  and the time step is chosen as  $10^{-5}$ . We chose the  $\alpha$  and  $\beta$  constants as  $-1000$  and  $-10$ , respectively. We simulated the flow selecting the wall velocity as  $10m/s$ ,  $100m/s$ ,  $1000m/s$ , and  $10000m/s$ . The results are compared with the analytical results. As shown in Figure 3.16 and Table 3.11, the wall velocity does not affect the accuracy of the solution. When compared with the results of the classical IB method in the previous section, we can see that the virtual boundary method produces more accurate results. Moreover, the simulation time is much less than the classical IB method.

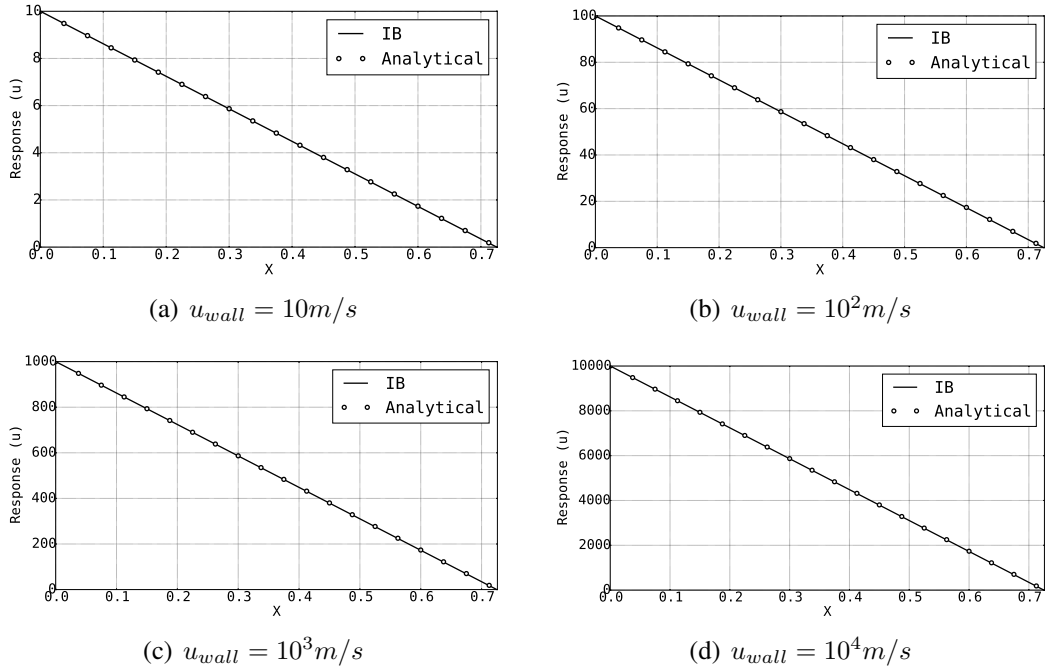


Figure 3.16: Comparison between IB and analytical results for different wall velocities.

Wall velocity (m/s)	RMSE
10	0.000616
$10^2$	0.000616
$10^3$	0.000616
$10^4$	0.000616

Table 3.11: RMSE values for different wall velocities.

Finally, we looked at the effect of constants  $\alpha$  and  $\beta$  on the accuracy of the solution. We discretized the domain using 81 nodes with wall velocity equal to  $100m/s$  and time step equal to  $10^{-5}$ . The location of the fixed wall is chosen as  $x_{wall} = 0.726$ . The flow between the plates is modelled using different coefficients for  $\alpha$  and  $\beta$  as shown in Table 3.12.

As can be seen in Figure 3.17 and Table 3.12,  $\alpha$  value has a considerable effect on the accuracy of the results. Increasing the  $\alpha$  value with an order of magnitude results in a considerable improvement in the accuracy of the solution. However,  $\beta$  value does not contribute to the accuracy but improves the convergence of the solution. The solutions

with larger  $\beta$  values converged in less number of iterations.

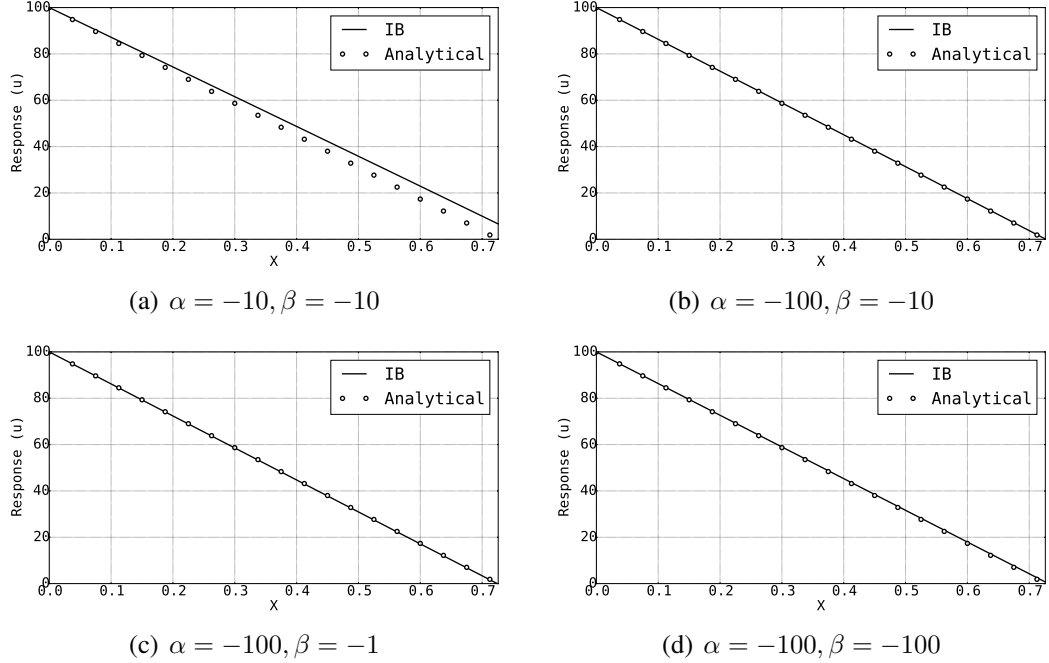


Figure 3.17: Comparison between IB and analytical results for different values for constants  $\alpha$  and  $\beta$ .

Case number	$\alpha$	$\beta$	RMSE
1	-10	-10	0.0327
2	-100	-10	0.00138
3	-100	-1	0.00129
4	-100	-100	0.00346

Table 3.12: Different values used for investigating the effect of  $\alpha$  and  $\beta$ .

### 3.6.3 Penalization Method

The third class of continuum immersed boundary techniques are known as penalization method first introduced by Arquis and Caltagirone [44]. In this method, the solid boundaries are modeled as porous media. Porosity, or void fraction, is a measure of the void spaces in a material and varies between 0 and 1. For the solid domain, the porosity value is near zero whereas its value is close to one in the fluid domain. Flow through a porous

domain is described using the Darcy's law. This is a simple proportional relationship between the instantaneous discharge rate through a porous medium, the viscosity of the fluid, and the pressure drop.

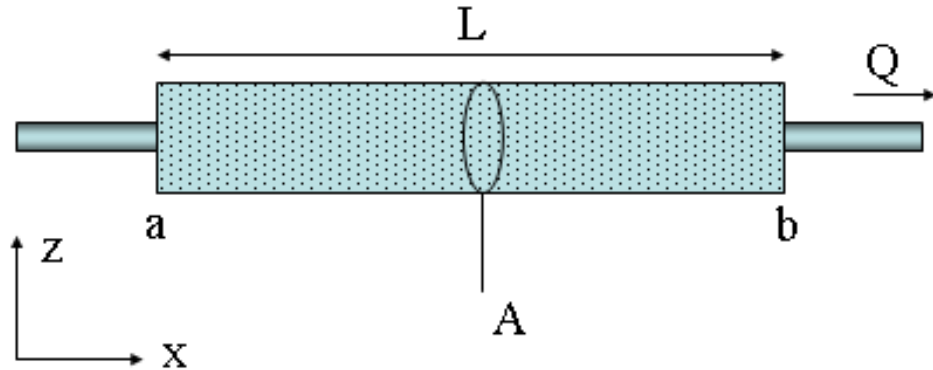


Figure 3.18: Flow through a porous pipe.

For flow through a porous domain in a pipe shown in Figure 3.18, Darcy's law is written as

$$Q = \frac{\kappa A \Delta p}{\mu L} \quad (3.23)$$

where  $Q$  is the total flow discharge,  $\kappa$  is the permeability of the domain,  $\Delta p$  is the pressure drop due to the porosity between two ends of the pipe,  $\mu$  is the fluid's viscosity, and  $L$  is the length of the domain. Darcy's law can be considered as a relation between the flow velocity and pressure drop. This pressure drop is used in the penalization method to represent the solid boundaries by modelling the force term using Equation (3.23). The force term is defined as follows:

$$f = -\mathcal{H}(\mathcal{X}) \frac{\mu}{\kappa} v \quad (3.24)$$

Where  $v$  is the velocity of the flow. To apply the force term to only the region inside the solid boundary, the penalization force is multiplied by a Heaviside function,  $\mathcal{H}(\mathcal{X})$ , that is a function of the relative distance of the points in the domain to the boundary of

the solid region. The Heaviside function  $\mathcal{H}$  has the value of *one* for all points inside the solid boundary and is *zero* for points outside the boundary. This will give us a zero forcing term for points outside the solid boundary and non-zero for points inside. Therefore, the pressure drop is only applied to the points inside the solid domain. This is explained in more detail in the following example.

Assume that the solid boundary is a circle located at  $(1, 2)$  with a radius of 2. This curve is defined using Equation (3.25).

$$(x - 1)^2 + (y - 2)^2 = 4 \quad (3.25)$$

The relative location of an arbitrary point  $x_0 = (\eta, \rho)$  to this boundary is determined using the following equation,

$$\mathcal{X}(\eta, \rho) = 4 - (\eta - 1)^2 - (\rho - 2)^2 \quad (3.26)$$

Depending on the sign of  $\mathcal{X}$ , we can make the following conclusions:

$$\begin{cases} \mathcal{X} > 0 & x_0 \text{ is inside the solid boundary} \\ \mathcal{X} < 0 & x_0 \text{ is outside the solid boundary} \\ \mathcal{X} = 0 & x_0 \text{ is on the boundary} \end{cases} \quad (3.27)$$

The sign of  $\mathcal{X}$  divides the physical domain into three regions. To use this function for force term assignment to mesh cell, we need to convert its values to 0 and 1. The force terms outside the solid boundaries are multiplied by zero whereas the force terms inside the solid boundary are multiplied by one. This is done by feeding the values of function  $\mathcal{X}(x)$  to a Heaviside function,  $\mathcal{H}$ . The Heaviside function, or the unit step function, is a discontinuous function whose value is zero for negative and one for positive values of  $x$  as

shown in Figure 3.19.

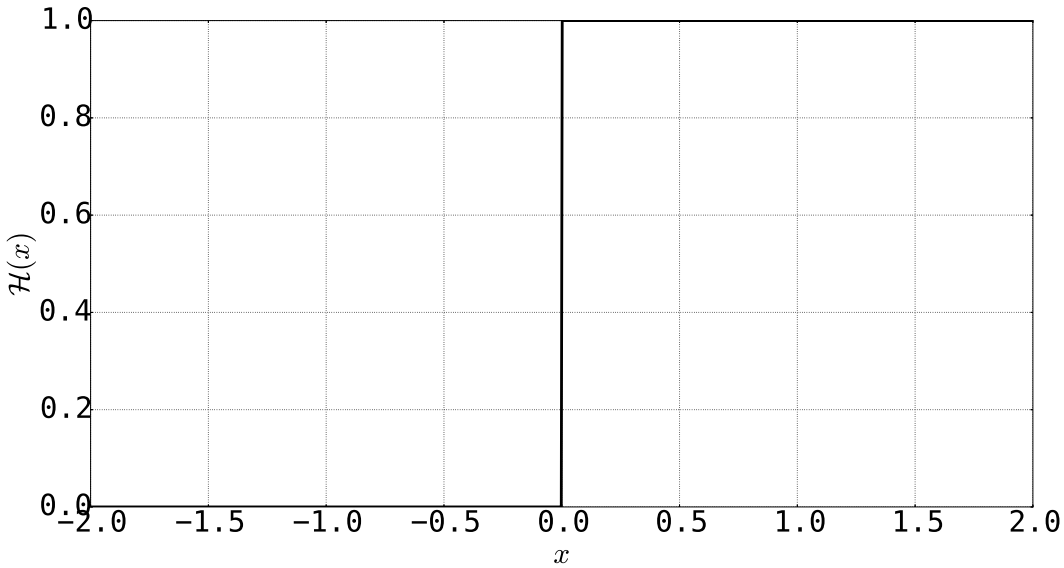


Figure 3.19: The Heaviside function.

By Heaviside function acting on  $\mathcal{X}$ , we get the value of one for nodes inside the solid boundary and zero for outside nodes. These are then multiplied to the force terms calculated using Equation (3.24). This enables us to apply the force term only within the solid domain. This method is applied to the demonstration problem of Section 3.3. For this problem, we looked at the effect of the number of mesh cells, wall velocity, and the permeability value on the accuracy of the method. The results are compared with analytical results for this problem like the previous sections.

For the first set of results, we looked at the effect of mesh size on the accuracy of the solution. The domain length is chosen as  $1.0m$  where the position of the fixed wall is selected as  $0.6125$ . We chose this so that the computational nodes won't coincide with the wall location. This better represents the application of the IB method. We chose the number of nodes as 11, 41, 81, and 161. As shown in Figure 3.20, as we increase the number of nodes, the total error between the numerical and analytical results decreases. For the Case where there is a computational node exactly on top of the location for the stationary wall ( $n = 161$ ), the two results match perfectly. The IB results are shown using

the solid line and the analytical results are represented using white circles.

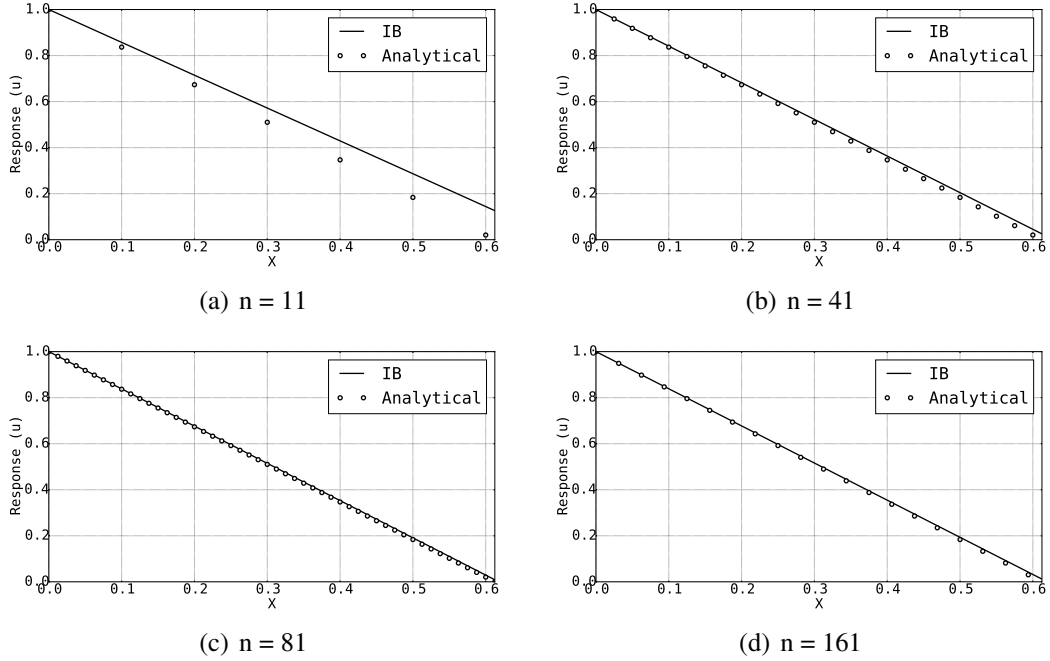


Figure 3.20: Comparison between IB and analytical results for different number of nodes.

The RSME value was used to compare the IB to the analytical results as shown in Table 3.13.

Number of nodes	RMSE value
11	0.0624
41	0.0139
81	0.005
161	0.001

Table 3.13: RMSE values for different number of nodes.

As can be seen in Table 3.13, even for  $n = 161$ , the RMSE value is not zero. This is because in the penalization method, even for low values of porosity, there is still a small flow going through the solid domain.

For the subsequent investigation, we look at the effect of the different velocity of the moving wall on the accuracy of the penalization method. For this analysis, we defined the fixed wall at  $x = 0.4325$  and discretized the domain using 81 nodes. The inlet velocity

is selected as 1, 10, 100, and 1000. To verify the methodology, we compared the IB with analytical results. We chose the time step as  $10^{-5}$  and the porosity value as  $\kappa = 10^{-5}$ . As shown in Figure 3.21 and the RMSE values in Table 3.14, the inlet velocity does not affect the accuracy of the response. Moreover, all of these simulations are done using the same time step and porosity value.

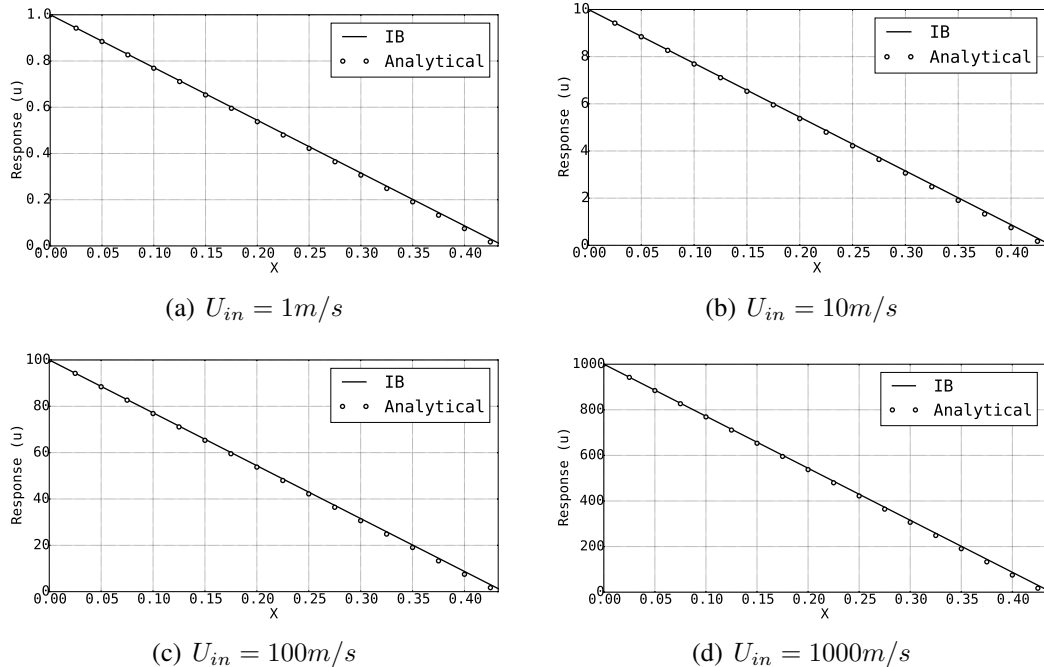


Figure 3.21: Comparison between IB and analytical results for different inlet velocities.

Inlet velocity (m/s)	RMSE value
1	0.0056
10	0.0056
100	0.0056
1000	0.0056

Table 3.14: RMSE values for different inlet velocities.

Finally, we looked at the effect of porosity values on the accuracy of the simulation. For this purpose, we fixed the wall location at  $x_{wall} = 0.435$  and defined the velocity of the moving wall as  $10m/s$ . The length of the domain is selected as  $1m$  and discretized using 81 nodes. We chose the time step as  $10^{-5}$ . We investigated the accuracy of penalization

method to porosity values of  $10^{-2}$ ,  $10^{-3}$ ,  $10^{-4}$ ,  $10^{-5}$  by comparing the IB simulation with analytical results. The results shown in Figure 3.22 and Table 3.15 displays the strong dependency of the simulation results of the porosity,  $\kappa$ , value. Several simulations need to be run and the convergence needs to be studied to select an appropriate porosity.

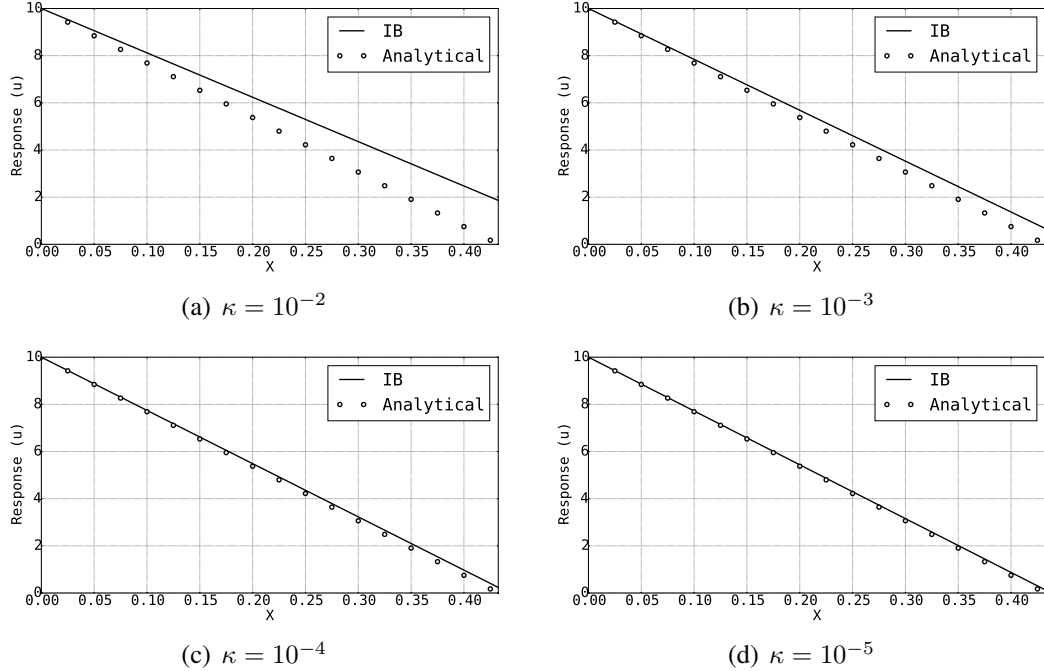


Figure 3.22: Comparison between IB and analytical results for different porosity values.

Porosity (m/s)	RMSE value
$10^{-2}$	0.079
$10^{-3}$	0.028
$10^{-4}$	0.01
$10^{-5}$	0.0056

Table 3.15: RMSE values for different porosity values.

The penalization method is probably the easiest one of the continuous IB methods to implement; however, its accuracy is very dependent on the number of nodes used. This is because there are no mechanisms to define the exact location of solid boundaries in the penalization method. This can lead to loss of accuracy and oscillations near the boundaries. The porosity value,  $\kappa$ , needs to be selected by running multiple simulations and compare

the results for convergence. Although, even with low values of porosities, there is a leakage in the solid domain that reduces the accuracy of the simulations.

## 3.7 Application in Continuum Sensitivity Analysis

While considerable effort of research and development went in different techniques for modelling the flow using immersed boundary method, very few efforts were directed toward calculating the sensitivity of flow with respect to change in the shape of the immersed boundary.

As mentioned in the previous chapter, there are different approaches for calculating the sensitivity response of a system. Among these methods, the discrete and continuum analytical sensitivity calculation techniques are more desirable due to their accuracy and cost compared to the numerical method. However, the continuum sensitivity analysis method enables a single black-box solver for the solution of both governing equation and sensitivity response. Due to this superiority, continuum sensitivity analysis is chosen as the sensitivity analysis technique. As the results indicate, immersed boundary method of choice needs to conform to the requirements of the sensitivity analysis. As mentioned in the previous chapter, continuum sensitivity equations are derived by differentiating the continuous governing equations. Only the IB methods with continuum forcing approaches have the boundary formulation in their continuous formulation. Therefore, continuous IB is used. The discrete immersed boundary method can also be utilized if discrete sensitivity analysis is chosen. However, we do not investigate those techniques in this work. This is investigated in the works of [84, 56, 57], where they used the penalization technique alongside discrete sensitivity analysis method to calculate the sensitivity of flow to boundary shape changes. These works are focused mainly on Stokes flow where the Reynolds number is relatively small.

The continuum sensitivity analysis requires the governing equations be continuously differentiable. However, the delta functions used in classical IB and virtual boundary

method do not satisfy this condition. The Heaviside function employed in the penalization technique also does not satisfy this condition, since a discrete step function is used as the Heaviside function to assign the force terms. This discontinuity needs to be addressed when using the CSA to calculate the sensitivities. This is achieved by introducing new regularized delta function and using regularized Heaviside functions to assign force terms to computational nodes. This is investigated in more detail in the next Chapter.

## 3.8 Summary

In this chapter, we investigated different immersed boundary techniques in detail and compared them concerning accuracy and ease of implementation. The discrete immersed boundary techniques are more general and do not require user defined parameters to represent the immersed boundaries. However, they cannot be implemented without a thorough knowledge of discretization technique used for the governing equations. Moreover, the implementation of interpolation function used for force calculation discrete IB can become extremely complicated for complex 3D boundaries. On the other hand, the continuous forcing immersed boundary technique is straightforward and can be easily implemented without a deep understanding of discretization and solution procedure, since the immersed boundary is handled in the continuum form of the equations. Using the continuous forcing immersed boundary technique, it is possible to reach the same accuracy as the discrete method with the aid of tuning parameters. Most importantly, the continuum sensitivity analysis can be used in conjunction with continuous forcing immersed boundary method. This enables us to use the same solver for solving both the governing equations and the sensitivity analysis. Therefore, the continuum immersed boundary is used to derive the sensitivity response of coupled aero-structural system. The current bottleneck in doing the sensitivity analysis using continuum immersed boundary method is the discontinuous mapping functions that are used to assign the forcing terms to mesh cells. This needs to be done

in a continuum fashion so that continuum sensitivity analysis can be used.

# **Chapter 4**

## **Shape Sensitivity Analysis Using Immersed Boundary Method**

In this chapter we apply the continuum sensitivity analysis to the CFD simulations conducted using the Immersed Boundary (IB) method, focusing on calculating the sensitivity of flow descriptors, such as pressure and velocity, with respect to the design variables that control the shape of the boundary, i.e. radius of a cylinder, or airfoil camber. The solid domain boundary is represented by using an analytical function. However, as will be shown in the following chapters, this is not required for applying this method. In this chapter, the modifications of the IB approach for making it suitable for continuum sensitivity formulation are discussed. To the best of the author's knowledge, this is the first time that continuum sensitivity analysis has been done for CFD simulations based on the continuum IB formulation.

In contrast to traditional body conformal methods, in the IB approach, the solid boundaries are represented by modifying the governing equation near the boundaries. In the case of continuum IB method, this is done by adding the appropriate force term to the cells adjacent to the immersed boundary. The value of these forces are calculated by using either

a feedback forcing [42] or a penalization function [44]. The Navier-Stokes (NS) equations are written as:

$$\frac{\partial \mathbf{u}}{\partial t} + \mathbf{u} \cdot \nabla \mathbf{u} = -\frac{\nabla P}{\rho} + \mu \nabla^2 \mathbf{u} + \mathbf{f} \quad (4.1)$$

Where  $\mathbf{u}$  is the velocity vector,  $P$  is pressure,  $\mu$  is kinematic viscosity ( $\mu/\rho$ ),  $\rho$  is density, and  $\mathbf{f}$  is the forcing term. The NS equations are solved on a Eulerian grid that is fixed in space and the IB is defined on a separate movable Lagrangian grid. This is shown Figure 4.1.

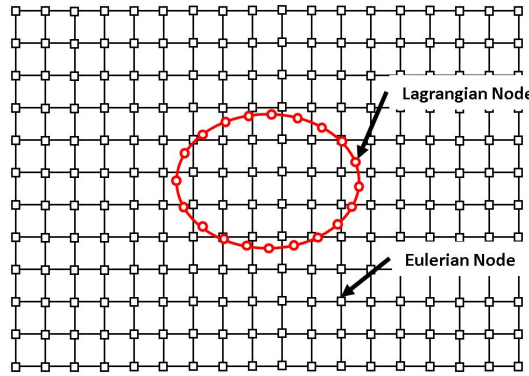


Figure 4.1: Eulerian and Lagrangian nodes for representing the fluid and solid domains. The Eulerian and Lagrangian nodes are represented by squares and circles, respectively.

The forcing function in the penalization method is calculated at the *Eulerian* nodes and is applied to computational nodes inside the solid boundary using a step function as shown in Equation (4.2).

$$\mathbf{f} = -\mathcal{S}(\mathcal{X}(b))\kappa \mathbf{u} \quad (4.2)$$

Where  $\mathcal{S}$  is the step function,  $\mathcal{X}$  defines the relative location of the computational nodes inside the domain to the IB boundary,  $\kappa$  is the penalization parameter, and  $\mathbf{u}$  is the fluid velocity. Using this forcing function, the governing equation (4.1) is rewritten as shown in Equation (4.3).

$$\frac{\partial \mathbf{u}}{\partial t} + \mathbf{u} \cdot \nabla \mathbf{u} = -\frac{\nabla P}{\rho} + \mu \nabla^2 \mathbf{u} - \mathcal{S}(\mathcal{X}(b))\kappa \mathbf{u} \quad (4.3)$$

As mentioned in Chapter 2, to derive the continuum sensitivity formulation, the governing

equation of (4.3) is differentiated with respect to the design variable,  $b$ . The step function  $\mathcal{S}$ 's derivative is the Dirac delta function, which is singular and cannot be used to solve the governing equations in a numerical framework. Therefore, a regularized Heaviside function,  $\mathcal{H}$ , will be employed instead of the step function for penalizing the governing equation. The effect of this function on the simulation results and sensitivity formulation will be discussed in the following sections.

In the virtual boundary method, the forcing function is calculated at the *Lagrangian* nodes.

$$\mathbf{f}(\mathbf{X}, t) = \alpha \int_0^t [\mathbf{u}(\mathbf{X}, \tau) - \mathbf{V}(\mathbf{X}, \tau)] d\tau + \beta [\mathbf{u}(\mathbf{X}, t) - \mathbf{V}(\mathbf{X}, t)] \quad (4.4)$$

Where  $\mathbf{u}(\mathbf{X}, t)$  is the fluid's velocity at the Lagrangian points  $\mathbf{X}$  and  $\mathbf{V}(\mathbf{X}, t)$  is the desired velocity at the Lagrangian point. For the no-slip boundary condition at the solid boundary, the desired velocity  $\mathbf{V}(\mathbf{X}, t)$  is zero at each of the Lagrangian points. The Eulerian nodes, where the fluid's governing equation is solved, does not necessarily coincide with the Lagrangian points. Moreover, the forcing functions that are evaluated at the Lagrangian nodes need to be mapped to the Eulerian nodes where the governing equations for the fluid are solved. As mentioned in Chapter 3, different mapping functions are used for transferring data between the Lagrangian and Eulerian nodes. However, none of these functions are continuously differentiable as required for the continuum sensitivity analysis. To address this issue, a regularized delta function is introduced.

## 4.1 Regularized Heaviside/Delta Function

The Regularized Heaviside (RH) function is a step function that is smoothed so that its derivative can be calculated numerically. The RH function is also known as sigmoid function in mathematics and is characterized as real-valued and differentiable, having either a non-negative or non-positive first derivative. There are a pair of horizontal asymptotes as

$x \rightarrow \pm\infty$ . The RH function is used instead of the step function to penalize the governing equation. Several different RH functions defined in Equation (4.5) are shown in Figure 4.2.

$$\mathcal{H}_1 = \frac{1}{2} + \frac{1}{\pi} \arctan(x) \quad (4.5a)$$

$$\mathcal{H}_2 = \frac{1}{1 + e^{-x}} \quad (4.5b)$$

$$\mathcal{H}_3 = e^{-e^{-x}} \quad (4.5c)$$

$$\mathcal{H}_4 = \frac{1 + \tanh(x)}{2} \quad (4.5d)$$

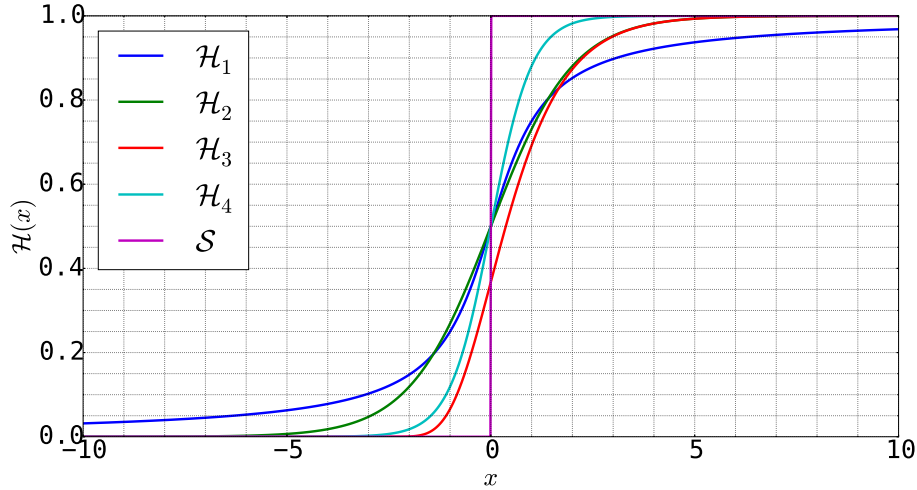


Figure 4.2: Comparison of different regularized Heaviside functions ( $\mathcal{H}_i$ ) and step function ( $\mathcal{S}$ ).

As shown in Figure 4.2, all RH functions, other than  $\mathcal{H}_3$ , are symmetric around  $x = 0$ . This symmetry is required since the line  $x = 0$  defines the boundary of the solid domain and accurate representation of the boundary requires the force terms to have same amount of information from both side of the boundary. By using an asymmetric definition for the RH function, the force term will be biased only on information from one side of the boundary. In this work, the RH function selected is  $\mathcal{H}_4 = \frac{1 + \tanh(x)}{2}$ , since it gives the fastest transition from 0 to 1. This transition is further controlled by adding the control

parameter  $\eta$  to the RH function definition as shown in Equation (4.6). The effect of the control parameter on the RH function is shown in Figure 4.3. As shown in Figure 4.3, the transition region is reduced by increasing the control parameter. Using this feature, the smearing effect of penalization method can be reduced near the boundaries.

$$\mathcal{H} = \frac{1 + \tanh(x/\eta)}{2} \quad (4.6)$$

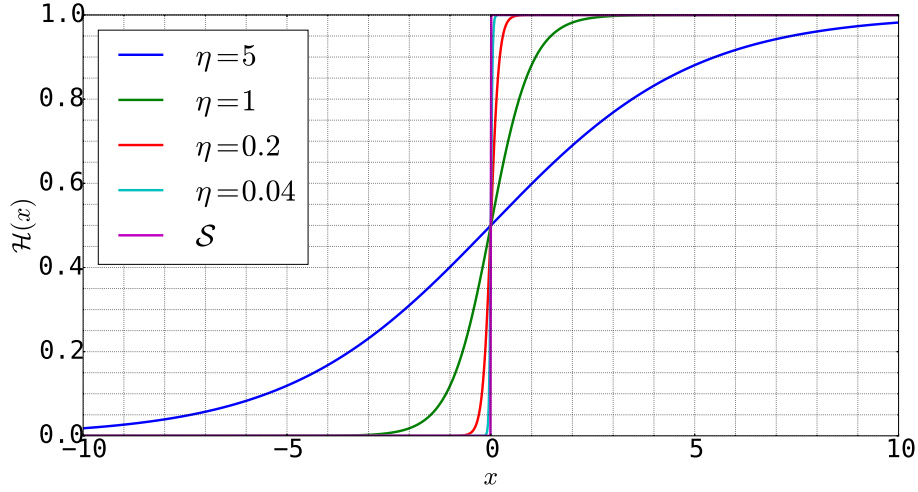


Figure 4.3: Effect of control parameter  $\eta$  on the RH function.

The penalized NS equation using the RH function of Equation (4.2) is continuous and can be differentiated to derive the continuum sensitivity equations. The free parameter is defined based on the desired change of the RH function within a particular range as shown in Equation (4.7).

$$\eta = \frac{R}{2 \tanh^{-1}(p)} \quad (4.7)$$

Where  $R$  is the distance that the  $p$  percentage of the RH function occurs. For example, if it is required for the RH function to change 99 percent ( $p = 0.99$ ) within length of 0.01 ( $R = 0.01$ ), the required  $\eta$  is calculated as 0.0018 using Equation (4.7).

For IB simulations incorporating the virtual boundary method, the Regularized Delta (RD) function is a substitute used for transferring data between the Lagrangian and Eulerian

nodes. In mathematics, the Dirac delta function is defined as the derivative of the unit step function. To be consistent with the mathematical formulation, the RD function is calculated by differentiating the RH functions of Equation (4.5) as shown in Equation (4.8). These RD functions are plotted in Figure 4.4.

$$\mathcal{D}_1 = \frac{1}{\pi(x^2 + 1)} \quad (4.8a)$$

$$\mathcal{D}_2 = \frac{e^{-x}}{(1 + e^{-x})^2} \quad (4.8b)$$

$$\mathcal{D}_3 = \frac{e^{-x}}{e^{e^{-x}}} \quad (4.8c)$$

$$\mathcal{D}_4 = -\frac{\tanh^2(x) + 1}{2} \quad (4.8d)$$

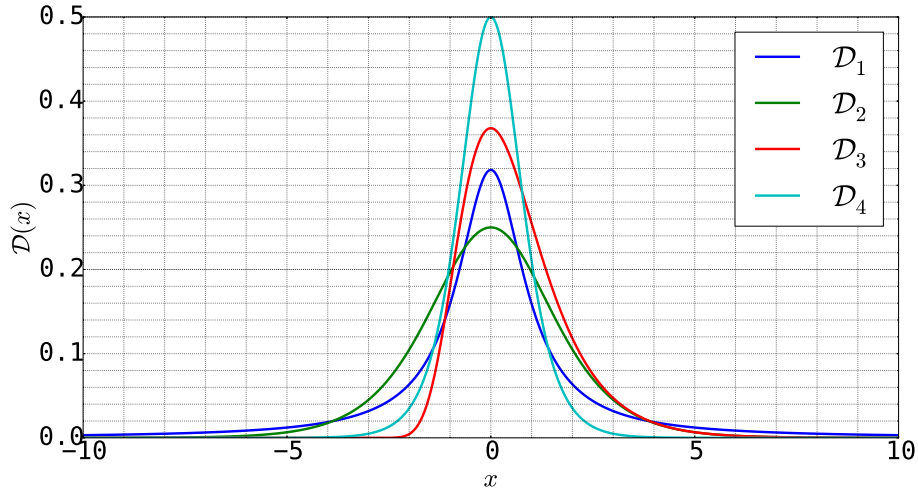


Figure 4.4: Comparison between different regularized delta functions ( $\mathcal{D}_i$ ). The integral of all these functions over  $x \in (-\infty, \infty)$  is equal to one.

RD functions  $\mathcal{D}_2$  and  $\mathcal{D}_3$  exhibit instability issues due to different powers of the exponential in the numerator and denominator and  $\mathcal{D}_1$  does not have a required sharpness expected from an RD function. Therefore, in this work, the RD function  $\mathcal{D}_4$  is selected for implementation in the virtual boundary method. The sharpness of this RD function is further controlled by using the  $\eta$  function as used in the definition of the corresponding RH

function. This is defined in Equation (4.9). The RD function for different values of  $\eta$  are shown in Figure 4.5.

$$\mathcal{D} = \frac{1}{\eta} \left( \frac{-\tanh^2\left(\frac{x}{\eta}\right) + 1}{2} \right) \quad (4.9)$$

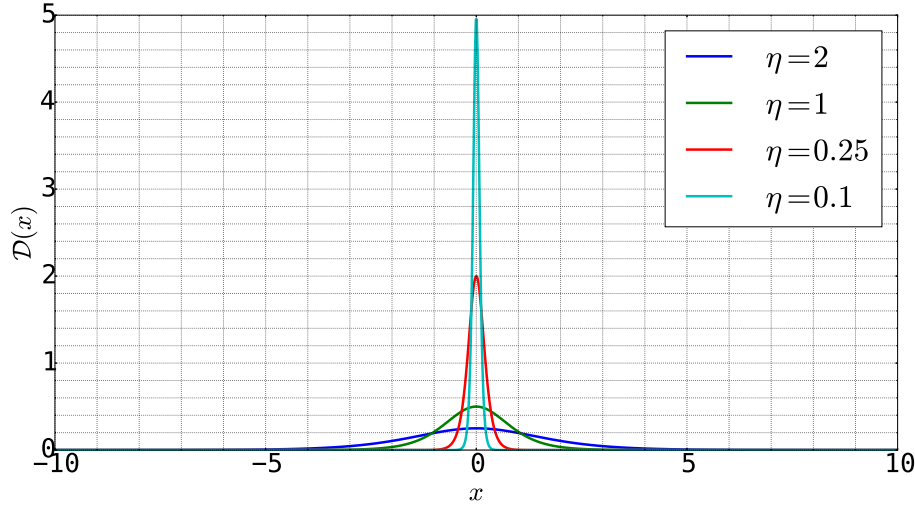


Figure 4.5: Effect of control parameter  $\eta$  on the RD function.

As shown in Figure 4.5, the RD function has continuous derivatives. This enables the virtual boundary method to be used for sensitivity calculation by providing differentiable governing equations. For the RD function, the free parameter is calculated by selecting how fast the RD function decays when moving further from its symmetry axis. The free parameter for the RD function is defined in Equation (4.10).

$$\eta = \frac{R}{\tanh^{-1}(\sqrt{1-p})} \quad (4.10)$$

The RD function drops to  $p$  percentage of its value at the symmetry axis at distance  $R$ . For example, for the RD function value to drop 99 percent ( $p = 0.99$ ) within 0.01 ( $R = 0.01$ ) of the symmetry axis of the RD function, the  $\eta$  value is calculated as 0.0033 based on Equation (4.10).

## 4.2 Sensitivity Analysis Formulation

In this section, the sensitivity equations are derived for IB representation of solid boundaries. Two separate IB methods are selected for the sensitivity analysis, the penalization method, and the virtual boundaries method. The direct sensitivity equations for design variables that control the shape of the IB are derived for these analysis and later applied on two different demonstration problems.

As mentioned in Chapter 2, the direct method for sensitivity analysis is preferred when the number of design variables are less than the number of functions for which the sensitivities are calculated for. For this approach, the governing equations are differentiated with respect to the arbitrary shape design variable,  $b$ .

For the penalization method, a level-set definition of the solid boundary is used to assign penalization factors to the nodes. As defined in Chapter 3, the boundary is defined using an analytical function,  $\mathcal{X}$ , that depends on the shape design variable. The governing equation for flow over the immersed boundaries using penalization method is written using the RH function:

$$\frac{\partial \mathbf{u}}{\partial t} + \mathbf{u} \cdot \nabla \mathbf{u} = -\frac{\nabla P}{\rho} + \nu \nabla^2 \mathbf{u} - \mathcal{H}(\mathcal{X}(b)) \kappa \mathbf{u} \quad (4.11)$$

Equation (4.11) is differentiated with respect to design variable  $b$  to derive the continuum sensitivity equations. The symbol  $( )'$  represents  $\partial/\partial b$  in the sensitivity equation (4.12).

$$\frac{\partial \mathbf{u}'}{\partial t} + \mathbf{u}' \cdot \nabla \mathbf{u} + \mathbf{u} \cdot \nabla \mathbf{u}' = -\frac{\partial P'}{\rho} + \nu \nabla^2 \mathbf{u}' - \underbrace{\frac{\partial \mathcal{H}}{\partial \mathcal{X}} \frac{\partial \mathcal{X}}{\partial b} \kappa \mathbf{u}}_{\text{effect of shape change}} - \mathcal{H}(\mathcal{X}) \kappa \mathbf{u}' \quad (4.12)$$

Equation (4.12) is solved for velocity and pressure sensitivities ( $\mathbf{u}', P'$ ) by knowing the values of  $\mathbf{u}$  from the analysis. As shown in Equation (4.12), the effect of shape change is introduced to the sensitivity equation through the derivative of the RH function.  $\partial \mathcal{H}/\partial \mathcal{X}$

is easily calculated by analytically differentiating the RH function with respect to  $\mathcal{X}$ . The evaluation of  $\partial\mathcal{X}/\partial b$  is also straight forward, since it was assumed that the solid boundary is defined analytically. The boundary conditions for Equation (4.11) are often independent of the shape design variables. Therefore, their derivative is typically zero. This enables us to solve the governing Equation of (4.12) for the sensitivity response.

Sensitivity implementation for the virtual boundary method is more demanding compared to the penalization method. Using the RD function, the NS equation using virtual boundary method for solid boundary definition is written as shown in Equation (4.13).

$$\frac{\partial \mathbf{u}}{\partial t} + \mathbf{u} \cdot \nabla \mathbf{u} = - \frac{\nabla P}{\rho} + \nu \nabla^2 \mathbf{u} + \\ \left\{ \alpha \int_0^t \left[ \int \mathbf{u}(\mathbf{x}, \tau) \mathcal{D}(\mathbf{x} - \mathbf{X}) d\mathbf{x} - \mathbf{V}(\mathbf{X}, \tau) \right] d\tau + \right. \\ \left. \beta \int \mathbf{u}(\mathbf{x}, t) \mathcal{D}(\mathbf{x} - \mathbf{X}) d\mathbf{x} - \mathbf{V}(\mathbf{X}, t) \right\} \mathcal{D}(\mathbf{x} - \mathbf{X}) \quad (4.13)$$

where  $\mathbf{V}(\mathbf{X}, t)$  is the desired velocity at the Lagrangian point on the solid boundary and  $\int \mathbf{u}(\mathbf{x}, t) \mathcal{D}(\mathbf{x} - \mathbf{X}) d\mathbf{x}$  is the current velocity at the Lagrangian node,  $\mathbf{X}$ , on the solid boundary calculated from the Eulerian nodes on the fluid's domain. To transfer the forces back to the Eulerian nodes, the same RD function is used as shown in Equation (4.13) by  $\mathcal{D}(\mathbf{x} - \mathbf{X})$  where the term in the parenthesis  $(\mathbf{x} - \mathbf{X})$  is responsible for casting the RD function at the location of the Lagrangian point  $\mathbf{X}$ . The maximum value for the RD function  $\mathcal{D}$  is normalized to one. This is essential to have a conservative transformation between the Eulerian and Lagrangian computational nodes. The mapping procedure is illustrated in the following example.

Assume that the analytical function  $y = x^2$  is evaluated at 9 locations between 0 and 1. To know the function value at locations  $X = 0.3321$  and  $X = 0.5813$ , that do not coincide with the location where the function is evaluated, it is required to use the following

equation. We used the RD definition of Equation (4.9) with  $\eta = 0.1$  for this purpose.

$$y(X) = \sum_{i=1}^9 \mathcal{D}_i Y_i \Delta x_i \quad (4.14)$$

Where the subscript  $i$  is the number of points used to discretize the Delta function. This equation used the data from nodes around  $X$  to calculate the function value. To convert the data at  $X$  (Lagrangian node) back to the surrounding nodes where the original function was evaluated, the following equation is used.

$$y(x) = y(X) \bar{\mathcal{D}}(x - X) \quad (4.15)$$

Where  $\bar{\mathcal{D}}(x - X)$  is a constant vector. The transfer of data from Eulerian nodes to Lagrangian is shown in Figure 4.6. In this figure, the original function is represented by the solid black line and the sampling locations are represented by black circles. The exact function value at the Lagrangian point is shown by a red circle and the calculated value from Equation (4.14) is shown by a blue cross. The numerical results for the comparison between the interpolated and actual values are shown in Table 4.1. The green squares represent the mapped back data to the Eulerian domain from the data at the Lagrangian point  $X$  shown with a red circle in Figure 4.6. As shown here, the data at Lagrangian nodes mainly affects the two closest Eulerian nodes. The effect of Lagrangian data at  $X$  decreases by moving further from  $X$ . The mapping from the Lagrangian to Eulerian domain has larger error compared to the mapping from Eulerian to Lagrangian grid. However, since this is done in a loop, the error diminishes as the simulation continues in time.

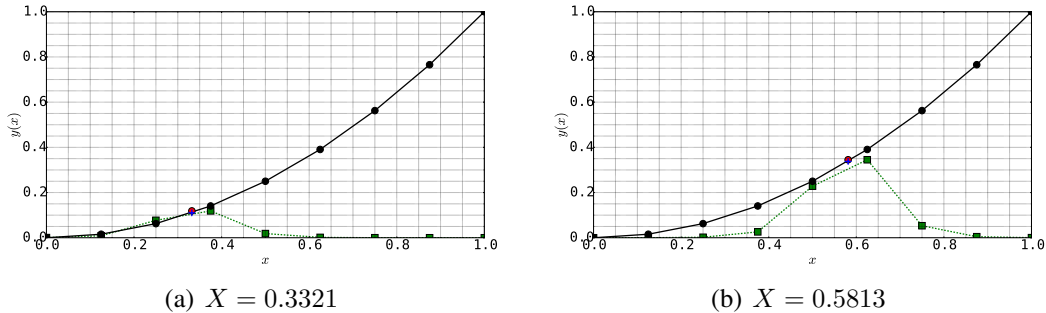


Figure 4.6: Results mapping between the Eulerian and Lagrangian computational nodes.

Lagrangian node location ( $X$ )	Absolute error
0.3321	0.0077
0.5813	0.0021

Table 4.1: Comparison between the true and interpolated results using the RD function at arbitrary Lagrangian location,  $X$ .

Using this continuous mapping between the Eulerian and Lagrangian domains, the governing equation (4.13) is differentiated with respect to design variable  $b$  to derive the sensitivity equations.  $(\cdot)'$  is used instead of the sensitivity operator,  $\partial/\partial b$ .

$$\begin{aligned}
& \frac{\partial \mathbf{u}'}{\partial t} + \mathbf{u}' \cdot \nabla \mathbf{u} + \mathbf{u} \cdot \nabla \mathbf{u}' = -\frac{\nabla P'}{\rho} + \nu \nabla^2 \mathbf{u}' + \\
& \left\{ \alpha \int_0^t \left[ \int \mathbf{u}'(\mathbf{x}, \tau) \mathcal{D}(\mathbf{x} - \mathbf{X}) d\mathbf{x} + \int \mathbf{u}(\mathbf{x}, \tau) \frac{\partial \mathcal{D}}{\partial X} \frac{\partial X}{\partial b} d\mathbf{x} \right] d\tau + \right. \\
& \left. \beta \int \mathbf{u}'(\mathbf{x}, t) \mathcal{D}(\mathbf{x} - \mathbf{X}) d\mathbf{x} + \int \mathbf{u}(\mathbf{x}, t) \frac{\partial \mathcal{D}}{\partial X} \frac{\partial X}{\partial b} d\mathbf{x} \right\} \mathcal{D}(\mathbf{x} - \mathbf{X}) + \\
& \left\{ \alpha \int_0^t \left[ \int \mathbf{u}(\mathbf{x}, \tau) \mathcal{D}(\mathbf{x} - \mathbf{X}) d\mathbf{x} - \mathbf{V}(\mathbf{X}, \tau) \right] d\tau + \right. \\
& \left. \beta \int \mathbf{u}(\mathbf{x}, t) \mathcal{D}(\mathbf{x} - \mathbf{X}) d\mathbf{x} - \mathbf{V}(\mathbf{X}, t) \right\} \frac{\partial \mathcal{D}}{\partial X} \frac{\partial X}{\partial b} \quad (4.16)
\end{aligned}$$

Equation (4.16) is solved for the sensitivity response  $\mathbf{u}'$ , where  $\mathbf{u}$  is known from the analysis results. The effect of shape change is introduced in the sensitivity equation through the derivative of the RD function,  $\frac{\partial D}{\partial X} \frac{\partial X}{\partial b}$ . The first term in this description is easily calculated since the RD function is known. The derivative of Lagrangian node location,  $X$ ,

to the design variable,  $b$ , is known since the solid boundary is defined analytically. The boundary conditions of Equation (4.13) are often design independent and have zero sensitivity. However, as showed in the work of Cross and Canfield [85], the order of which the boundaries are defined can greatly affect the accuracy of sensitivity results. This can be addressed by either using higher order methods to approximate the boundaries or using Spatial Gradient Reconstruction (SGR) technique of Cross and Canfield [22]. In this work we used higher order boundary approximation to address this issue.

### 4.3 Shape Sensitivity Analysis for 1D problem

For the first benchmark case, we looked at the flow between two plates that was defined in Section 3.3. The governing equation and boundary conditions for this problem is shown in Equation (4.17). The boundary condition is defined as  $u = U$  at  $y = L$ .

$$u_t = \mu u_{yy} \quad \text{in } \Omega_f \quad (4.17a)$$

$$\begin{cases} u = U & \text{at } y = 0 \\ u = 0 & \text{at } y = L \end{cases} \quad (4.17b)$$

The analytical result for the steady-state velocity profile between the two plates is:

$$u = U \frac{L - x}{L} \quad (4.18)$$

This enables us to treat the moving wall velocity ( $U$ ) and the distance between the two plates ( $L$ ) as design variables. The sensitivity of the steady-state velocity profile between the two plates to these design variables is calculated using CSA. The results of the CSA are

verified with the analytical sensitivity results in Equation (4.19).

$$\frac{\partial u}{\partial L} = \frac{Ux}{L^2} \quad (4.19a)$$

$$\frac{\partial u}{\partial U} = \frac{L - x}{L} \quad (4.19b)$$

For this benchmark problem, the flow is modeled using two different immersed boundary techniques introduced at the beginning of this chapter: penalization method and the virtual boundary method. The difference between the flow analysis from Chapter 3 is the use of RH and RD functions instead of discontinuous step and delta functions. Therefore, first the effects of these modifications are investigated.

For the flow simulation using the penalization method of Equation (4.3), I investigated the effect of number of nodes and the moving wall velocity of the solution. To have a stable solution, the flow analysis time step cannot be larger than  $2/\kappa$  where  $\kappa$  is the porosity value that is selected to model the solid domain. For this analysis, the  $\eta$  value of the RH function is selected based on the criteria that 99 percent change of the RH function occurs within two mesh cells. The result for the simulation based on RH function is compared with the step function solution in Figure 4.7.

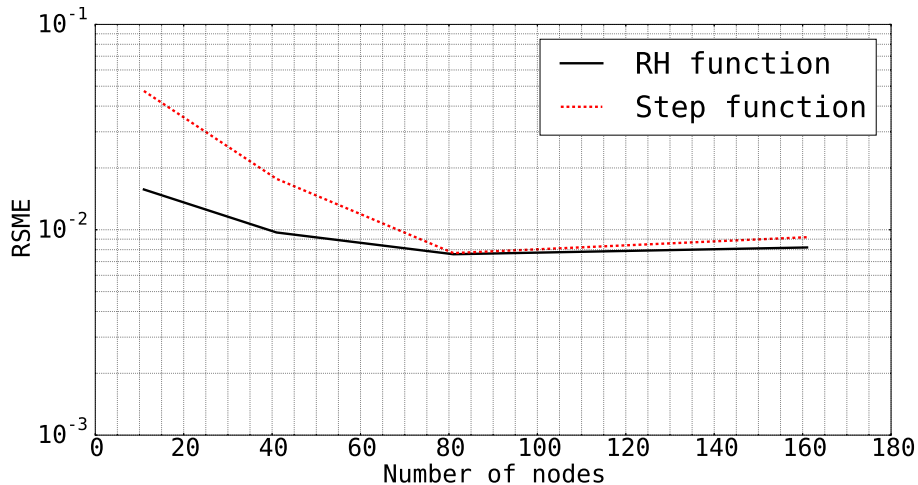


Figure 4.7: Effect of Regularized Heaviside (RH) and step functions on the solution accuracy.

As shown in Figure 4.7, the results of the RH function are more accurate compared to the step function. The effect of wall velocity on the accuracy from the simulation was also investigated. The wall velocity was selected as  $1m/s$ ,  $10m/s$ ,  $100m/s$ , and  $1000m/s$ . However, this did not affect the simulation accuracy.

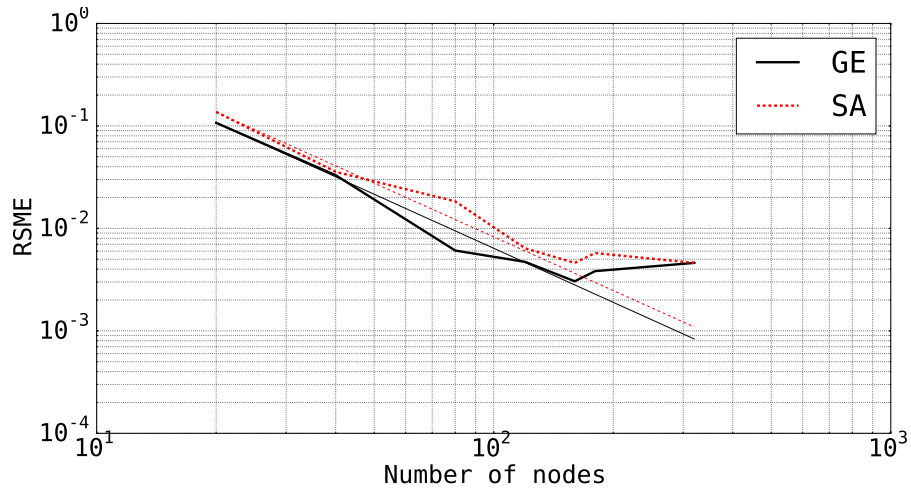
The sensitivity equations for the penalization technique are derived by differentiating the governing equation as shown in Equation (4.12). However, for this problem, the convective terms and pressure gradient drop out, from the derivation, resulting in the sensitivity equation

$$\frac{\partial u'}{\partial t} = \mu \frac{\partial^2 u'}{\partial x^2} + \kappa \left[ \frac{\partial \mathcal{H}}{\partial X} \frac{\partial X}{\partial b} + \mathcal{H}(X)u' \right] \quad (4.20)$$

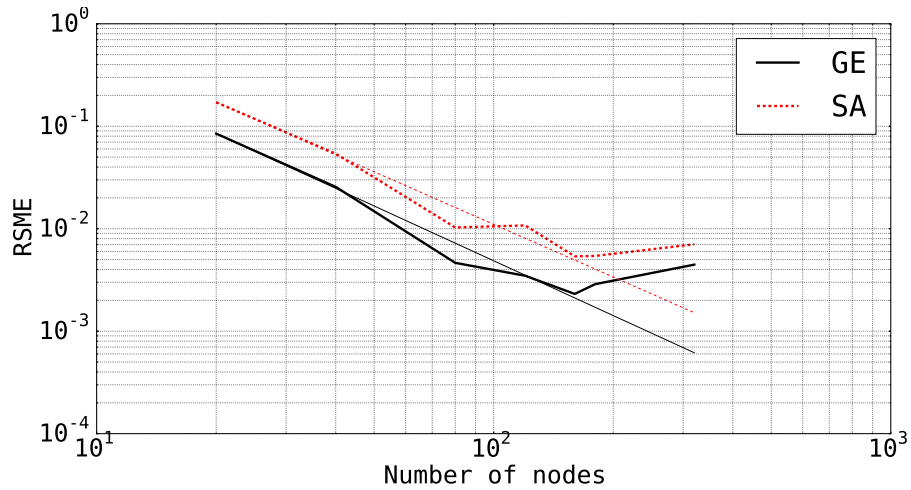
Where  $X$  is  $x - x_w$  and  $x_w$  is the solid wall location .  $u$  is the flow velocity,  $\mu$  is the viscosity,  $\kappa$  is the porosity, and  $\mathcal{H}$  is the RH function.  $b$  corresponds to a generic design variable and  $u'$  is the flow field sensitivity to the design variable,  $b$ . The boundary conditions are derived by differentiating Equation (4.17b); this is shown in Equation (4.21). Both boundary conditions are zero because their location does not change by changing the design variable.

$$\begin{cases} u' = 0 & \text{at } x = 0 \\ u' = 0 & \text{at } x = 1 \end{cases} \quad (4.21)$$

For this problem,  $\kappa$  is selected as  $2^4$  based on the convergence studies for the governing equations, and the sensitivity of the velocity profile with respect to the distance between two plates is verified with Equation (4.19a). The  $\eta$  parameter for the RH function is selected in such a way that 95 percent of change in RH function occurs within two nodes from the solid boundary. This ensures the stability of the method. The wall initial locations are selected as  $x_{wall} = 0.4321$  and  $x_{wall} = 0.7583$ . Neither of these locations coincide with the computational nodes in the domain. The effect of the number of nodes on the accuracy of the solution of the governing equations. Sensitivity results are shown in Figure 4.8.



(a)  $x_{wall} = 0.4321$



(b)  $x_{wall} = 0.7583$

Figure 4.8: RSME value for the sensitivity analysis (SA) and governing equation (GE). The thick lines represent the actual values for the RSME error and the thin lines represent the least-square approximation of the best fit.

The thin lines in Figure 4.7 represent the curve fit using function  $y = ae^{bx}$  through the RSME values. The slope of this line is  $-1.75$  for both of these analyses. This means that the convergence rate is the same for governing equations and sensitivity analysis in this problem. The error source between the analytical and the CSA is better investigated by looking at the comparison between the sensitivity of the velocity profile to the distance between the plates as shown in Figure 4.9.

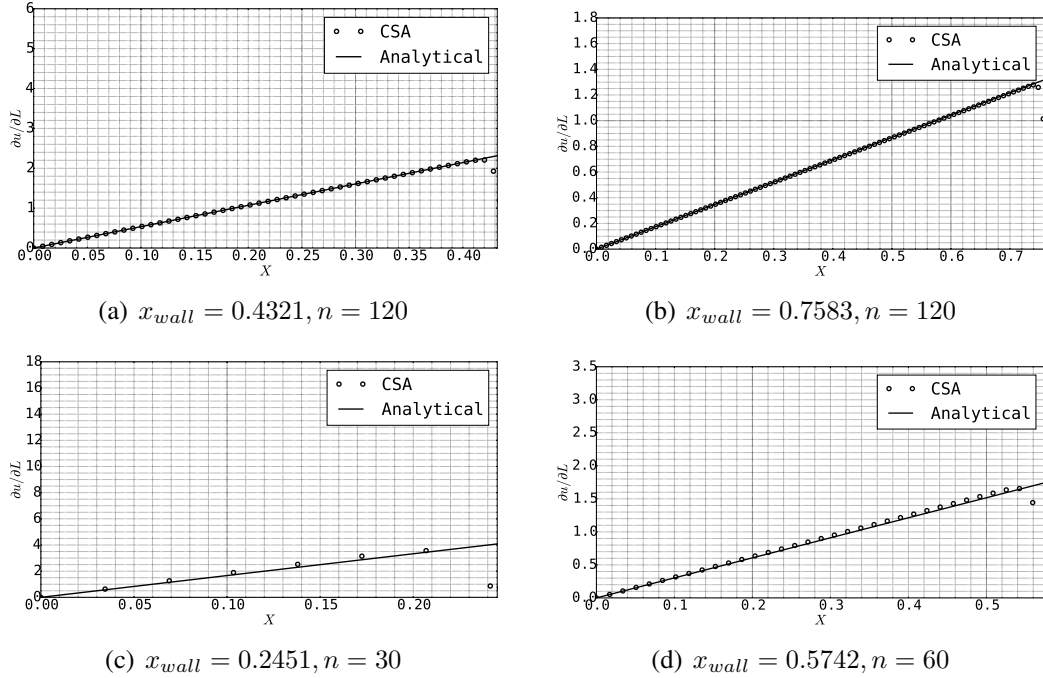


Figure 4.9: Comparison between the velocity sensitivity profile of CSA and analytical results in the domain.  $w_{wall}$  is the location of the stationary wall and  $n$  is the number of nodes used to discretize the domain.

As shown in Figure 4.9, the accuracy of CSA results starts to decay near the boundary. It should be noted that this domain corresponds to the region that we chose the RH function value to have its 99 percent change. Therefore, the size of this region is known prior to the analysis. As shown in Figure 4.9, decay of accuracy near the walls did not affect the sensitivity results in regions further away from the boundary. Sensitivity response near the boundaries is improved by using higher order method to represent the boundary. The results based on higher order boundary representation are shown in Figure 4.10.

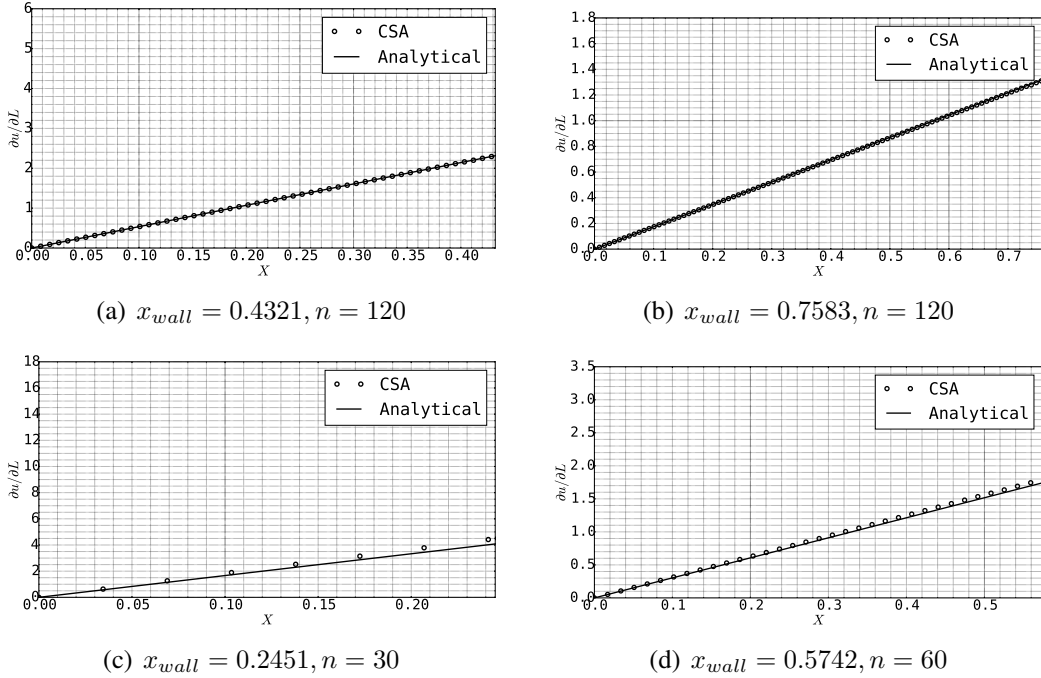


Figure 4.10: Improving the sensitivity results by using higher order boundary representation.

This problem is also solved using the virtual boundary method and the results are compared with the penalization method regarding the accuracy of simulation cost. The simulation cost is defined as the number of time steps it takes to reach a converged value. The virtual boundary method is based on solving the Navier-Stokes equation (4.1) and modeling the boundaries through the force term defined in Equation (4.4). As mentioned in Section 4.1, the RD function needs to be used in the virtual boundary method to have a differentiable governing equation for CSA. Therefore, the effect of the RD function on the accuracy of the solution is first investigated.

The RD function for this simulation is selected as the one in Equation (4.9). The  $\eta$  parameter is based on Equation (4.10) where  $p = 0.99$  and  $R = 2dx$ . This ensures the solution stability. For this analysis,  $\alpha$  and  $\beta$  constants in Equation (4.4) are each selected as  $-100$ . The convergence result is shown in Figure 4.11. As shown here, the simulation with RD function has better convergence properties than the delta function.

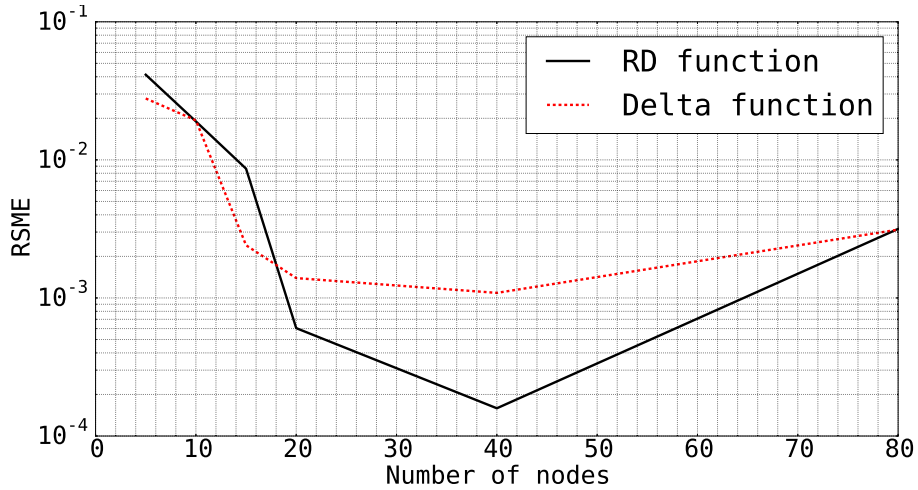


Figure 4.11: Effect of Regularized Delta (RD) and delta function on the solution accuracy.

The effect of wall velocity accuracy of the simulation was also investigated. The wall velocity was selected as  $1m/s$ ,  $10m/s$ ,  $100m/s$ , and  $1000m/s$ . However, this did not affect the accuracy of the simulations.

The sensitivity equations are derived by differentiating the Navier-Stokes equations as shown in Equation (4.16). However, for this problem, Equation (4.16) is simplified as shown in Equation (4.22).

$$\begin{aligned} \frac{\partial u'}{\partial t} = & \nu \nabla^2 u' + \\ & \left\{ \alpha \int_0^t \left[ \int u'(x, \tau) \mathcal{D}(x - X) d\mathbf{x} + \int u(x, \tau) \frac{\partial \mathcal{D}}{\partial X} \frac{\partial X}{\partial b} d\mathbf{x} \right] d\tau + \right. \\ & \left. \beta \left[ \int u'(x, t) \mathcal{D}(x - X) d\mathbf{x} + \int u(x, t) \frac{\partial \mathcal{D}}{\partial X} \frac{\partial X}{\partial b} d\mathbf{x} \right] \right\} \bar{\mathcal{D}}(x - X) + \\ & \left\{ \alpha \int_0^t \left[ \int u(x, \tau) \mathcal{D}(x - X) d\mathbf{x} \right] d\tau + \beta \int u(x, t) \mathcal{D}(x - X) d\mathbf{x} \right\} \frac{\partial \bar{\mathcal{D}}}{\partial X} \frac{\partial X}{\partial b} \quad (4.22) \end{aligned}$$

Where  $X$  is the wall location. Equation (4.22) required the calculation of the RD function of Equation (4.9). This function is known as the doublet function [86] and is written as shown in Equation (4.23). The  $\eta$  value for this function is the same one chosen for the RD function. The doublet function of Equation (4.23) is plotted in Figure 4.12 for different

values of  $\eta$ .

$$T(x, \eta) = \frac{\left[ \tanh^2 \left( \frac{x}{\eta} \right) - 1 \right] \tanh \left( \frac{x}{\eta} \right)}{\eta^2} \quad (4.23)$$

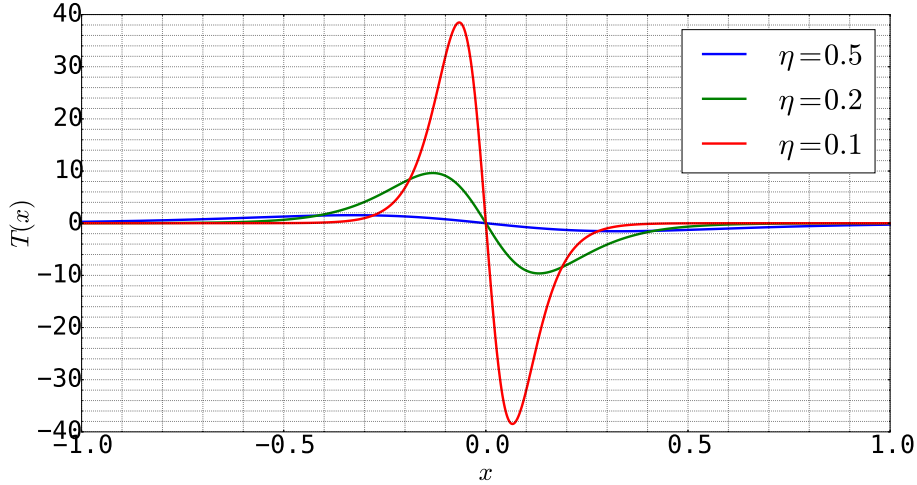


Figure 4.12: Doublet function of Equation (4.23).

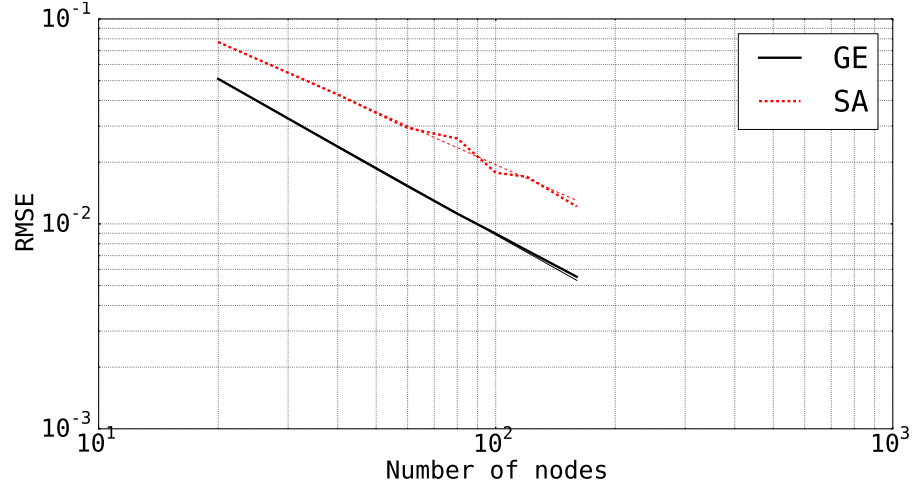
The boundary conditions for Equation (4.22) are defined by differentiating the boundary conditions in Equation (4.17b). Since neither of these boundary conditions depend on the design variable, the boundary conditions for Equation (4.22) are equal to zero. This are defined in Equation (4.24).

$$\begin{cases} u' = 0 & \text{at } x = 0 \\ u' = 0 & \text{at } x = 1 \end{cases} \quad (4.24)$$

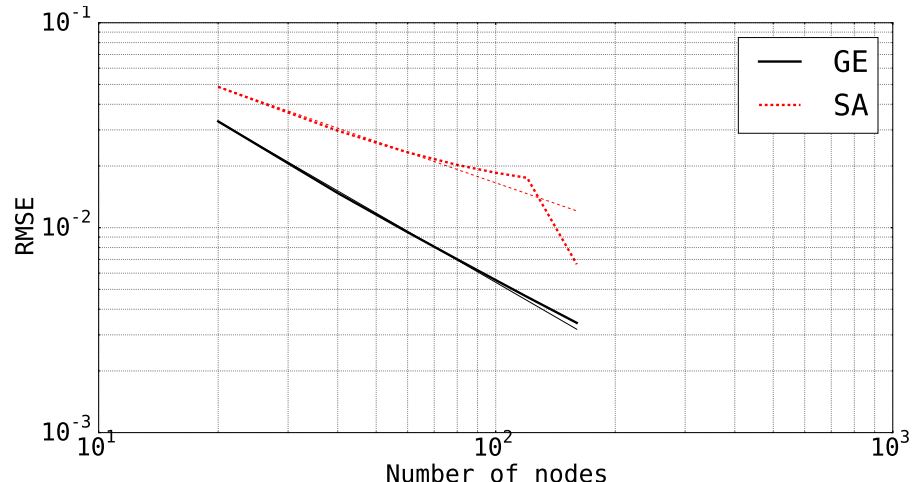
The analytical results of the sensitivity of velocity profile to the length are defined in Equation (4.19a) and used for verifying the sensitivity results.

The convergence results for the sensitivity analysis are shown in Figure 4.13. We looked at two different wall locations and moving wall velocities. The wall location is defined as  $x_{wall} = 0.6981m$  and  $x_{wall} = 0.4327m$  with the velocities  $U = 1m/s$  and  $U = 1000m/s$ , respectively. The thick line represents the RSME data value and the thin line represents the line with equation  $y = ax^b$  passing through the data points. The slope of this line is reported as  $-0.85$  for the sensitivity analysis and  $-0.95$  for the governing

equations. This slope describes the convergence rate of the method.



(a)  $x_{wall} = 0.4327, U_{wall} = 1000$



(b)  $x_{wall} = 0.6981, U_{wall} = 1$

Figure 4.13: RSME value for the sensitivity analysis (SA) and governing equation (GE). The thick lines represent the actual values for the RSME error and the thin lines represent the least-square approximation of the best fit.

To better investigate the sensitivity results, we looked at the velocity sensitivity profile between the two plates in Figure 4.14. As seen here, the accuracy of the sensitivity results decays near the perturbed boundary. As before, the accuracy decay near the boundary is fixed by using higher order boundary representation as shown in Figure 4.15.

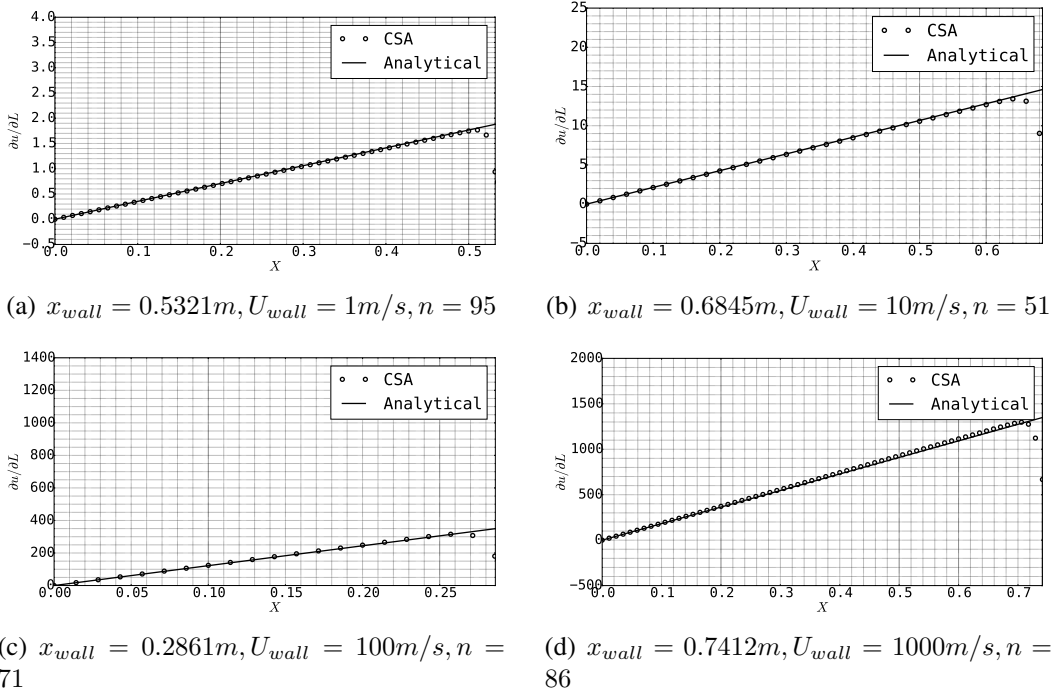


Figure 4.14: Velocity sensitivity profile between the two plates.

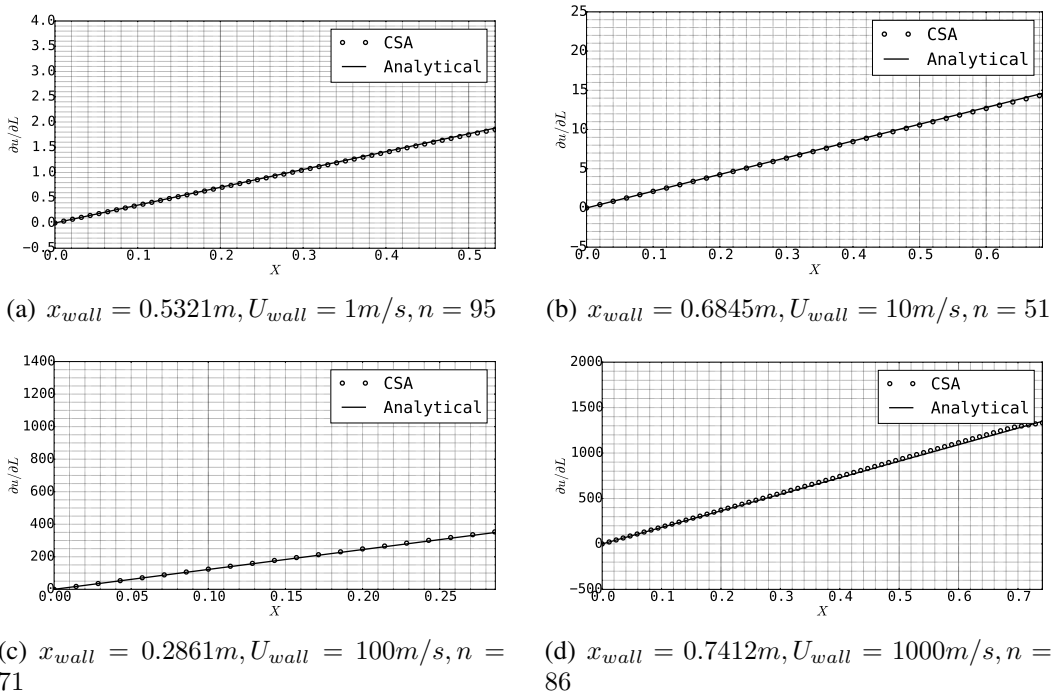


Figure 4.15: Effect of higher order boundary definition on the sensitivity analysis.

While the accuracy of the results is the same with the penalization technique and the

virtual boundary method throughout the domain, the virtual boundary method has better stability characteristics, meaning that a larger time step can be used for the numerical integration. This reduces the cost associated with the simulation. Moreover, the penalization method is only capable of enforcing the zero velocity on the immersed boundary, whereas with the virtual boundary method an arbitrary velocity  $V(X, t)$  can be defined on the immersed boundary as shown in Equation (4.4). This makes the virtual boundary method a more general method for the treatment of solid boundaries. Therefore, for the rest of the benchmark problems, the virtual boundary method is used.

## 4.4 Shape Sensitivity of Flow Over a Cylinder

For the second demonstration problem, the flow over a cylinder is modeled via the virtual boundary method using Equation (4.13) and the sensitivity of the flow field variables (velocity and pressure) with respect to the radius of the cylinder is calculated. For this problem, the domain is defined as a rectangle with the cylinder located on the horizontal symmetry line as shown in Figure 4.16.

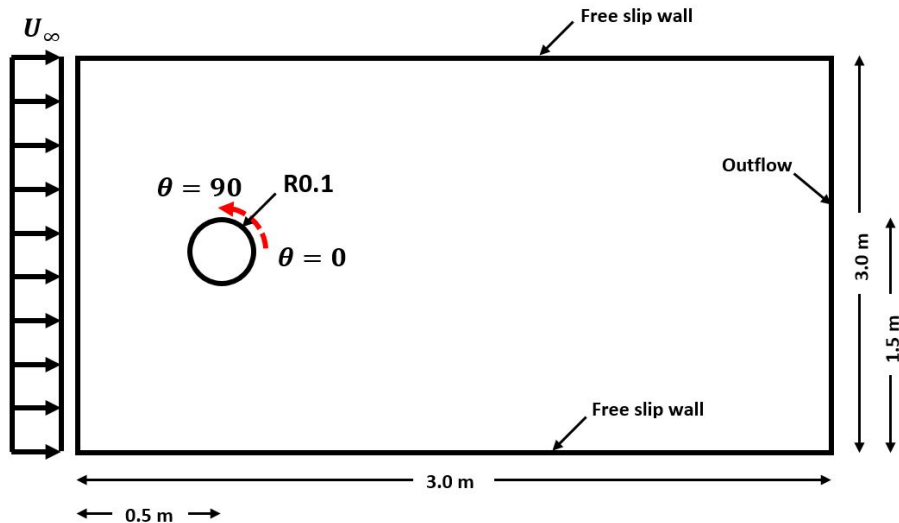


Figure 4.16: Physical domain with dimensions for flow over cylinder.

The boundary conditions are defined as the flow velocity at the inlet (left boundary)

and the outflow (zero gradient) boundary condition at the outlet (right boundary). The top and bottom boundaries are modeled as free slip walls. The pressure boundary conditions are defined as zero gradient on inlet, top, and bottom wall and zero dirichlet boundary condition at the outlet. The surface of the cylinder is modeled by the virtual boundary method. The cylinder is located at  $(0.5, 1.5)$  and has the radius of  $0.1m$ . Its surface is represented by using 50 Lagrangian nodes. The  $\alpha$  and  $\beta$  values for this analysis are selected as  $-10^4$  and  $-50$ , respectively. These constants are problem dependent and are selected in such a way that the required velocity conditions are satisfied at the Lagrangian points. To ensure the stability of the numerical method, the CFL number is kept under one for all following analysis. This is done by selecting an appropriate time step for the chosen mesh size using Equation (4.25).

$$\frac{u\Delta t}{\Delta x} + \frac{v\Delta t}{\Delta y} \leq 1.0 \quad (4.25)$$

The mesh convergence for this problem for a Reynolds number of 100 is shown in Figure 4.17.

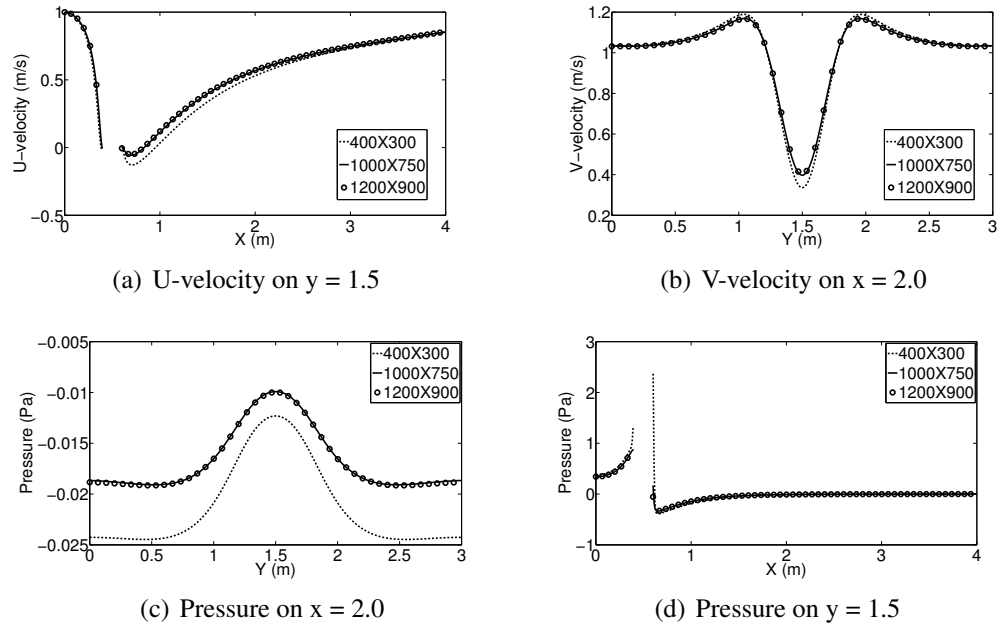


Figure 4.17: Convergence results for  $Re = 100$ .

The convergence study of the mesh refinement is also conducted for a node on the downwash of the cylinder at  $(2, 0)$  as shown in Figure 4.18. The slopes of the fitted curves to the u-velocity, v-velocity, and pressure error estimates are calculated as  $-2.34$ ,  $-1.96$ , and  $-2.72$ , respectfully. This means that the method is second-order accurate in space and time.

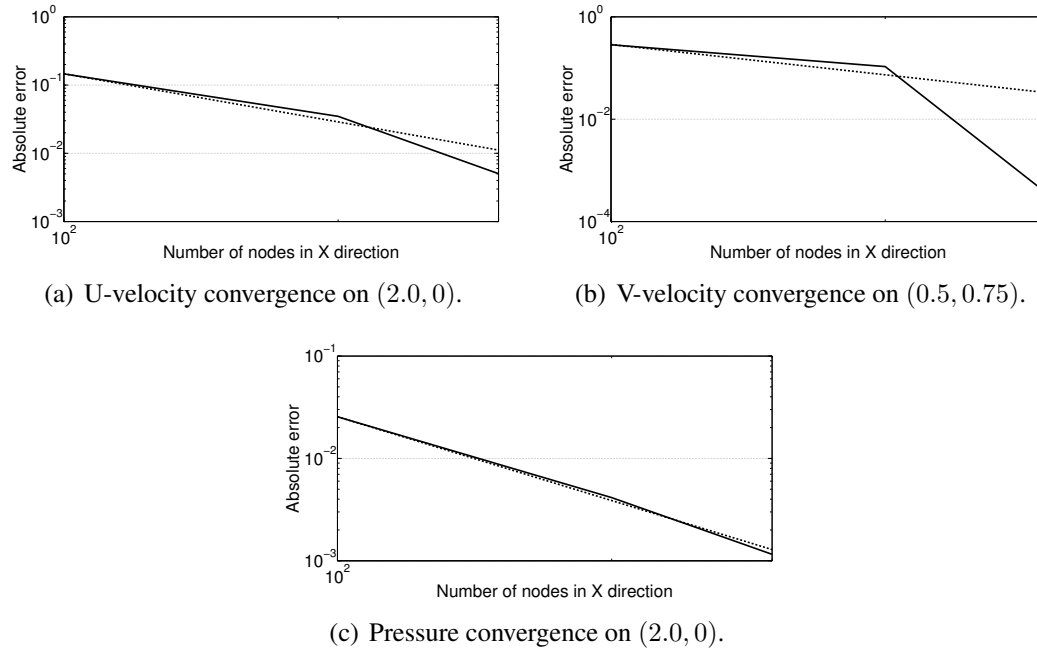


Figure 4.18: Convergence plots for  $\text{Re} = 100$ .

The contour plots for the velocity and pressure are shown in Figure 4.19.

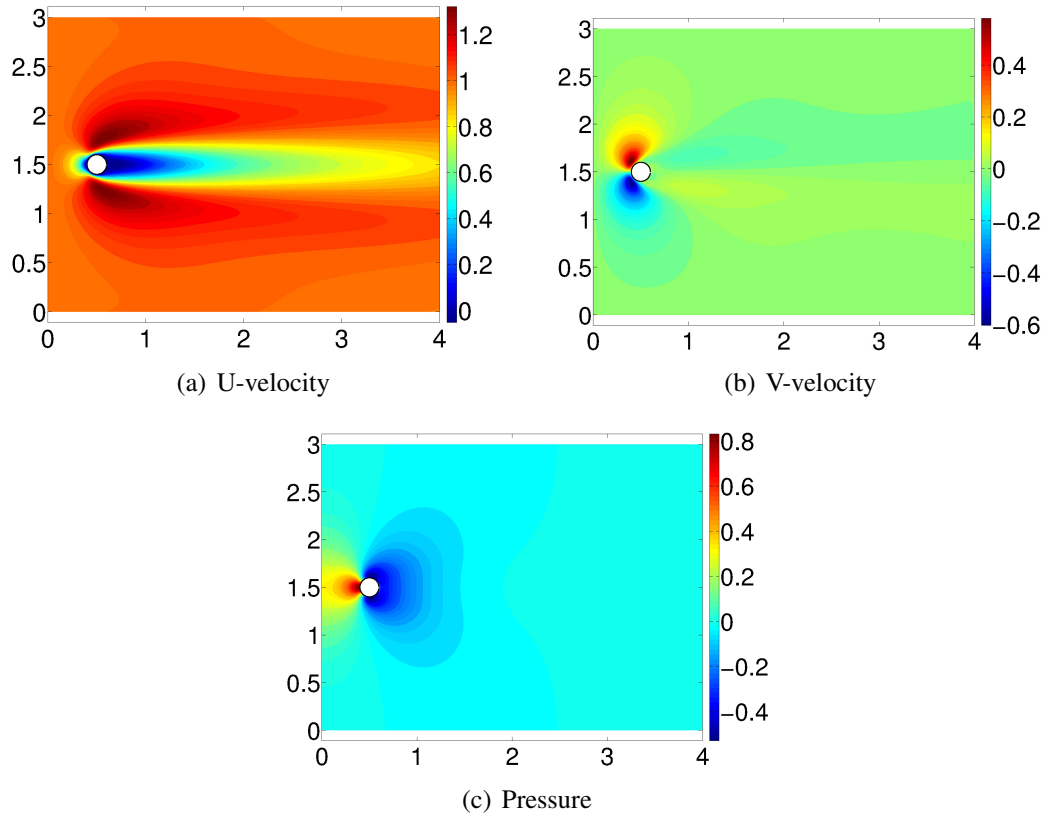


Figure 4.19: Velocity and pressure contours for  $\text{Re} = 100$ .

To ensure zero velocity on the solid boundary, we looked at the value of  $u$  and  $v$  velocities at the Lagrangian points on the boundary. These are shown in Figure 4.20. As shown here, the forcing terms brought the velocity to zero within the accuracy requirement.  $\theta$  is the polar coordinate of Lagrangian points on the cylinder surface as shown in Figure 4.16.

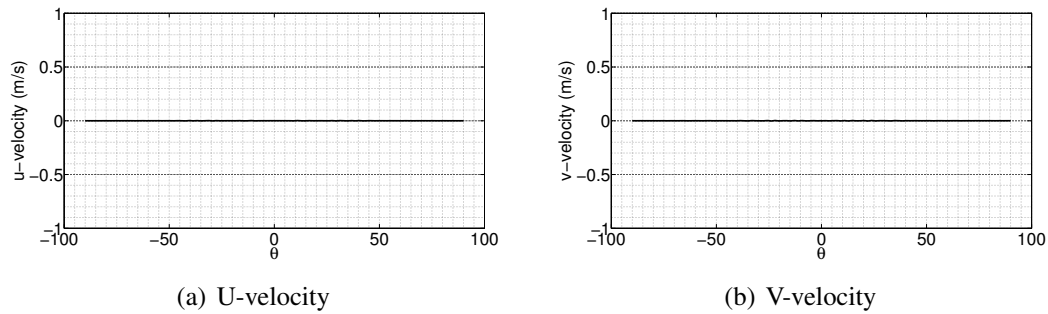


Figure 4.20: Velocity components on the solid boundary for  $\text{Re} = 100$ .

Finally, the pressure profile on the cylinder surface is calculated as shown in Figure 4.21. No smoothing is done for calculating the pressure values at the Lagrangian points. This data is interpolated using the RD function of Equation (4.9). As shown here, the pressure distribution on the boundary is smooth. This is in contrast to other IB methods that result in a non-smooth pressure profiles over the boundaries.

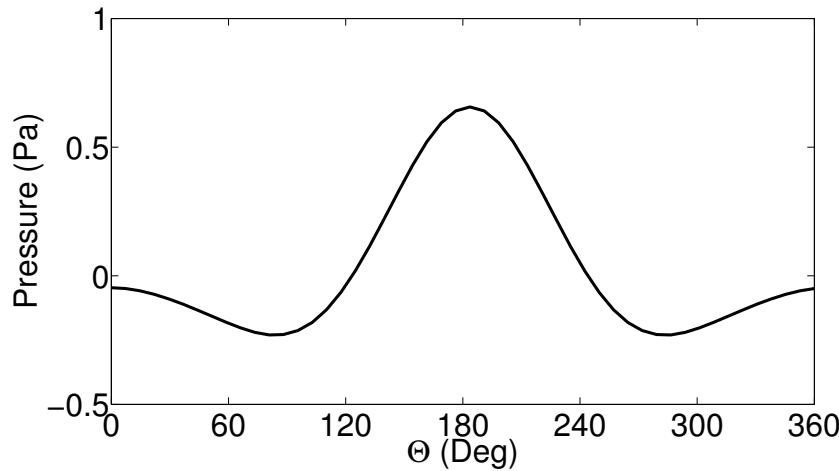


Figure 4.21: Physical domain with dimensions for flow over cylinder.

The continuum sensitivity equations are derived by differentiating the governing NS equations of (4.13) with respect to the shape design variable,  $b$ , as shown in Equation (4.16). For this problem, the cylinder boundary is defined using the following analytical level-set function. For the points on the cylinder surface, Equation (4.26) is equal to zero.

$$\mathcal{R}(x, y; r) : (x - x_0)^2 + (y - y_0)^2 = r^2 \quad (4.26)$$

For the sensitivity analysis,  $\partial D / \partial X$  is calculated easily, since the analytical form of the RD function is known (Equation (4.9)). It is possible to calculate the  $\partial X / \partial b$  values in Equation (4.16) by differentiating Equation (4.26). This is done in Equation (4.27).

$$\frac{\partial \mathcal{R}(x, y; r)}{\partial b} : 2(x - x_0) \frac{\partial x}{\partial b} + 2(y - y_0) \frac{\partial y}{\partial b} = 2r \frac{\partial r}{\partial b} \quad (4.27)$$

For this analysis, the design variable,  $b$ , is selected as the radius of the cylinder; therefore, the right-hand-side of Equation (4.27) reduces to  $2r$ .

The boundary conditions for the sensitivity analysis are defined by differentiating the original boundary conditions of the governing equations. These conditions do not depend on the design variables and therefore have zero values. These conditions are applied using a 4th order approximation on the boundaries of sensitivity equation. It should be noted that the solver uses 2nd order discretization vs the boundary condition. This is required for accurate sensitivity calculation. Obtaining the governing equations and boundary conditions, it is possible to solve the sensitivity equations.

The complex step method is used to validate the sensitivity response of the system. As mentioned in Chapter 1, the complex step method does not contain the accuracy issues of the finite difference method and provides the accurate sensitivities up to machine precision. However, the analysis code requires handling complex arithmetic. The analysis code is developed in MATLAB using the guidelines of [5] so that complex step can be used to calculate the sensitivities. The complex-step derivative is defined in Equation (1.1). The comparison of the CSA results with the complex step solution for the sensitivities of a different location in the domain is shown in Figure 4.22. The RMSE value is used to compare the results of continuum sensitivity analysis (CSA) and complex step (CS) method. Figure 4.22 shows an acceptable comparison between the CSA and CS results.

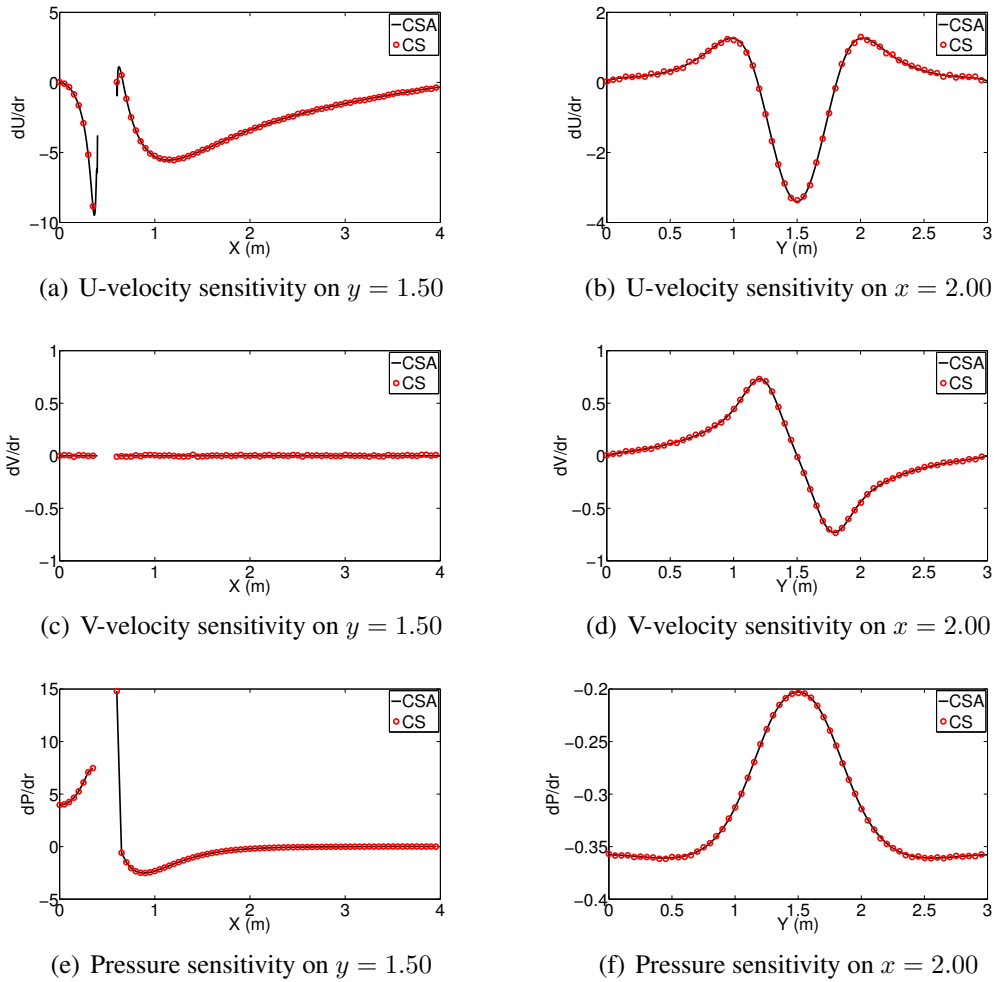


Figure 4.22: Verification of the flow variable sensitivities with respect to change in the cylinder radius for different location in the domain.

The rate of convergence of the sensitivity results are investigated in Figure 4.23. The slope of the fitted line (dashed line) for  $u$ -velocity,  $v$ -velocity, and pressure sensitivity are reported as  $-2.2$ ,  $-1.94$ , and  $-2.31$ , respectively. The  $v$ -velocity has lower convergence rate since the sampling location is near the wall when the spatial approximations are first order.

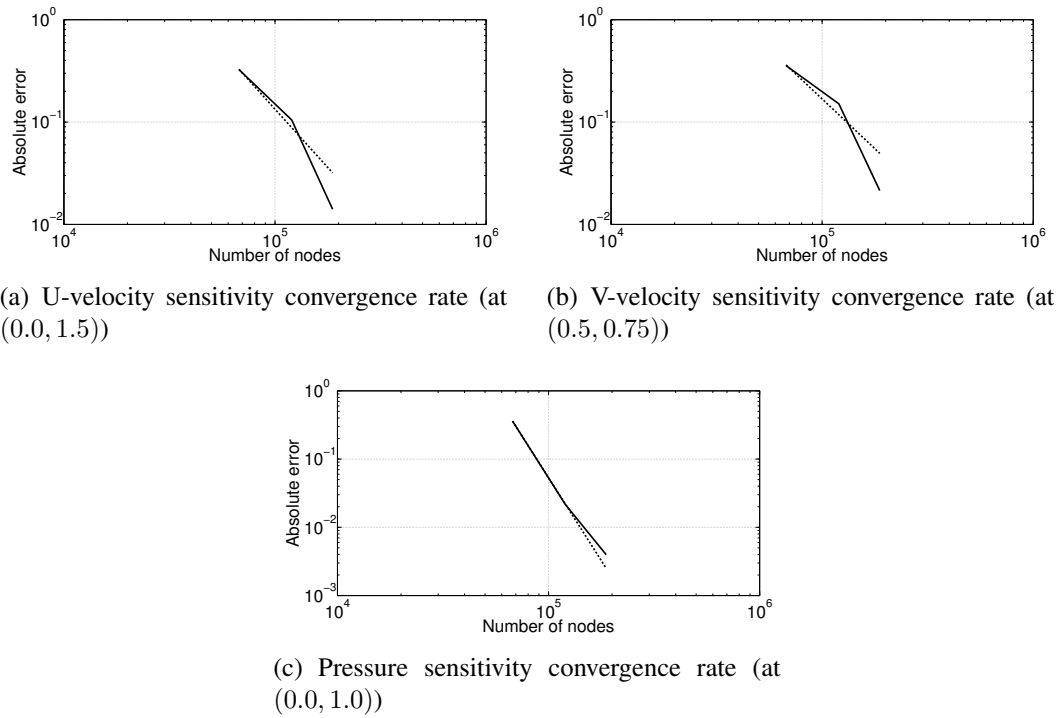


Figure 4.23: Convergence rate for the sensitivities ( $\text{Re} = 100$ ).

The sensitivity contours for the velocity and pressure are shown in Figure 4.24.

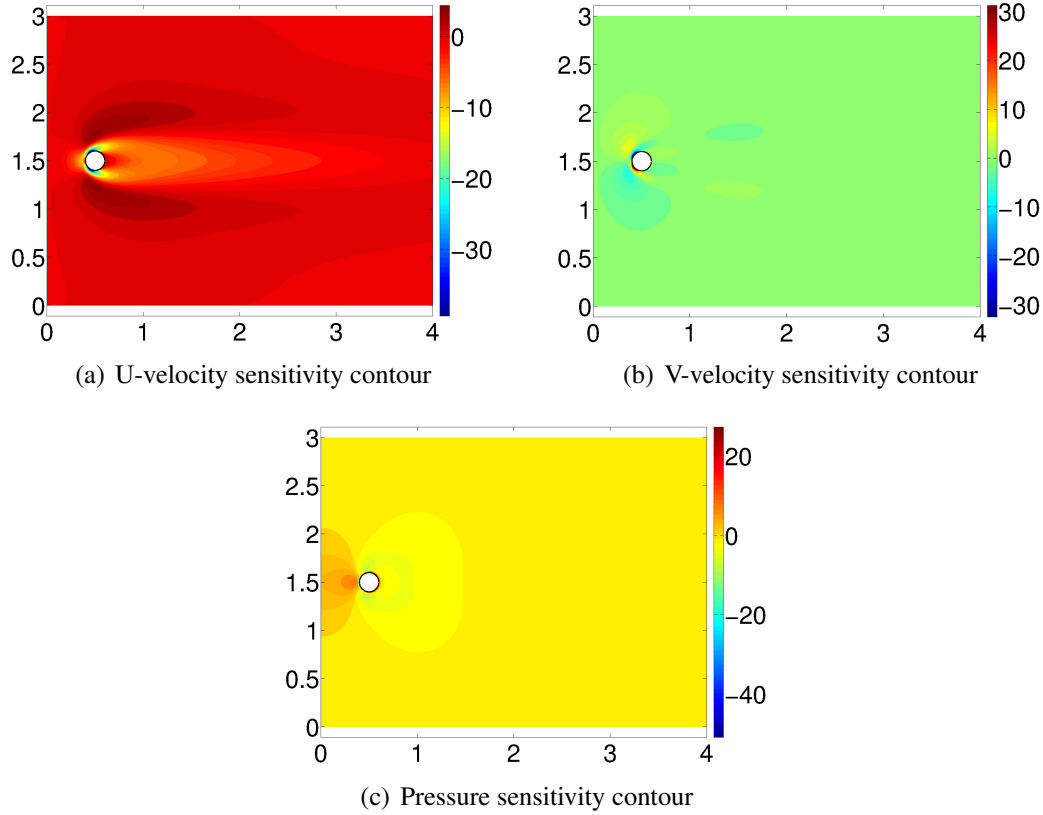


Figure 4.24: Sensitivity contours for  $\text{Re} = 100$ .

In most aerodynamic/aeroelastic designs, the sensitivity analysis is conducted for calculating the sensitivity of the pressure field on the surface of the solid boundaries. This sensitivity value is later used for calculating the sensitivity of aerodynamic forces acting on the solid boundaries by integrating the sensitivity of the pressure field. For this purpose, the sensitivity of the pressure field is plotted on solid boundaries and verified with the complex step method in Figure 4.25. It should be noted that Savitzky-Golay filtering is used to smooth the sensitivity results over the solid boundary. As shown in Figure 4.25, the two results agree very well with each other.

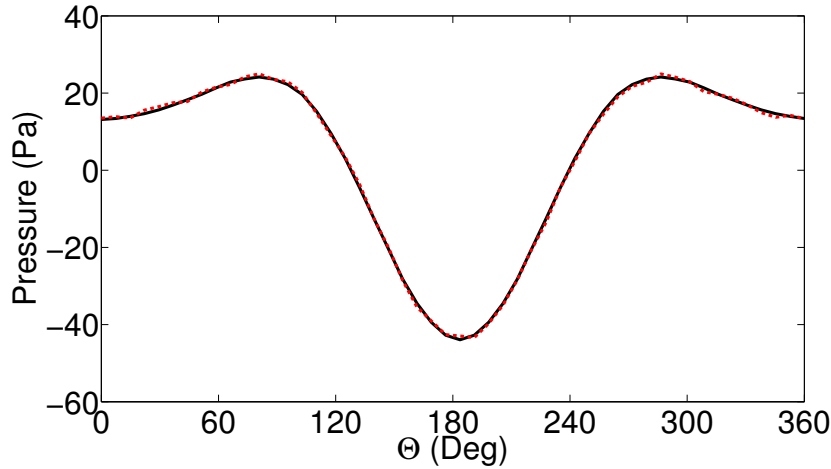


Figure 4.25: Comparison between pressure sensitivity results on the boundary for  $\text{Re} = 100$ .

## 4.5 Shape Sensitivity of Flow through a Nozzle

In this section, the flow in a convergent-divergent nozzle is modeled using the virtual boundary method and the sensitivity of flow with respect to the change of the shape of the nozzle is calculated. The shape of the nozzle is defined using three points: inlet, throat, and outlet. The inlet and outlet points are represented as red circles, while a red cross represents the throat point in Figure 4.26. The shape of the nozzle is approximated as a second-order polynomial passing through the point at the inlet and the throat node and separate second-order polynomial connecting throat and the outlet node. To ensure a smooth shape for the nozzle, the polynomials are forced to have zero derivatives at the throat. The throat area is controlled by the relative distance of the throat node from the symmetry line of the nozzle,  $y_t$ . This is selected as the design variable for sensitivity analysis. The analytical equation

of the nozzle's top wall in terms of the design variable,  $y_t$ , is written as

$$y(x) = \begin{cases} (0.61 - 2.04y_t)x^2 + (1.22y_t - 0.36)x + (0.81y_t + 0.55) & \text{if } 0.0 \leq x \leq 0.3 \\ (3.34 - 11.11y_t)x^2 + (6.67y_t - 2.0)x + 0.8 & \text{if } 0.3 < x \leq 1.0 \end{cases} \quad (4.28)$$

The bottom wall formula can be found by mirroring the top equation with respect to the symmetry line,  $y = 0.5$ .

The shape of the nozzle for different design variables are shown in Figure 4.26

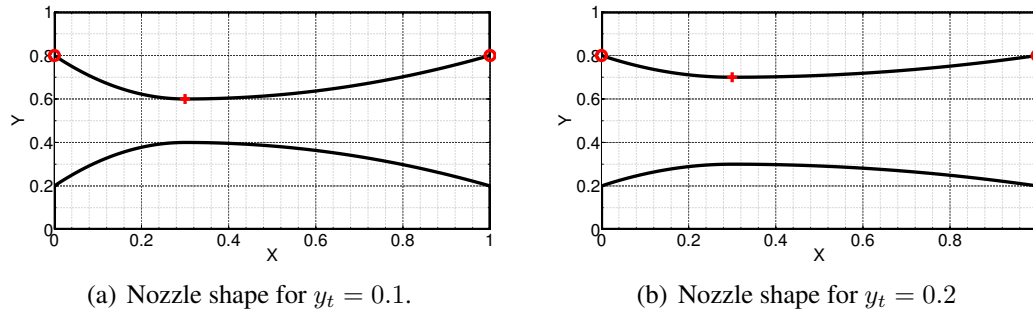


Figure 4.26: Effect of design variable on the shape of the nozzle.

The mesh convergence plots for the governing equations are shown in Figure 4.27. As shown here, the mesh size of  $500 \times 125$  is selected for the analysis.

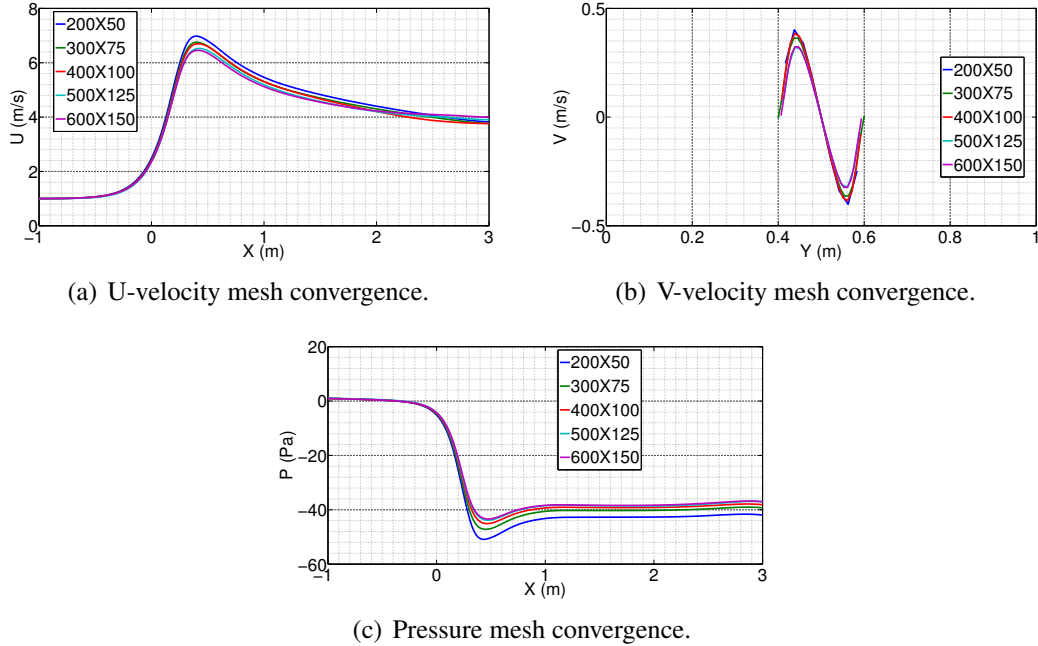
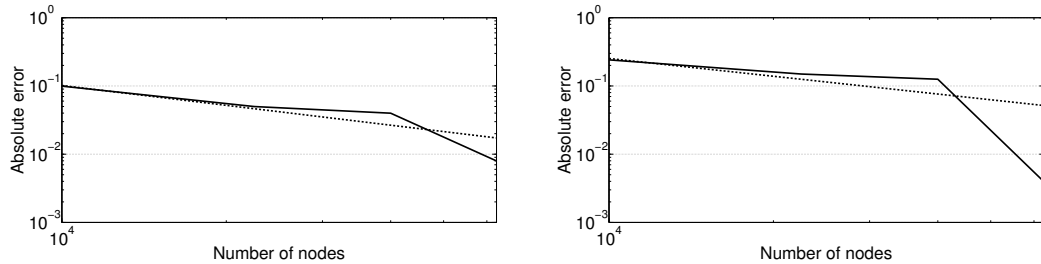
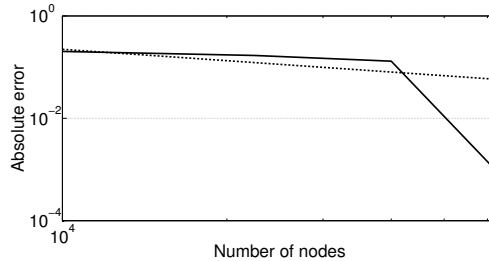


Figure 4.27: Mesh convergence study for the governing equation. The dashed line represent the fitted curve through points.

The convergence rate is shown in Figure 4.28. A mesh node at the throat area on the symmetry line is selected for this study for u-velocity and pressure. Since the v-velocity is zero for this point, a node at  $(0.3, 0.55)$  is selected for the convergence study of the v-velocity. The slope of the dotted line in Figure 4.28 is calculated as  $-0.96$ ,  $-0.86$ , and  $-0.73$  for u-velocity, v-velocity, and pressure error, respectfully. The convergence is close to first order due to the relative location of the points to the solid walls where the approximation is first order.



(a) U-velocity convergence rate at (0.3, 0.0). (b) V-velocity convergence rate at (0.3, 0.55).



(c) Pressure convergence rate at (0.3, 0.0)..

Figure 4.28: Mesh convergence study for the governing equation.

The contour plots for the velocities through the nozzle are shown in Figure 4.29. As shown here, the forcing function was able to model the walls and cause the flow to accelerate through the nozzle.

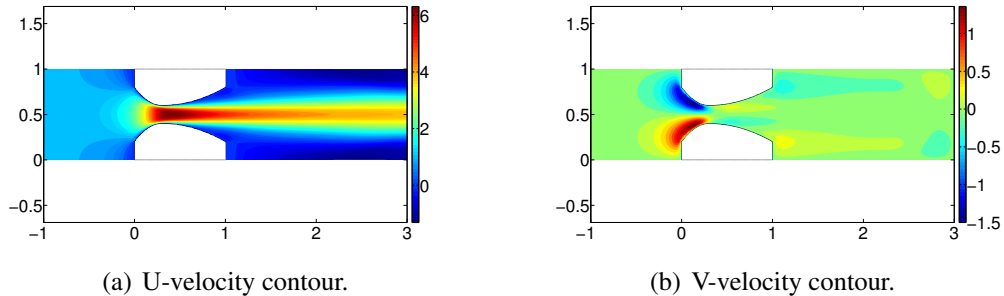


Figure 4.29: Contour plots for flow through nozzle ( $Re = 100$ ).

The sensitivity of the flow variables with respect to the throat area is calculated by differentiating the governing equations with respect to the design variable. The boundary conditions do not depend on the shape design variable; therefore, their derivative is equal to zero. This results in zero boundary conditions for the sensitivity equations.

The sensitivity of the flow with respect to the throat area is calculated using CSA. The u-velocity and pressure sensitivities are plotted on the symmetry line of the nozzle; whereas, the v-velocity sensitivity is plotted at the throat area. These values are verified with the complex step results where they showed a favorable comparison.

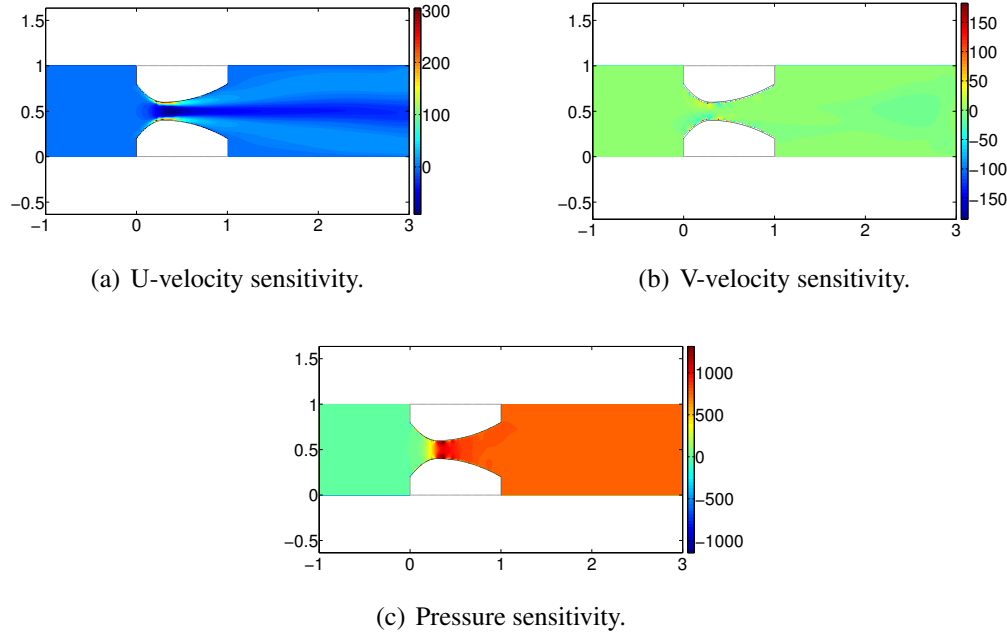


Figure 4.30: Sensitivity contours.

To verify the sensitivity analysis, the sensitivities of velocity and pressure are plotted on different locations in the domain. We chose the symmetry line of the nozzle to plot the u-velocity and pressure sensitivity with respect to the throat area and the vertical line passing through the throat for verifying the v-velocity sensitivity. The verification is done using the complex step sensitivities as shown in Figure 4.31.

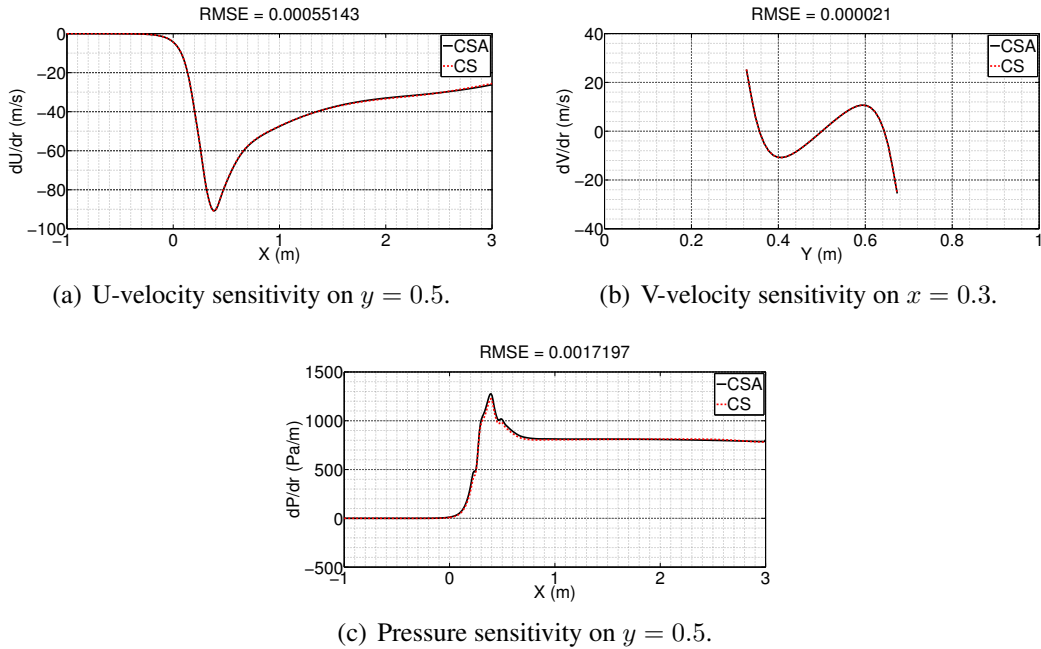


Figure 4.31: Verification of sensitivity results for the nozzle.

## 4.6 Summary

In this chapter, the Continuum Sensitivity Analysis (CSA) framework was applied to the Immersed Boundary (IB) formulation of flow over solid boundaries. In the conventional IB method, Heaviside and Delta functions are used to assign force terms to the governing equations to represent the effect of solid boundaries. To derive the sensitivity equations using the CSA, the governing equations need to be continuously differentiable; however, this is not true for conventional IB formulation. To address this issue, we introduced Regularized Heaviside (RH) and Regularized Delta (RD) functions to the governing equations. These functions are continuously differentiable and are tuned based on the grid size used in the simulation. The governing Navier-Stokes (NS) equations are rewritten based on two different continuous IB formulations and differentiated to get the sensitivity equations. To get accurate sensitivity response, it is required to use higher order boundary definition. The sensitivity equations were solved for the sensitivity of the flow variables with respect

to different shape design variables where the results were verified using the complex step method. It was shown that the CSA results are in good agreement with numerical results of the complex step method. The convergence rate of the sensitivity equations were also compared with the convergence rate of the governing equations. For the conducted analysis, it was reported that the sensitivity equations converge with the same rate as the governing equations.

# Chapter 5

## Shape Sensitivity Analysis for Coupled Fluid-Structure Interaction Design

Fluid-Structure Interaction (FSI) is a multiphysics coupling of the physical laws that govern fluid mechanics and structural dynamics. When fluid flows over or inside a structure, it causes stresses on the solid object. These stresses, depending on the magnitude, can cause small or large deformations in the structure; this results in a change of its shape. The effect of small deformations of the solid can be neglected since they do not affect the fluid flow. However, if the deformations are large, the pressure and velocity field of the fluid will change as a result.

In this chapter, we start with a survey of different coupling and solution methods available for solving a coupled FSI problem. To handle the mesh deformation shortcoming of large structural deformations, we will propose the IB method for managing these multiphysics simulations. We will build on the work of Chapter 4 to develop shape sensitivity analysis for a coupled FSI system. The shape sensitivity analysis developed here is demonstrated on various coupled systems. Throughout this chapter we consider the flow of *incompressible laminar Newtonian fluid* governed by Navier-Stokes (NS) equations in-

teracting with an *elastic structure*.

## 5.1 Fluid-Structure Interaction

Fluid-structure interactions are vital in the design of numerous engineering systems such as aircraft and turbine blades, while especially vital in designs where fatigue is the dominant mode of failure. Neglecting the effects of oscillatory loads caused by fluid-structure interaction can yield to the catastrophic failure of designed systems. Tacoma Narrows Bridge (1940) is one of the most infamous examples of large-scale failure.

Computer simulations are often used to calculate the response of a system for a multi-physics and nonlinear fluid-structure problem. There are two main approaches available for developing simulation tools for these coupled FSI problems [87]: 1) Partitioned approach and 2) Monolithic approach.

In a **partitioned** scheme, the fluid and the structure equations are alternatively integrated in time and the interface conditions are enforced. Typically, partitioned methods are based on the following sequential process:

1. Transfer the location and velocity of the structure to the fluid domain
2. Update the fluid mesh
3. Solve the fluid's governing equation and calculate the new pressure field
4. Apply a pressure load on the structure
5. Advance the structural system in time under the fluid-induced load

This sequential process allows for software modularity. Partitioned schemes require only one fluid and structure solution per time step, which can be considered as a single fluidstructure iteration.

In the **monolithic** approach, the equations governing the flow and the displacement of the structure are solved simultaneously with a single solver. The monolithic approach requires a code developed for this particular combination of physical problems, whereas the partitioned approach preserves software modularity because an existing flow solver and structural solver are coupled. Moreover, the partitioned approach facilitates the solution of the flow equations and the structural equations with different, possibly more efficient techniques, which have been developed specifically for either flow equations or structural equations. In this research, we are following the partitioned approach to the FSI problem. In this chapter, we will couple the IB solver developed in Chapter 3 for solving the NS equations with an external finite element code to address the multiphysics problem.

The FSI solution procedure is also classified based on the level of coupling between the two disciplines [88]. In the 1-way, or weak coupling, the pressure loads are transferred to the structure causing the solid domain to deform. However, the structural domain does not affect the fluid's mesh and the solid domain deformations are not mapped back to the fluid domain. In this approach, each discipline is solved a single time to calculate the response. On the other hand, in the 2-way, or strong coupling, the solution of the coupled system is done in an iterative manner. The solution procedure starts with solving the fluid's governing equations. The pressure distribution at the fluid-structure boundary is then mapped to the solid domain to calculate the displacement of the structure. The deformation of the structure results in updating the fluid mesh. This is done until the solution is converged or the process is stopped manually. By using the IB method, the mesh modification step of strong coupling is removed in this work. As described in Chapter 3, by removing the mesh deformation step, we get a more robust simulation and decrease the computational expense of the coupled multiphysics analysis at the same time.

### 5.1.1 Governing Equations

The coupled motion of the fluid and solid domains are governed by a set of governing equations. The Navier-Stokes and continuity equations govern the fluids motion as shown in Equation (5.1) and the solid deformation is governed by a set of elastic equations as shown in Equation (5.2).

$$\rho^f \frac{\partial \mathbf{u}^f}{\partial t} + \rho^f \mathbf{u}^f \cdot \nabla \mathbf{u}^f = \nabla \cdot \boldsymbol{\sigma}^f + \rho^f \mathbf{f}^f \quad : \text{Conservation of momentum} \quad (5.1a)$$

$$\nabla \cdot \mathbf{u}^f = 0 \quad : \text{Conservation of mass} \quad (5.1b)$$

$$\boldsymbol{\sigma}^f = \mu \left[ \nabla \mathbf{u}^f + (\nabla \mathbf{u}^f)^T \right] - p^f \mathbf{I} \quad : \text{Stress formula} \quad (5.1c)$$

$$\rho^s \dot{\mathbf{u}}^s = \nabla \cdot \boldsymbol{\sigma}^s + \mathbf{f}^s \quad : \text{Equation of motion} \quad (5.2a)$$

$$\boldsymbol{\epsilon}^s = \frac{1}{2} \left[ \nabla \mathbf{d}^s + (\nabla \mathbf{d}^s)^T \right] \quad : \text{Strain-displacement equation} \quad (5.2b)$$

$$\boldsymbol{\sigma}^s = \mathbf{C} : \boldsymbol{\epsilon}^s \quad : \text{Constitutive equation} \quad (5.2c)$$

In the above equations, superscript ‘*f*’ and ‘*s*’ correspond to the fluid and solid properties, respectively. In Equation (5.1)  $\rho^f$ ,  $\mathbf{u}^f$ ,  $p^f$ , and  $\mathbf{f}^f$  correspond to the fluid density, velocity, pressure, and body forces, respectively. It should be noted that the immersed boundary forces are applied through the body force term  $\mathbf{f}^f$ . In Equation (5.2)  $\rho^s$ ,  $\mathbf{u}^s$ ,  $\mathbf{f}^s$ ,  $\mathbf{d}^s$ , and  $\mathbf{C}$  correspond to the solid density, velocity, body force, displacement, and stiffness tensor, respectively. We chose  $d$  to represent the displacement so that it won’t be confused with the velocity term  $u$ . This is required when we are defining the IB conditions over the boundary. It should be noted that  $\mathbf{C} : \boldsymbol{\epsilon}^s$  defined the inner product of two second order tensors and is equal to  $\mathbf{C}_{ij} \epsilon_{ij}^s$ . In this chapter, we assume that the body force term in the solid’s equation,  $\mathbf{f}^s$ , is equal to zero. The fluid’s body force term is calculated based on the virtual boundary

method as described in Chapter 3.

In order to couple the fluid and solid equations of (5.1) and (5.2), we are imposing a set of kinematic and dynamic constraints [89] at the intersection of the two mediums as defined in Equation (5.3).

$$\mathbf{u}^s - \mathbf{u}^f = 0 \quad : \text{Kinematic constraint} \quad (5.3a)$$

$$\sigma^s \cdot \mathbf{n} - \sigma^f \cdot \mathbf{n} = 0 \quad : \text{Dynamic constraint} \quad (5.3b)$$

The kinematic constraint will result in zero relative velocity between the fluid and solid domain; whereas, the dynamic constraint will lead to the transfer of loads between the two physical mediums.

### 5.1.2 Multidisciplinary Coupling

In Chapter 3, we utilized the Regularized Delta (RD) function to transfer the velocity information from the Eulerian nodes to the Lagrangian nodes to calculate the force terms needed for the IB method. The same idea is used here to calculate the pressure loads acting on the solid domain. As shown in Figure 5.1, by solving the NS equations, the magnitude of the pressure field at each fluid (Eulerian) node ( $x_i$ ) is known.

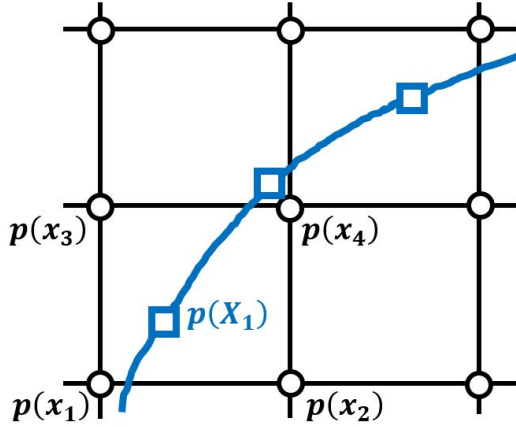


Figure 5.1: Eulerian (○) and Lagrangian (□) nodes for pressure values near and on the immersed boundary.

To map this pressure information from the Eulerian nodes,  $x_i$ , to the Lagrangian node,  $X$ , we convolute the pressure field calculated from the CFD simulation with RD function of Equation (5.4a). By this approach, we have calculated the pressure load on the structure. This is shown in Equation (5.4b)

$$\mathcal{D}(x, X) = \frac{-\tanh^2\left(\frac{x - X}{\eta}\right) + 1}{2\eta} \quad (5.4a)$$

$$p(X, Y) = \int \int p(x, y) \mathcal{D}(x, X) \mathcal{D}(y, Y) dx dy \quad (5.4b)$$

By applying this pressure distribution on the solid domain and solving the equation of motion, we can calculate the displacement and the resulting velocity of the solid structure. The structure's new location is used to update the RD function used for data transfer between the Eulerian and Lagrangian nodes. The cost of updating the RD functions for IB method is minuscule compared to the effort required to update the mesh in body conformal discretization approaches. The velocity of the solid domain is used for calculating the force terms required by the IB method as shown in Equation (5.5).

$$\mathbf{f}(\mathbf{X}, t) = \alpha \int_0^t [\mathbf{u}(\mathbf{X}, \tau) - \mathbf{V}(\mathbf{X}, \tau)] d\tau + \beta [\mathbf{u}(\mathbf{X}, \tau) - \mathbf{V}(\mathbf{X}, \tau)] \quad (5.5)$$

As described in Chapter 4,  $\mathbf{u}(\mathbf{X}, \tau)$  is the fluid velocity calculated at the Lagrangian point  $\mathbf{X}$  at time  $\tau$  and  $\mathbf{V}(\mathbf{X}, \tau)$  is the velocity of the solid structure at the same location and time. The later is calculated after solving the structure's equation of motion. This loop is continued until a convergence is met or the process is stopped manually. The flowchart for the fluid-solid interaction using the IB method is shown in Figure 5.2.

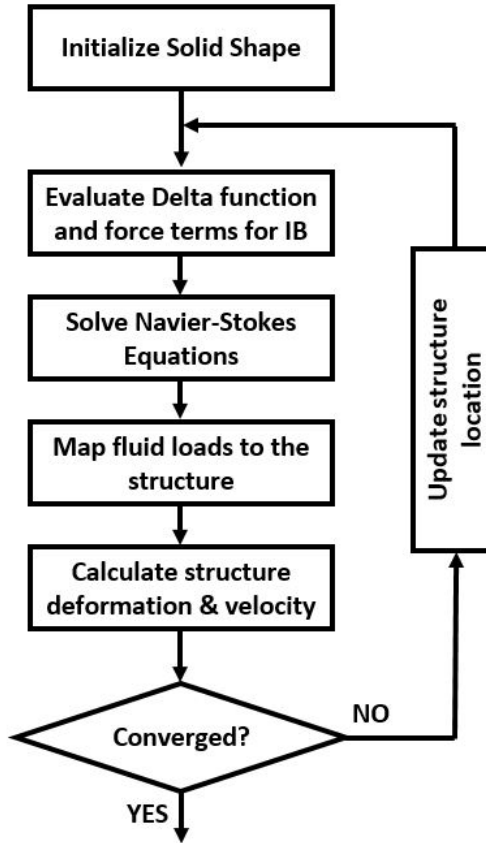


Figure 5.2: Fluid-solid interaction analysis using IB method flow chart.

## 5.2 Multidisciplinary Shape Sensitivity Analysis

The shape sensitivity analysis for the coupled multidisciplinary problem is built on the work done in Chapter 4. However, in this chapter, we are also including the shape sensitivity effects on the structural side. To do so, we differentiate Equations (5.1) and (5.2) alongside the kinematic and dynamic constraints of Equation (5.3) with respect to shape

design variable,  $b$ . The sensitivity equations for the fluid and solid domains are shown in Equation (5.6) and (5.7), respectively.

$$\rho^f \frac{\partial}{\partial t} \left( \frac{\partial \mathbf{u}^f}{\partial b} \right) + \rho^f \frac{\partial \mathbf{u}^f}{\partial b} \cdot \nabla \mathbf{u}^f + \rho^f \mathbf{u}^f \cdot \nabla \left( \frac{\partial \mathbf{u}^f}{\partial b} \right) = \nabla \cdot \left( \frac{\partial \sigma^f}{\partial b} \right) + \rho^f \frac{\partial \mathbf{f}^f}{\partial b} \quad (5.6a)$$

$$\nabla \cdot \left( \frac{\partial \mathbf{u}^f}{\partial b} \right) = 0 \quad (5.6b)$$

$$\frac{\partial \sigma^f}{\partial b} = \mu \left[ \nabla \left( \frac{\partial \mathbf{u}^f}{\partial b} \right) + \nabla \left( \frac{\partial \mathbf{u}^f}{\partial b} \right)^T \right] - \frac{\partial p^f}{\partial b} \mathbf{I} \quad (5.6c)$$

$$\rho^s \frac{\partial \dot{\mathbf{u}}^s}{\partial b} = \nabla \cdot \left( \frac{\partial \sigma^s}{\partial b} \right) + \frac{\partial \mathbf{f}^s}{\partial b} \quad (5.7a)$$

$$\frac{\partial \epsilon^s}{\partial b} = \frac{1}{2} \left[ \nabla \frac{\partial \mathbf{d}^s}{\partial b} + \nabla \left( \frac{\partial \mathbf{d}^s}{\partial b} \right)^T \right] \quad (5.7b)$$

$$\frac{\partial \sigma^s}{\partial b} = \frac{\partial \mathbf{C}}{\partial b} : \epsilon^s + \mathbf{C} : \frac{\partial \epsilon^s}{\partial b} \quad (5.7c)$$

$$\frac{\partial \mathbf{u}^s}{\partial b} - \frac{\partial \mathbf{u}^f}{\partial b} = 0 \quad (5.8a)$$

$$\frac{\partial \sigma^s}{\partial b} \cdot \mathbf{n} - \frac{\partial \sigma^f}{\partial b} \cdot \mathbf{n} = 0 \quad (5.8b)$$

As shown in Equations (5.6) and (5.7), to solve the sensitivity equations we need to obtain the solution of the governing equation ( $\mathbf{u}^f$ ,  $\epsilon^s$ ). Therefore, we are proposing to use the flowchart of Figure 5.3 for the coupled multidisciplinary sensitivity analysis. The sensitivity calculation process starts by solving the Navier-Stokes equation and mapping the pressure to the structural domain to calculate the deformation in the structural domain. The solution of the Navier-Stokes and Elasticity equations are then fed to the sensitivity solver to calculate the sensitivity response. This loop is continued until a convergence for the

governing equations is reached or the process is stopped manually.

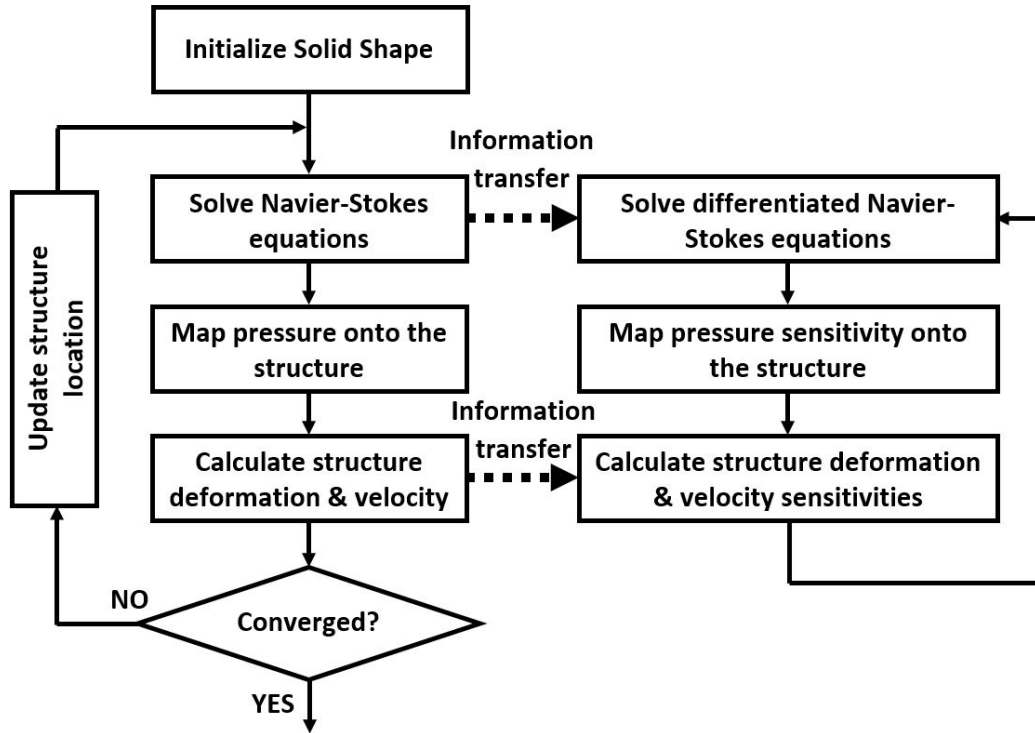


Figure 5.3: Coupled multidisciplinary sensitivity analysis flowchart.

## 5.3 Demonstration Cases

### 5.3.1 Vortex Induced Vibration

Vortex Induced Vibrations (VIV) are motions of solid structures immersed in fluid that are caused by the irregularities in the flow. VIV of structures are of practical interest to many fields of engineering. For example, they can cause vibration and noise in heat exchanger tubes or an aircraft wing. In this demonstration problem, we are interested in the forced oscillations of an elastically mounted, rigid cylinder for different values of the Reynolds number. The physical problem is shown in Figure 5.4. The boundary conditions are selected as constant velocity at inlet, free slip boundary conditions on top and bottom walls, and outflow boundary condition at the outlet.

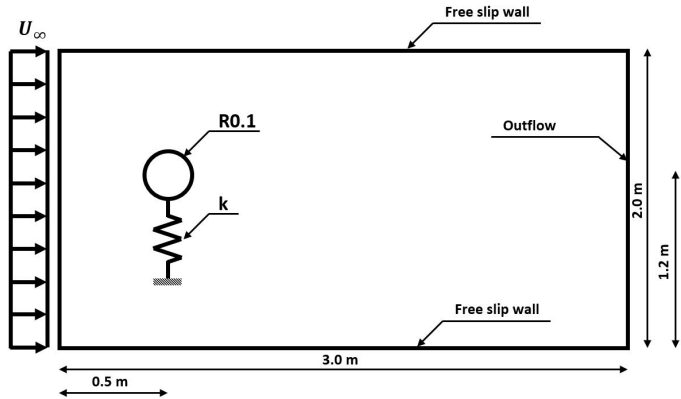


Figure 5.4: Physical domain for the vortex induced vibration problem.

The rigid cylinder has the radius  $R$  and is mounted on an elastic structure with stiffness  $k$ . The free stream velocity is selected as  $U_\infty$ . To verify the solver and FSI coupling, we are going to calculate the shedding frequency of the cylinder first. Vortex shedding is an oscillating flow that takes place when fluid passes a bluff body at certain velocities. The vortices that are generated on the aft of the body start to detach periodically from either side of the body. The frequency at which the vortex shedding takes place is described using the dimensionless Strouhal number. The Strouhal number is defined as shown in Equation (5.9).

$$St = \frac{fL}{U} \quad (5.9)$$

where  $f$  is the frequency of the vortex shedding;  $L$  is the characteristic length; and  $U$  is the flow velocity. The Strouhal number of a stationary circular cylinder is a function of Reynolds number [90] as shown in Figure 5.5[91].

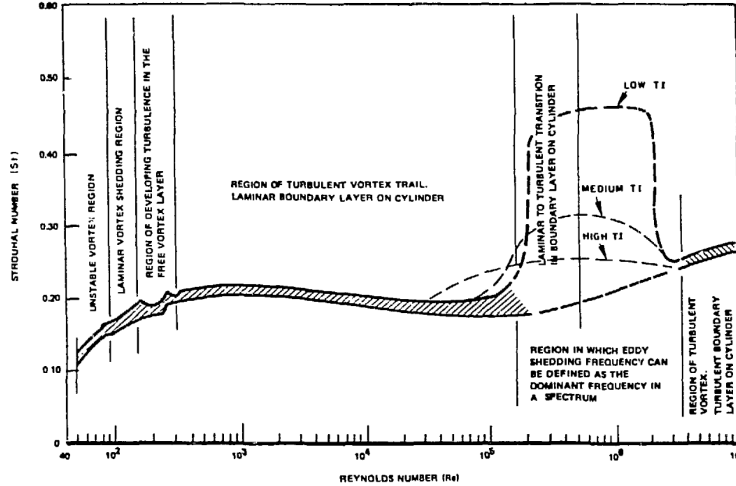


Figure 5.5: Strouhal number for a single cylinder.

To verify the simulation code developed for the IB simulation, we verified the shedding frequency of the circular cylinder in the cross-flow. The domain length and height are selected as  $3m$  and  $2m$ , respectively, as shown in Figure 5.4. The cylinder radius is selected as  $0.1m$  and is located  $0.5m$  from the left wall and  $1.2m$  from the bottom wall. The asymmetric shape of the computational domain helps the shedding initiation. The domain is discretized using 3000 cells in the  $x$  direction and 2000 in the  $y$ . The cylinder is defined using 50 Lagrangian nodes. The  $p$  value in the delta function definition is selected as 0.5. It should be noted that to verify the shedding frequency the cylinder is fixed in its place. We compared the Strouhal number calculated from the IB code with the results [92] for two different Reynolds numbers. The shedding frequency is calculated by saving the time history of drag force on the cylinder and performing frequency analysis on this data. We used the power spectral density function to look at the most dominant frequencies. The comparison between these results is shown in Table 5.1.

Reynolds number	St (current IB)	St (Literature [91] and [92])
100	0.171	0.168
500	0.194	0.200

Table 5.1: Comparison of the shedding frequency using IB method and literature.

The effect of the number of Lagrangian points on the shedding frequency is shown

in Figure 5.6. As shown here, the number of Lagrangian points does not affect the vortex shedding frequency.

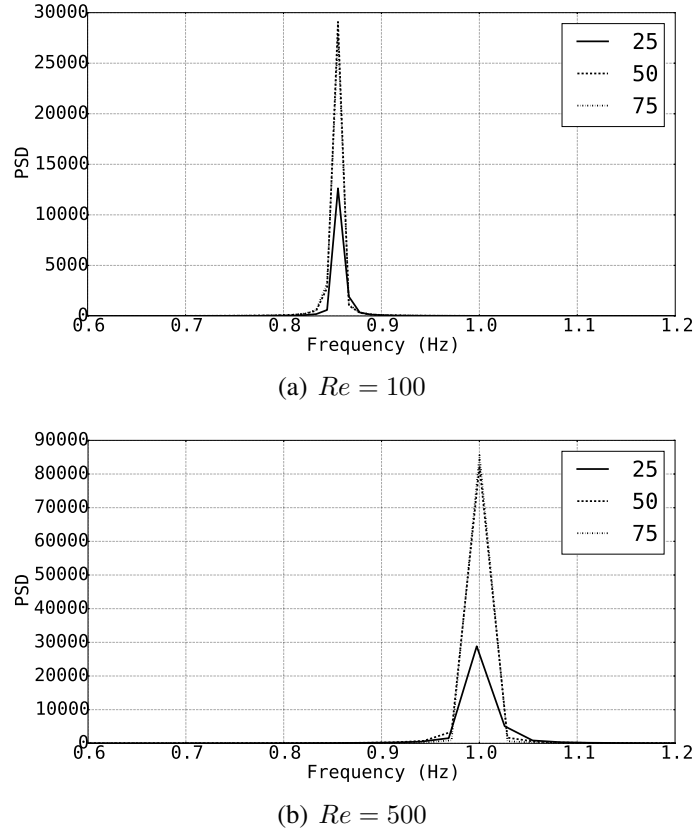


Figure 5.6: Number of Lagrangian points effect on the shedding frequency.

After verifying the shedding frequency of IB solver, we attach the elastic structure to the cylinder and let the system vibrate due to aerodynamic loads. The equation of motion for this cylinder is shown in Equation (5.10).

$$m\ddot{y} + ky = f(y, \dot{y}, t; R) \quad (5.10)$$

where  $y$  is the cylinder location;  $m$  is the cylinder mass;  $k$  is elastic structure stiffness; and  $f(y, \dot{y}, t; R)$  is the aerodynamic load. It should be noted that the load is an explicit function of cylinder location, velocity, and time, while an implicit function of cylinder radius. This requires an unsteady treatment of the FSI problem by coupling Equations (5.1) and (5.10).

At each time step, the NS equations are solved and the pressure values at the Lagrangian nodes are calculated using the regularized Delta function. These pressure values are then integrated over the cylinder surface to calculate the force value on the right-hand-side of Equation (5.10). To solve for the structure displacement and velocity, Equation (5.10) is written in the state-space form as shown in Equation (5.11). This equation is then integrated in time alongside the NS equations using Adams-bashforth method. The initial condition for the structure is selected as zero displacement and velocity at  $t = 0$ .

$$\begin{bmatrix} \dot{y} \\ \ddot{y} \end{bmatrix} = \begin{bmatrix} 0 & 1 \\ -\frac{k}{m} & 0 \end{bmatrix} \begin{bmatrix} y \\ \dot{y} \end{bmatrix} + \begin{bmatrix} 0 \\ f(y, \dot{y}, t; R) \end{bmatrix} \quad (5.11)$$

where the load,  $f(y, \dot{y}, t; R)$ , is calculated as shown in Equation (5.12).

$$f = \oint \left( \int \int p(x, y) \mathcal{D}(x - X_s) \mathcal{D}(y - Y_s) dx dy \right) ds \quad (5.12)$$

In Equation (5.12),  $p(x, y)$  is the pressure calculated from the CFD solution;  $\mathcal{D}$  is the regularized delta function; and  $ds$  represents the infinitesimal element on the cylinder surface.

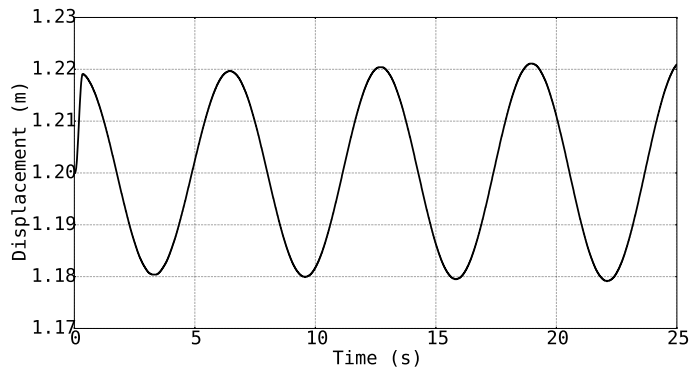
For the coupled FSI sensitivity analysis, we considered the vortex induced vibration of the cylinder at two different Reynolds numbers. The sensitivity of the displacement to the radius of the cylinder is calculated and verified with the complex step results. The sensitivity equation for the fluid domain is derived in Chapter 4, by solving it, we have the sensitivity of pressure field on the surface of the cylinder. The sensitivity equation for the structure is derived by differentiating Equation (5.11) as shown in Equation (5.13).

$$\begin{bmatrix} \dot{y}' \\ \ddot{y}' \end{bmatrix} = \begin{bmatrix} 0 & 1 \\ -\frac{k}{m} & 0 \end{bmatrix} \begin{bmatrix} y' \\ \dot{y}' \end{bmatrix} + \begin{bmatrix} 0 \\ f'(y, \dot{y}, t; R) \end{bmatrix} \quad (5.13)$$

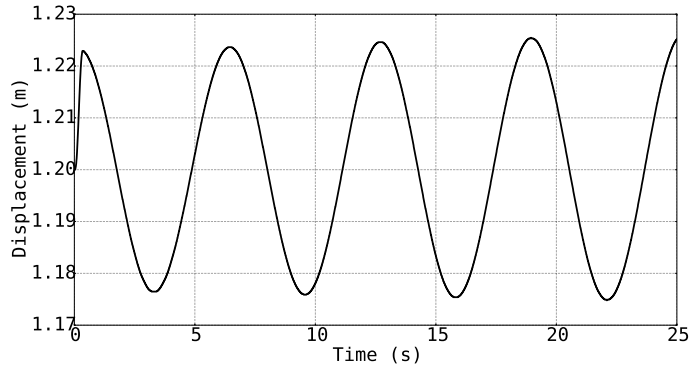
here,  $(\cdot)'$ , represents the derivative with respect to the design variable. It can be seen that the

same solver used for solving Equation (5.11) is utilized for solving Equation (5.13). The only difference between the two systems is the load used for evaluating the right-hand-side of Equation (5.13).

For this problem, the stiffness of the elastic structure,  $k$ , is selected as 1 N/m and the cylinder mass is chosen as 1 kg. The time history of cylinder displacement in the first 25 seconds of its motion is shown in Figure 5.7. The cylinder starts from the initial position at  $y = 1.2$ , and after a short transient region, starts oscillating at an almost constant amplitude as shown in Figure 5.7.



(a)  $Re = 100$



(b)  $Re = 500$

Figure 5.7: Time history of cylinder center displacement.

Figure 5.8 shows the u-velocity contour around the elastically mounted cylinder at different times. As can be seen, the vortex shedding is dominant at  $t = 5$ , but it started before  $t = 5$  and causes the cylinder to oscillate.

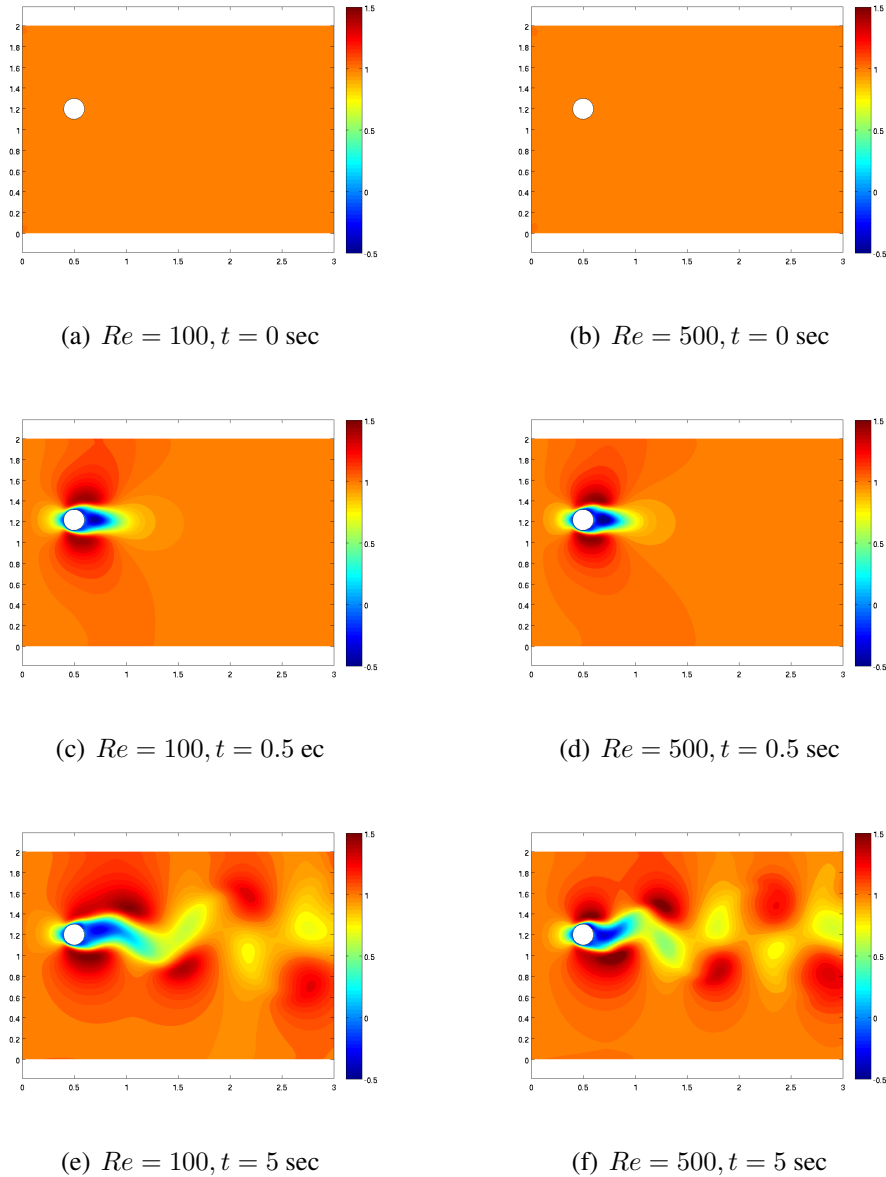


Figure 5.8: Unsteady u-velocity contours for flow around cylinder at  $Re = 100$  and  $Re = 500$ .

The time history of the sensitivity results are shown and verified with the complex step solution in Figure 5.9. As shown here, at  $t = 0$ , the sensitivity of displacement with respect to radius is zero since the initial location of cylinder is independent of its shape. However, the value of cylinder displacement will start oscillating between positive and negative numbers as the time progresses. This is what we are expecting since by increasing

the radius, the loads on the cylinder will increase. This will result in an increase in the amplitude at both ends of the oscillation period.

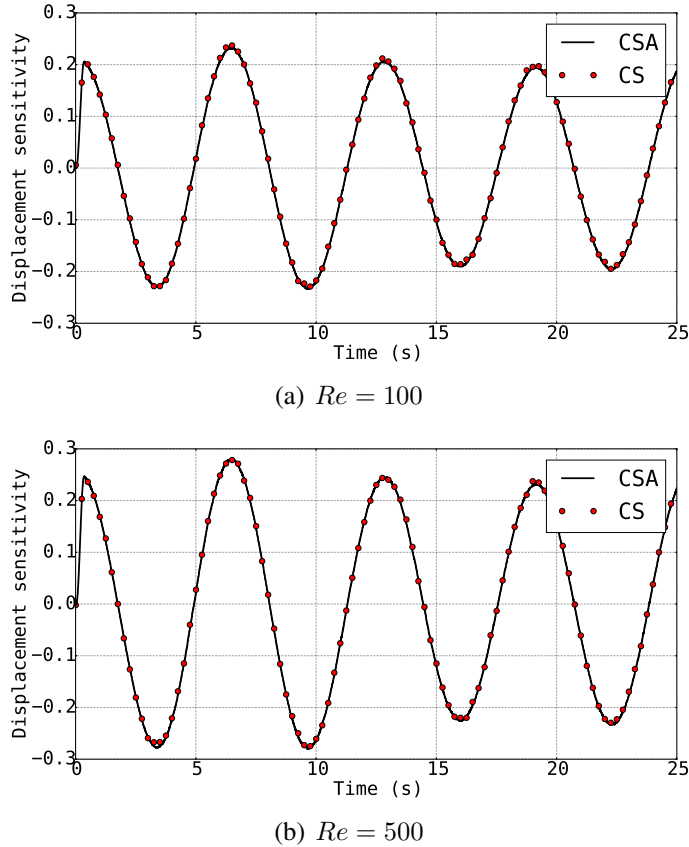


Figure 5.9: Time history of cylinder center displacement sensitivity.

Figure 5.10 shows the u-velocity sensitivity contour around the elastically mounted cylinder at different times. As shown in the sensitivity contours, the change in the cylinder radius mainly affects the downstream flow. This is expected for a convective flow where information from the cylinder cannot move upstream. The small region with negative sensitivity near the surface is due to the reduction of velocity due to boundary layer expansion as the radius increases and has physical meaning.

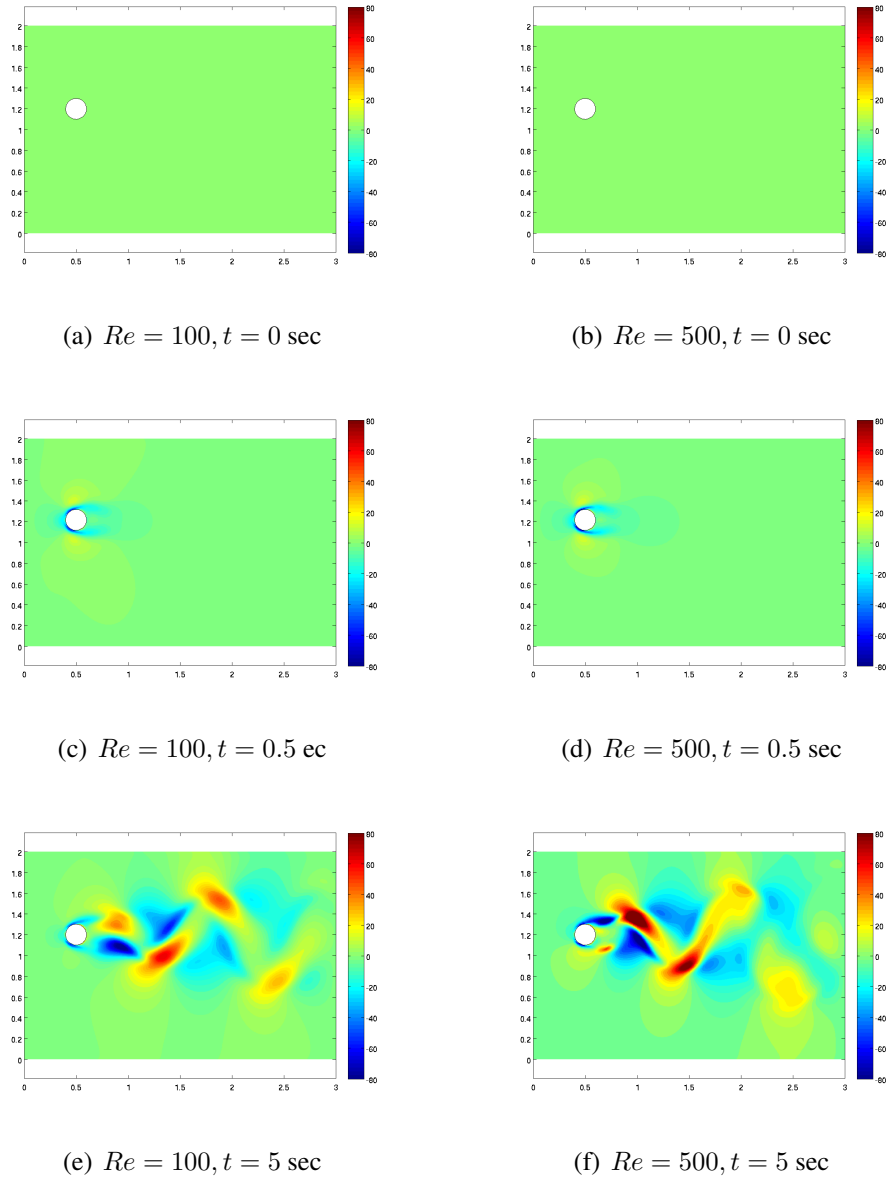


Figure 5.10: Unsteady u-velocity contours for flow around cylinder at  $Re = 100$  and  $Re = 500$ .

### 5.3.2 Pitch and Plunge Airfoil Motion

Understanding the unsteady aerodynamic characteristics of a pitching and plunging airfoil has two major engineering applications. First, it can be used to predict the dynamic stall of aerodynamic bodies such as aircraft in a demanding maneuver [93]. Dynamic stall is

often seen in aerodynamic surfaces going through a pitching moment or oscillatory behavior. This phenomenon is caused due to instability and separation of the leading-edge vortex which results in a dramatic decrease in lift and sudden increase in pitching moment. Dynamic stall can lead to high amplitude vibrations and high loads that can cause fatigue and structural failure of the aerodynamic surfaces. The second motivation of investigating this unsteady aerodynamic behavior is the application of flapping wings for swimming and flying animals [94]. The vast majority of research on the pitching and plunging airfoil is done by forcing the motion on the airfoil and looking at the aerodynamic response. This is mainly done for investigating the thrust and the parameters that control it [95, 96]. Webb, et al. investigated the use of IB method for the forced pitching and plunging movement of the SD7003 airfoil and verified their solution with experimental results [97]. In this work, we are interested in the free oscillations of the airfoil due to aerodynamic loads. Moreover, we will investigate sensitivity of the airfoil displacement to its shape.

To have an analytical representation of the airfoil shape, we used the Joukowsky transform to define the geometry. Joukowsky transform is a conformal mapping that maps a circle in the complex plane to a shape that represents a typical airfoil shape. The Joukowsky transform is shown in Equation (5.14).

$$z = \zeta + \frac{1}{\zeta} \quad , \quad \zeta = x + iy \quad (5.14)$$

As shown in Figure 5.11, the center location of the original circle defines the thickness and camber of the airfoil. For the sensitivity analysis, we are interested in the sensitivity of flow to the chamber; therefore, it is required to differentiate with the  $y$  coordinate of circle center. This is calculated analytically.

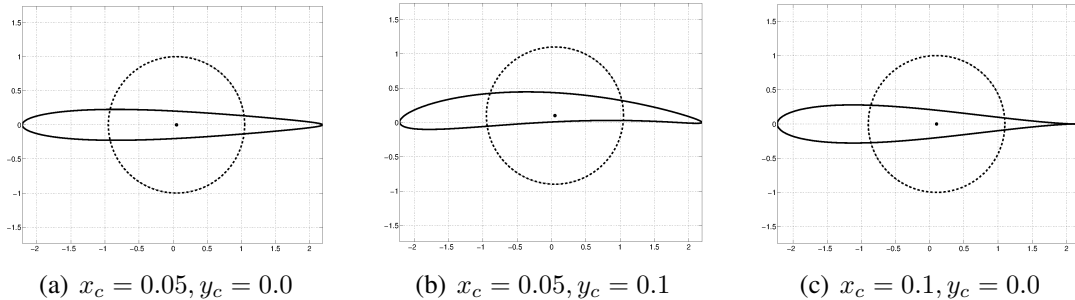


Figure 5.11: Effect of circle location on Joukowsky airfoil shape.

The computational domain for this problem is defined as shown in Figure 5.12(a). The rigid airfoil is mounted on a two degree-of-freedom elastic structure as shown in Figure 5.12(b). The elastic structure contains axial and torsional springs to represent an actual wing more accurately.

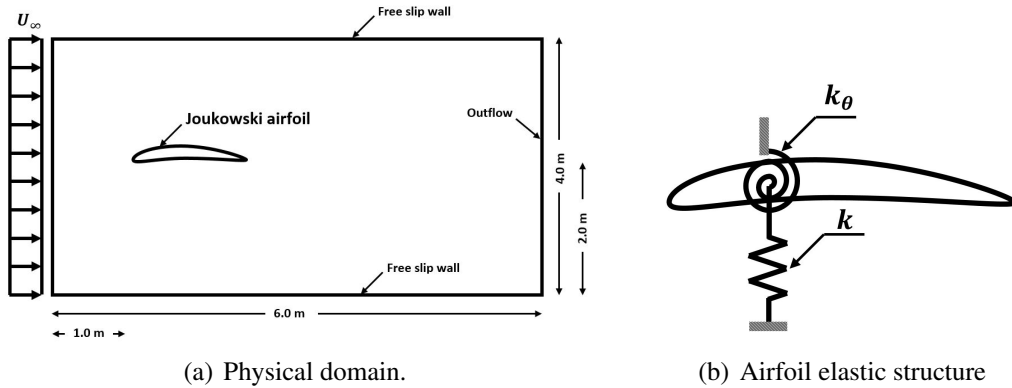


Figure 5.12: Physical domain and elastic structure for the pitching and plunging airfoil.

The governing equations for the elastic structure in the state-space form are shown in Equation (5.15).

$$\begin{bmatrix} \dot{y} \\ \ddot{y} \\ \dot{\theta} \\ \ddot{\theta} \end{bmatrix} = \begin{bmatrix} 0 & 1 & 0 & 0 \\ -\frac{k}{m} & 0 & 0 & 0 \\ 0 & 0 & 0 & 1 \\ 0 & 0 & -\frac{k_\theta}{I} & 0 \end{bmatrix} \begin{bmatrix} y \\ \dot{y} \\ \theta \\ \dot{\theta} \end{bmatrix} + \begin{bmatrix} 0 \\ F(y, \dot{y}, t) \\ 0 \\ M(\theta, \dot{\theta}, t) \end{bmatrix} \quad (5.15)$$

where  $m$  is airfoil mass;  $k$  is axial spring stiffness;  $I$  is airfoil moment of inertia around its quarter-chord;  $k_\theta$  is rotational spring stiffness;  $F$  is the force in  $y$  direction (lift generated by airfoil); and  $M$  is the moment at quarter-chord. The force and moment are calculated using the pressure field from the solution of NS equations. Adams-bashforth method is used to explicitly integrate Equation (5.15) in time.

For this problem, we look at two different airfoils mounted on the elastic structure as shown in Figure 5.13. The difference in airfoil shape will result in different characteristics in the FSI response of the system. We refer to the airfoil defined in Figure 5.22(a) as *thin airfoil* and the one in Figure 5.22(b) as *thick airfoil*.

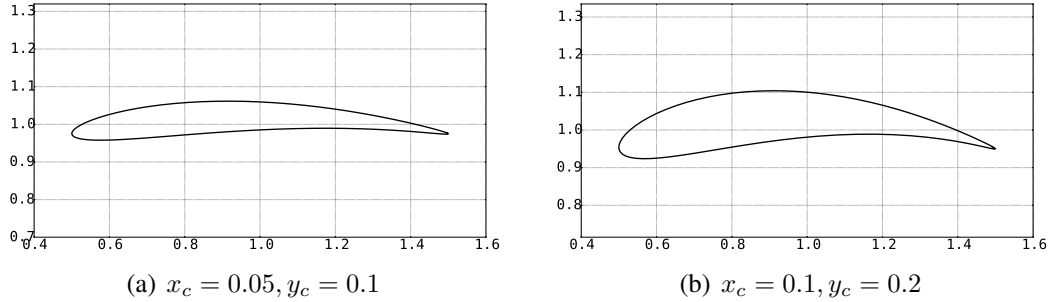
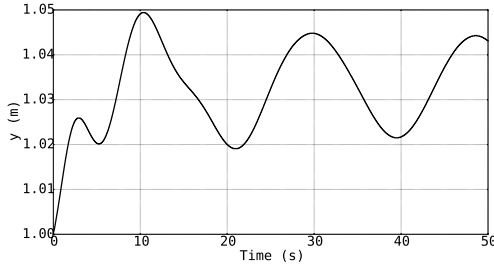
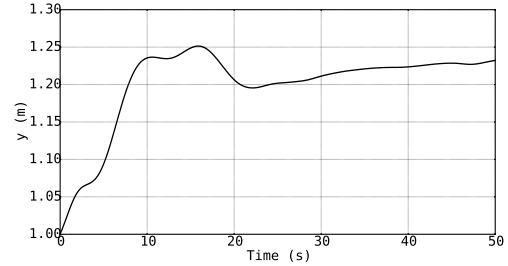


Figure 5.13: Airfoil shape used for FSI calculation.

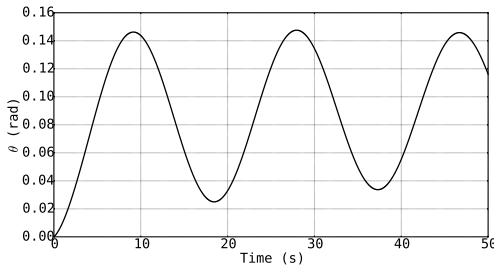
The Reynolds number for this simulation is selected as 100. At higher Reynolds number will result in turbulent flow which is not the subject of this research. For the elastic structure properties, spring stiffness is selected as  $0.5N/m$ , airfoil mass as  $1.0Kg$ , rotational spring as  $0.1N/\theta$ , and the moment of inertia as  $1.0Kg \cdot m^2$ . The results of the first 50-second simulation of the airfoil center location and change in the angle of attack due to aerodynamic loads are shown in Figure 5.14. As shown here, the thin airfoil of Figure 5.22(a) follows an oscillatory response whereas the thick airfoil of Figure 5.22(b) experiences divergence.



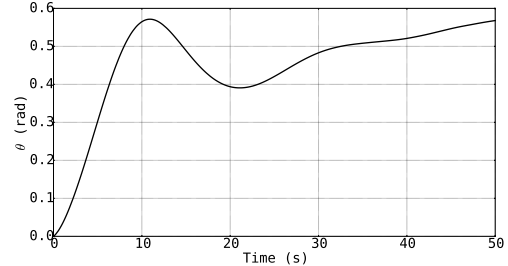
(a) Thin airfoil displacement



(b) Thick airfoil displacement



(c) Thin airfoil rotation



(d) Thick airfoil rotation

Figure 5.14: Airfoil displacement and rotation results due to aerodynamic loads.

To better understand the solution history, three snapshots from the u-velocity contour of the two airfoils are shown in Figure 5.15. As shown here, the thick airfoil goes through large displacement and deformation. This is difficult to capture using the conventional body-conformal method; however, it can be done with rather ease by utilizing the current IB approach.

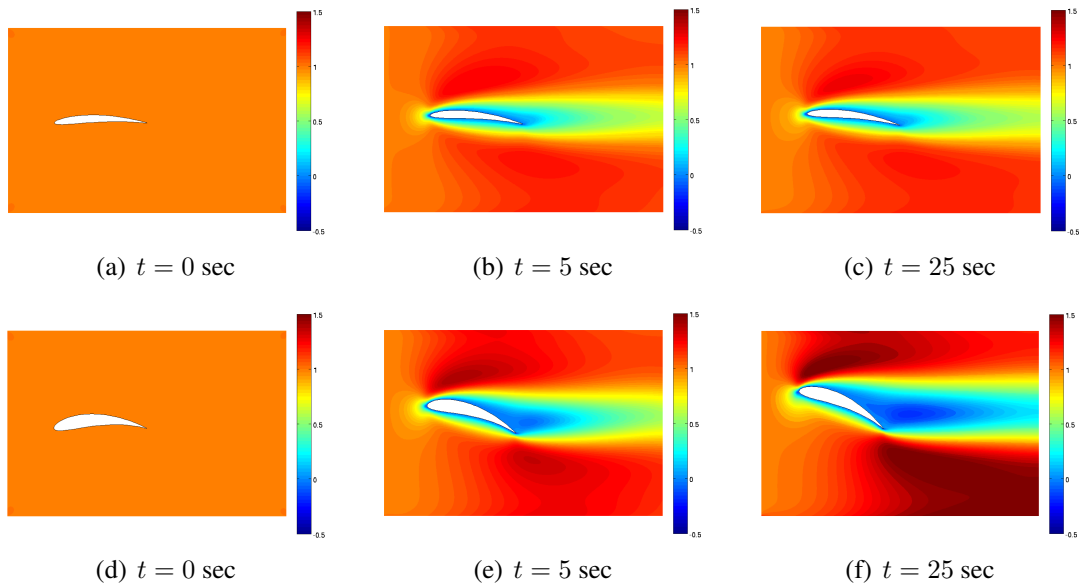


Figure 5.15: U-velocity time snapshots for airfoil on an elastic structure.

For the sensitivity analysis, we investigate the sensitivity of the airfoil displacement and rotation to change in its chamber. As discussed in Chapter 4, as a part of sensitivity calculation, it is required to derive the shape sensitivities. This is done analytically since the Joukowski transform provides us with an analytical definition for the airfoil boundary. The shape sensitivity of the airfoil to camber is calculated by differentiating Equation (5.14) to the  $y$  coordinate of the center of the airfoil. For the structure side, the shape only affects the loads acting on the elastic structure and not its shape. Therefore, we can use the same solver used for calculating the displacement and rotation of the structure for the sensitivity calculation. The time history of the sensitivity results for the displacement and rotation of the two airfoils is shown in Figure 5.16.

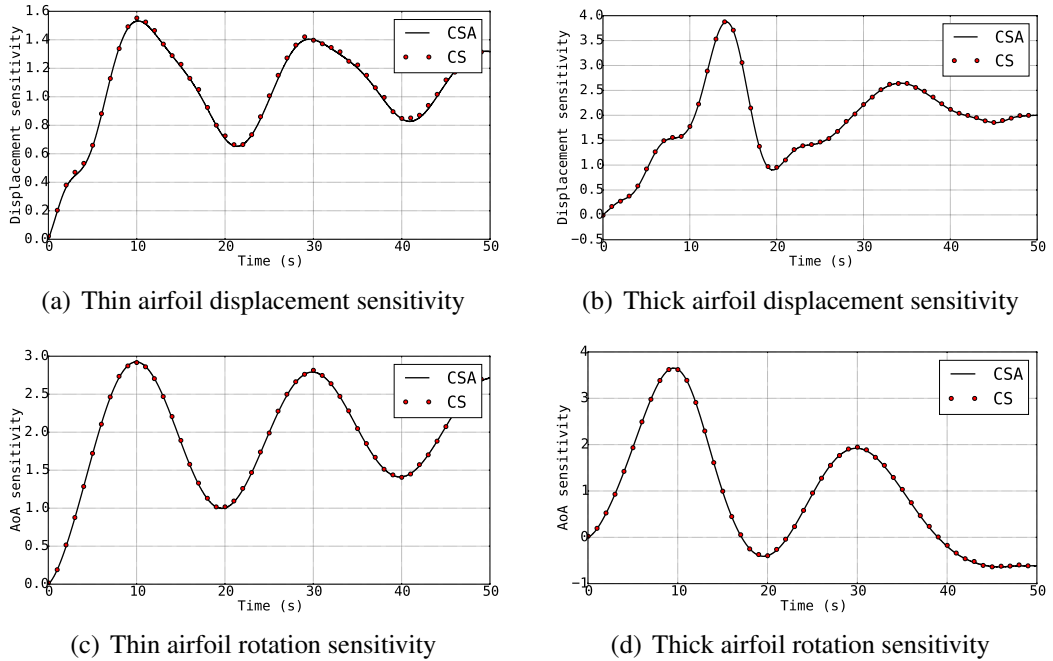


Figure 5.16: Airfoil displacement and rotation sensitivity results due to change in camber.

As shown in Figure 5.16, the sensitivity response flow is the same pattern as the analysis solution for this problem. For the oscillatory response of the thin airfoil, the sensitivity solution also moves between two extremes for both the displacement and airfoil rotation. However, for the thick airfoil that shows a divergence characteristic as shown in Figure 5.14, the sensitivities also reach a constant value. It is interesting to see that for the thick airfoil, by increasing the thickness, the lift will increase and therefore, we see positive sensitivities for the displacement; however, the moment generated around the quarter chord decreases which causes a negative sensitivity for the rotation.

Finally, we looked at the u-velocity sensitivity contours as shown in Figure 5.17 for different snapshots in time. As shown here, the velocity field around the airfoil in both cases contains the most sensitivity near the tip.

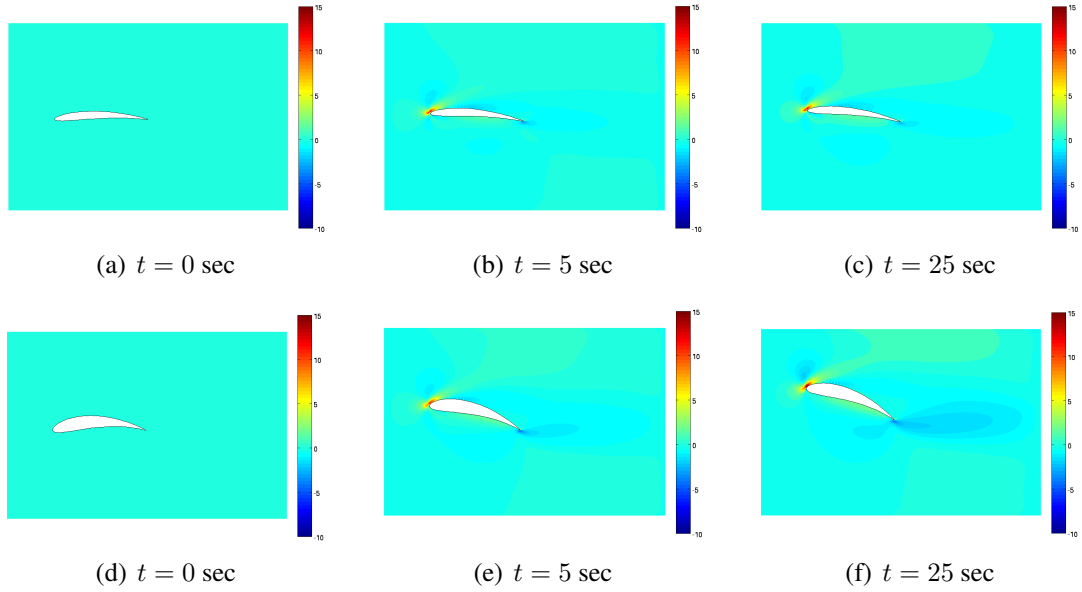


Figure 5.17: U-velocity sensitivity time snapshots for airfoil on an elastic structure.

### 5.3.3 Flapping and Bending of a Monofin

An archetype of fluid-structure interaction is the flapping of a flag pole in a steady wind and the mutual interaction of the pole with its surrounding fluid. This phenomenon is also of interest in various other engineering applications such as locomotion using a monofin [98], sails and understanding the flapping of flexible structures, and possible application of energy harvesting [99] and turbulence reduction [100]. Here we focus on calculating the sensitivity of structure response to the change in its shape since the application of the immersed boundary method for such problems has already been demonstrated in the work of Kim et al. [101]. The physical domain for this problem is shown in Figure 5.18. The boundary conditions are selected as constant velocity at inlet, free slip boundary conditions on top and bottom walls, and outflow boundary condition at the outlet.

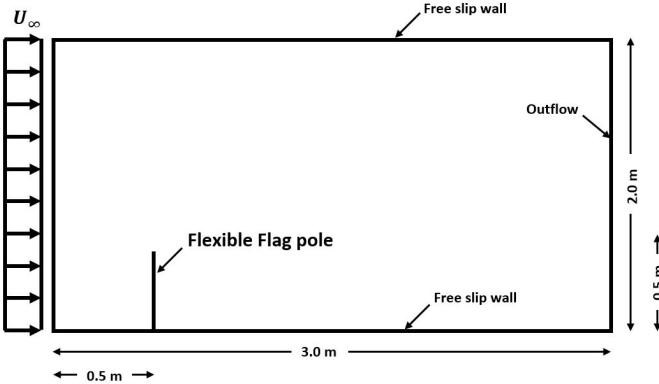


Figure 5.18: Physical domain for the bending monofin.

As the cross-flow starts, the monofin will start vibrating due to aerodynamic loads. Due to the sudden start of the flow, the loading on the structure mimics the same characteristic as step function loading. Hence, we expect the structural response to have similar characteristics. This will provide us with more insight into the dynamic response of the system.

The monofin structure is modeled using Euler-Bernoulli beam theory with three degrees of freedom at each node. The monofin is made of Aluminium with  $E = 68.9 \text{ GPa}$ , and  $\rho = 2.7 \times 10^3 \text{ Kg/m}^3$ . The cross-section is defined as a circle with the diameter of 4mm. Due to the unsteady nature of the problem, the Newmark-beta method is used for explicit time integration of the structural equation of motion. As in previous problems, the pressure load is transferred to the structure using regularized delta function and the effect of location and velocity of the Lagrangian nodes of the structure are reflected through the IB forcing term of Equation (3.21). For this problem, we considered at the unsteady response of two different cases of the monofin, each at a different length. The Reynolds number for this problem is fixed at 100 to make sure that the Laminar flow assumption is met for the simulation. The time history of monofin tip displacement is shown in Figure 5.19. As we increase the length of the beam, the frequency of oscillation decreases. This is true since by increasing the length, the bending stiffness of the structure decreases, which results in a lower frequency of oscillation.

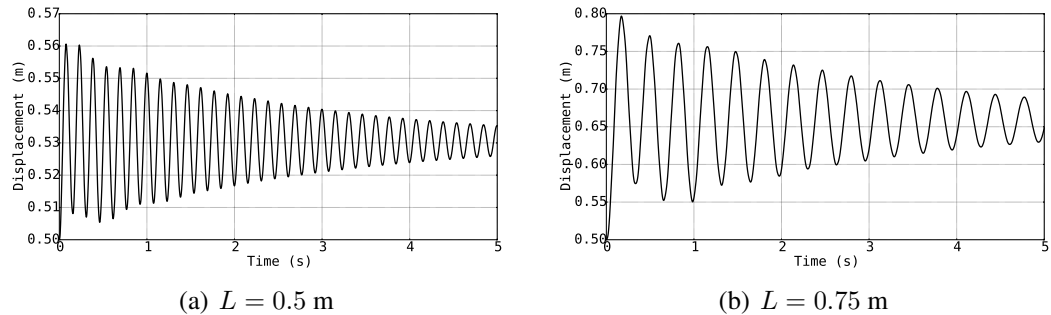


Figure 5.19: Time history of the monofin tip displacement in cross-flow.

Another important aspect of Figure 5.19 is the viscous damping feature of the tip displacement movement. The structural model does not include viscous damping and the effect seen in Figure 5.19 is purely due to the multidisciplinary interaction of fluid and structure for this problem. It is clear that the longer monofin experiences lower damping which is due to lower frequency and therefore, the lower velocity of the structure. This will result in less damping force since the viscous damping is proportional to the velocity of the structure. To better see the flow structure behind the monofin, time snapshots of the u-velocity and pressure contours are shown in Figure 5.20 and 5.21 respectively.

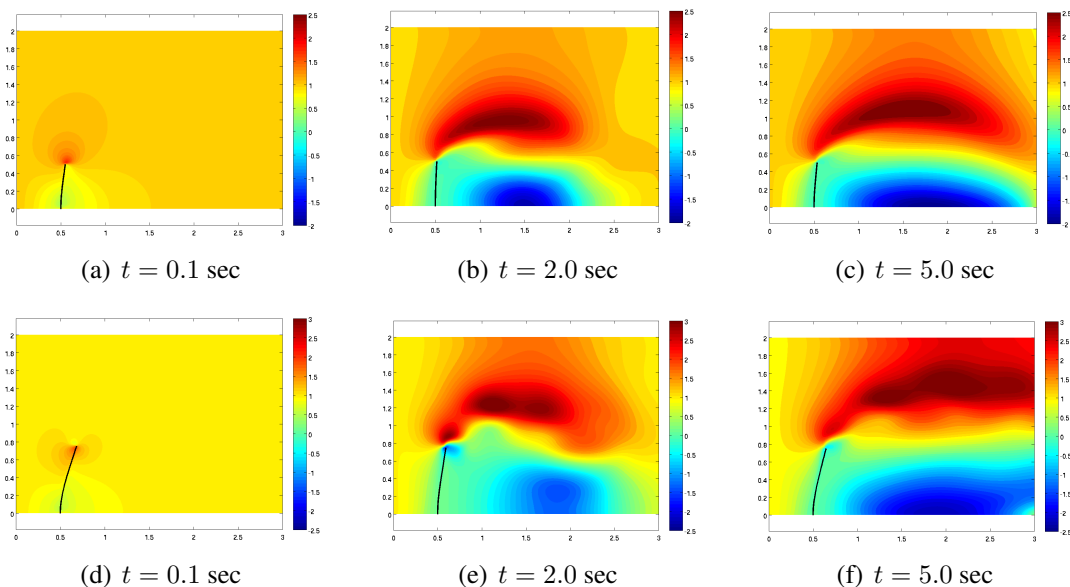


Figure 5.20: U-velocity time snapshots for elastic monofin.

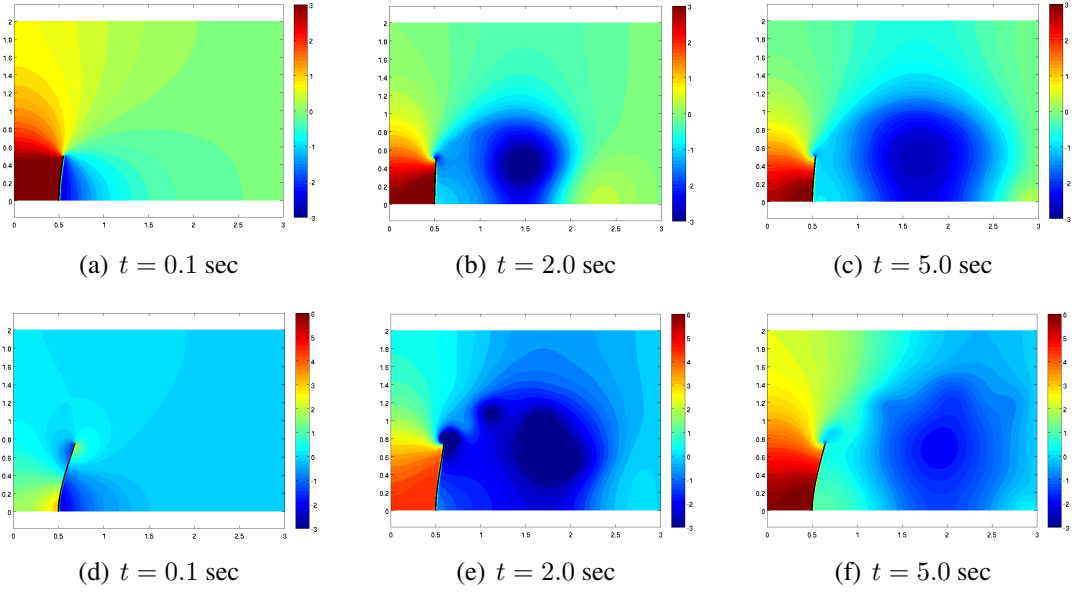


Figure 5.21: Pressure time snapshots for elastic monofin.

We calculate the monofin tip displacement sensitivity to its length, that affects both the fluid and structure domain. Therefore, both of the governing equations need to be differentiated with respect to the length. Differentiation of the Navier-Stokes equations for the fluid is extensively discussed in Chapter 4, here we derive the continuum sensitivity equation for the monofin structure. The governing equation for an Euler-Bernoulli beam is shown in Equation (5.16).

$$\frac{d^2}{dx^2} \left( EI \frac{d^2w}{dx^2} \right) + \rho \frac{d^2w}{dt^2} = q(x) \quad (5.16)$$

where  $w$  is the deflection in  $y$  direction;  $E$  is elastic modulus;  $I$  is the second moment of area of the beam's cross-section;  $\rho$  is mass per length; and  $q(x)$  is the distributed load. The sensitivity equation for the structure is derived by analytically differentiating Equation (5.16) with respect to design variable  $L$  as shown in Equation (5.17).

$$\frac{d^2}{dx^2} \left( EI \frac{d^2w'}{dx^2} \right) + \rho \frac{d^2w'}{dt^2} = q'(x) \quad (5.17)$$

where  $(\cdot)'$  represents the derivative of response with respect to design variable,  $L$ . It should be noted that the right-hand side of Equations (5.16) and (5.17) are solved by solving the Navier-Stokes and differentiated Navier-Stokes equations, respectively. The loads from the fluid domain are transferred to the structure using regularized delta function. The time history of the sensitivity of tip displacement to the length of the monofin is shown in Figure 5.22. As shown here, the sensitivity results from the CSA agrees well with the Complex Step (CS) results.

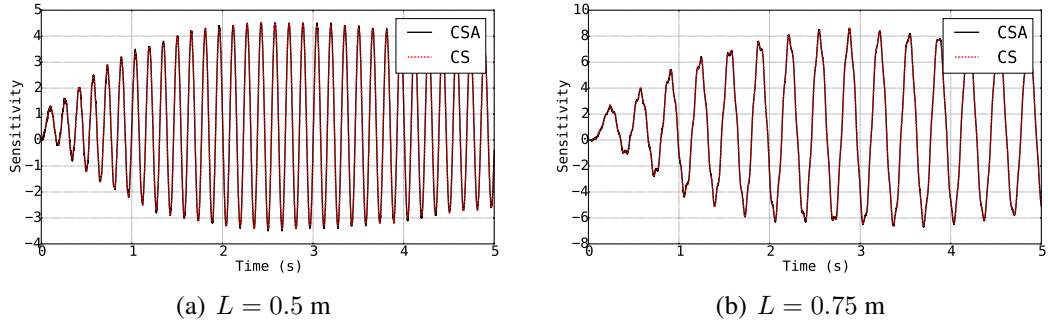


Figure 5.22: Time history of the monofin tip displacement in cross-flow.

## 5.4 Summary

In this chapter, we formulated the sensitivity analysis for coupled fluid-structure interaction problems. Fluid-structure coupling is achieved by transferring the loads from the Eulerian nodes of the fluid domain to the Lagrangian structure nodes by the regularized delta function of Equation (4.6). The effect of solid deformation and velocity is transferred to the fluid domain by the force term in the Navier-Stokes equations as described in Chapter 3. In this chapter, we verified our fluid-structure coupling by looking at the vortex shedding frequency of flow around a circular cylinder at two different Reynolds numbers. We derived the governing sensitivity equation for the coupled problem by differentiating the governing equation for each discipline and also the interface dynamic and kinematic constraints. To solve the sensitivity equations for the structure domain, the load sensitivity is required,

which is calculated by solving the differentiated Navier-Stokes equations. We applied this methodology to various demonstration problems as shown in this chapter. Due to the unsteadiness of these coupled problems, the unsteady sensitivity analysis is conducted and the results are verified using the complex step method. As shown in the results section, the solution of analytical sensitivity analysis agrees well with the complex step results.

# Chapter 6

## Summary Remarks and Future work

This work is motivated by the need for accurate high fidelity sensitivities for the design of coupled fluid-structure interaction systems. Design and analysis of such multiphysics systems are challenging due to several factors such as the coupling algorithms for data transfer between disciplines, mesh deformation, numerical stabilities, and sensitivity calculation. In this work we focused on two aspects of the FSI problems: i) sensitivity analysis and ii) mesh deformation.

The sensitivity analysis is required in different design aspects such as design optimization, function approximation, and reliability analysis. As pointed out in the literature survey in Chapter 1, the analytical methods for sensitivity calculation have several benefits regarding accuracy and cost over the available numerical methods. However, the primary concern of the analytical sensitivity methods is their formulation and implementation. As discussed in Chapter 2, there are two approaches for analytical sensitivity calculation, discrete and continuum approach. In the discrete sensitivity analysis (DSA) the governing equations are first discretized and then differentiated whereas the governing equations are first differentiated and then discretized in the continuum sensitivity analysis. It was shown in Chapter 2 that for the CSA the numerical differential operators derived for solving the governing equations can be reused in the sensitivity calculations; however, this is not pos-

sible for DSA. The capability of reusing the differential operators without modification is very beneficial concerning the implementation of the CSA in commercial packages. The difference between the sensitivity analysis and the solution of the governing equations are through the effect of boundary conditions as was shown in Chapter 2. The ease of implementation for the CSA motivated us to use this technique for sensitivity calculation of the FSI problem.

The state of the art techniques that are used to model the interaction between the fluid and a deformable solid are based on a body conformal mesh for representing the fluid domain and the solid boundaries. However, as pointed out in Chapter 3 the body-conformal methods require the computational domain to be updated as the solid boundaries deform. This is required for both the design optimization where the optimizer changes the shape and the FSI simulation where the boundaries deform due to forces from the fluid domain. The mesh deformation adds to the computational cost of the simulation since a set of governing equations (usually elastic equations) need to be solved to track the location of the computational nodes. Moreover, these techniques can fail when the deformation of the solid domain becomes significant or for complex boundary shapes. To address these issues, we proposed to utilize the Immersed Boundary (IB) method for solving the flow over solid boundaries and also sensitivity analysis. In IB method, the effect of solid boundaries are either added to the governing equation through force terms (continuous IB method) or represented by changing the numerical stencil near the solid boundaries (discrete method). Several different IB methods were investigated in Chapter 3 and their characteristics were analyzed. The continuous IB method was selected since it is more compatible with CSA. However, additional modifications were made to the continuous IB method to make it appropriate for CSA implementation.

As discussed in Chapter 3, in the continuum IB method the effect of solid boundaries are added to the governing equations using force terms. This is either through penalizing the governing Navier-Stokes (NS) equations using the Darcy equation or adding the force

terms based on a feedback function of Equation (3.21). These forces are added to the NS equations using the Heaviside function and delta function respectively. However, these functions are not continuously differentiable and cannot be employed in the CSA formulation. The Regularized Delta (RD) and Regularized Heaviside (RH) functions were introduced in Chapter 4 to address this issue. This is one of the contributions of this research to make the IB compatible with CSA. The developed RH and RD function are shown in Equations (4.6) and (4.9). It was shown in Chapter 4 that even the results of the IB method improved in accuracy by using the developed RD and RH functions. The sensitivity analysis was conducted for 1D and 2D problems using the IB method in Chapter 4 and the sensitivity analysis results were verified using the complex step method. It was shown in Chapter 4 that the accuracy of sensitivity results decay near the boundaries. This problem is addressed by reconstructing the sensitivity results using first order Taylor series expansion. The use of CSA alongside the IB method is another contribution of this research. This combines the positive features of IB method regarding robustness and cost to ease of implementation features of CSA. To the best of the author's knowledge, this work is the first implementation of CSA for continuum IB analysis.

## 6.1 Research Contribution

This dissertation demonstrates several contributions in the area of multidisciplinary sensitivity analysis for the design of systems based on coupled fluid-structure response. This technique offers a significant advantage over the traditional body conformal method for analysis and sensitivity calculation used for design. Some contributions of this work are as follows:

- A framework based on immersed boundary formulation for coupled fluid-structure interaction analysis is proposed. By using the immersed boundary method, the need for mesh deformation is removed from the simulation procedure; therefore, a more

robust framework is achieved and demonstrated for the simulation of FSI systems where the boundary shape is complex, and the structure deformations are large. The IB method is further improved by the introduction of regularized delta function for transferring data between the fluid and solid domain. This results in a smooth pressure distribution over the solid boundaries and also enables the application of continuum sensitivity analysis for the coupled sensitivity analysis.

- The analytical continuum sensitivity formulation is developed for CFD simulations based on the IB approach. The introduction of regularized delta function to the IB formulation enables the continuous differentiation of Navier-Stokes equations. Moreover, by using the continuum sensitivity analysis differential operators used in the solver are utilized without any modification. This methodology enables accurate and rapid sensitivity calculated from pressure and velocity fields of the fluid domain with respect to structure shape. Comparison with complex step results proved the accuracy of sensitivity results calculated with this approach.
- A fully coupled multidisciplinary sensitivity analysis is achieved by coupling and differentiating a transient finite element structural solver alongside the CFD simulation. Using this approach, the transient sensitivity response of various coupled fluid-structure interaction systems are investigated. These results can be used in the design of such complex systems.

## 6.2 Future Work

This work proposes a new methodology based on continuum sensitivity analysis and immersed boundary method for the analytical sensitivity analysis of coupled fluid-structure interaction systems. The future accomplishments required in this research are as follows:

- In this work, it is assumed that the solid boundary is defined analytically using a cou-

ple of control parameters. This enables the analytical differentiation of the boundary shape for the IB method. However, this is not always possible. It is more desired to have a general approach for defining the boundary shape. This is also desirable to the optimization process since arbitrary change becomes possible. We are proposing to use the level-set method for determining the boundaries and calculating the boundary sensitivities required for sensitivity analysis using the IB method. The level set models can easily represent complex boundaries that can form holes, split into multiple pieces, or merge with others to form a single one.

- Incorporation of compressible flow simulation is another avenue for the future work in this area. Many of cases such as aircraft design are better represented with the compressible flow assumptions.
- All the sensitivity analysis done in this work was based on the direct sensitivity formulation. This formulation is useful where the number of design variables is less than the number of functions that are differentiated. For the case where the functions are less than design variables, the adjoint method is more applicable. The continuous adjoint derivation for implementation using the IB method is required.

# Bibliography

- [1] Sridhar, B., Ng, H., and Chen, N., “Aircraft trajectory optimization and contrails avoidance in the presence of winds,” *Journal of Guidance, Control, and Dynamics*, Vol. 34, No. 5, 2011, pp. 1577–1584.
- [2] Han, Z.-H., Götz, S., and Zimmermann, R., “Improving variable-fidelity surrogate modeling via gradient-enhanced kriging and a generalized hybrid bridge function,” *Aerospace Science and Technology*, Vol. 25, No. 1, 2013, pp. 177–189.
- [3] Pettit, C. L., “Uncertainty quantification in aeroelasticity: recent results and research challenges,” *Journal of Aircraft*, Vol. 41, No. 5, 2004, pp. 1217–1229.
- [4] Sobiesczanski-Sobieski, J. and Haftka, R. T., “Multidisciplinary aerospace design optimization: survey of recent developments,” *Structural optimization*, Vol. 14, No. 1, 1997, pp. 1–23.
- [5] Martins, J. R., Sturdza, P., and Alonso, J. J., “The complex-step derivative approximation,” *ACM Transactions on Mathematical Software (TOMS)*, Vol. 29, No. 3, 2003, pp. 245–262.
- [6] Naumann, U., *The art of differentiating computer programs: an introduction to algorithmic differentiation*, Vol. 24, Siam, 2012.

- [7] Choi, K. K. and Kim, N.-H., *Structural sensitivity analysis and optimization 1: linear systems*, Springer Science & Business Media, 2006.
- [8] Vanderplaats, G., *Numerical optimization techniques for engineering design: with applications*, McGraw-Hill Series in Mechanical Engineering, McGraw-Hill Ryerson, Limited, 1984.
- [9] Arora, J. S. and Haug, E. J., “Methods of design sensitivity analysis in structural optimization,” *AIAA journal*, Vol. 17, No. 9, 1979, pp. 970–974.
- [10] Reuther, J. J., Jameson, A., Alonso, J. J., Rimlinger, M. J., and Saunders, D., “Constrained multipoint aerodynamic shape optimization using an adjoint formulation and parallel computers, part 2,” *Journal of aircraft*, Vol. 36, No. 1, 1999, pp. 61–74.
- [11] Martins, J. R., Alonso, J. J., and Reuther, J. J., “A coupled-adjoint sensitivity analysis method for high-fidelity aero-structural design,” *Optimization and Engineering*, Vol. 6, No. 1, 2005, pp. 33–62.
- [12] Newman, J. C., Taylor, A. C., and Barnwell, R. W., *Aerodynamic shape sensitivity analysis and design optimization of complex configurations using unstructured grids*, National Aeronautics and Space Administration, 1997.
- [13] Morris, A., Allen, C., and Rendall, T., “CFD-based optimization of aerofoils using radial basis functions for domain element parameterization and mesh deformation,” *International journal for numerical methods in fluids*, Vol. 58, No. 8, 2008, pp. 827–860.
- [14] Jameson, A., Shankaran, S., Martinelli, L., and Haimes, B., “Aerodynamic Shape Optimization of Complete Aircraft Configurations using Unstructured Grids,” *42nd AIAA Aerospace Sciences Meeting and Exhibit*, AIAA 2004-533, 2004.

- [15] Gamboa, P., Vale, J., P. Lau, F., and Suleman, A., “Optimization of a morphing wing based on coupled aerodynamic and structural constraints,” *AIAA journal*, Vol. 47, No. 9, 2009, pp. 2087–2104.
- [16] Pandya, M. J. and Baysal, O., “Gradient-based aerodynamic shape optimization using alternating direction implicit method,” *Journal of aircraft*, Vol. 34, No. 3, 1997, pp. 346–352.
- [17] Kim, H.-J., Sasaki, D., Obayashi, S., and Nakahashi, K., “Aerodynamic optimization of supersonic transport wing using unstructured adjoint method,” *AIAA journal*, Vol. 39, No. 6, 2001, pp. 1011–1020.
- [18] Lyu, Z. and Martins, J. R., “Aerodynamic design optimization studies of a blended-wing-body aircraft,” *Journal of Aircraft*, Vol. 51, No. 5, 2014, pp. 1604–1617.
- [19] Haftka, R. T. and Adelman, H. M., “Recent developments in structural sensitivity analysis,” *Structural optimization*, Vol. 1, No. 3, 1989, pp. 137–151.
- [20] Borggaard, J. and Burns, J., “A PDE sensitivity equation method for optimal aerodynamic design,” *Journal of Computational Physics*, Vol. 136, No. 2, 1997, pp. 366–384.
- [21] Hristova, H., Etienne, S., Pelletier, D., and Borggaard, J., “A continuous sensitivity equation method for time-dependent incompressible laminar flows,” *International Journal for numerical methods in fluids*, Vol. 50, No. 7, 2006, pp. 817–844.
- [22] Cross, D. M. and Canfield, R. A., “Local continuum shape sensitivity with spatial gradient reconstruction,” *Structural and Multidisciplinary Optimization*, Vol. 50, No. 6, 2014, pp. 975–1000.
- [23] Arora, J. and Haug, E., “Methods of Design Sensitivity Analysis in Structural Optimization,” *AIAA Journal*, Vol. 17, No. 9, 1979, pp. 970–974.

- [24] Dems, K. and Mroz, Z., “Variational approach to first- and second-order sensitivity analysis of elastic structures,” *International Journal for Numerical Methods in Engineering*, Vol. 21, No. 4, 1985, pp. 637–661.
- [25] Jameson, A., “Aerodynamic design via control theory,” *Journal of scientific computing*, Vol. 3, No. 3, 1988, pp. 233–260.
- [26] Borggaard, J. and Burns, J., *A sensitivity equation approach to shape optimization in fluid flows*, Springer, 1995.
- [27] Stanley, L. G. D. and Stewart, D. L., *Design Sensitivity Analysis: Computational Issues of Sensitivity Equation Methods*, Frontiers in applied mathematics, Society for Industrial and Applied Mathematics (SIAM, 3600 Market Street, Floor 6, Philadelphia, PA 19104), 2002.
- [28] Etienne, S. and Pelletier, D., “A general approach to sensitivity analysis of fluid–structure interactions,” *Journal of Fluids and Structures*, Vol. 21, No. 2, 2005, pp. 169–186.
- [29] Liu, S. and Canfield, R. A., “Equivalence of continuum and discrete analytic sensitivity methods for nonlinear differential equations,” *Structural and Multidisciplinary Optimization*, Vol. 48, No. 6, 2013, pp. 1173–1188.
- [30] Sahin, M. and Mohseni, K., “An arbitrary Lagrangian–Eulerian formulation for the numerical simulation of flow patterns generated by the hydromedusa *Aequorea victoria*,” *Journal of Computational Physics*, Vol. 228, No. 12, 2009, pp. 4588–4605.
- [31] Liu, S. and Canfield, R. A., “Boundary velocity method for continuum shape sensitivity of nonlinear fluidstructure interaction problems,” *Journal of Fluids and Structures*, Vol. 40, No. 0, 2013, pp. 284 – 301.

- [32] Peskin, C. S., “Numerical analysis of blood flow in the heart,” *Journal of computational physics*, Vol. 25, No. 3, 1977, pp. 220–252.
- [33] Anderson, J. D. and Wendt, J., *Computational fluid dynamics*, Vol. 206, Springer, 1995.
- [34] Saiki, E. and Biringen, S., “Numerical simulation of a cylinder in uniform flow: application of a virtual boundary method,” *Journal of Computational Physics*, Vol. 123, No. 2, 1996, pp. 450–465.
- [35] Zhu, L. and Peskin, C. S., “Interaction of two flapping filaments in a flowing soap film,” *Physics of Fluids (1994-present)*, Vol. 15, No. 7, 2003, pp. 1954–1960.
- [36] Beyer, R. P. and LeVeque, R. J., “Analysis of a one-dimensional model for the immersed boundary method,” *SIAM Journal on Numerical Analysis*, Vol. 29, No. 2, 1992, pp. 332–364.
- [37] Peskin, C. S. and McQueen, D. M., “A three-dimensional computational method for blood flow in the heart I. Immersed elastic fibers in a viscous incompressible fluid,” *Journal of Computational Physics*, Vol. 81, No. 2, 1989, pp. 372–405.
- [38] Fauci, L. J. and Peskin, C. S., “A computational model of aquatic animal locomotion,” *Journal of Computational Physics*, Vol. 77, No. 1, 1988, pp. 85–108.
- [39] Kempe, T., Lennartz, M., Schwarz, S., and Fröhlich, J., “Imposing the free-slip condition with a continuous forcing immersed boundary method,” *Journal of Computational Physics*, Vol. 282, 2015, pp. 183–209.
- [40] Uhlmann, M., “An immersed boundary method with direct forcing for the simulation of particulate flows,” *Journal of Computational Physics*, Vol. 209, No. 2, 2005, pp. 448–476.

- [41] Mittal, R. and Iaccarino, G., “Immersed boundary methods,” *Annual Review of Fluid Mechanics*, Vol. 37, 2005, pp. 239–261.
- [42] Goldstein, D., Handler, R., and Sirovich, L., “Modeling a no-slip flow boundary with an external force field,” *Journal of Computational Physics*, Vol. 105, No. 2, 1993, pp. 354–366.
- [43] Durlofsky, L. and Brady, J., “Analysis of the Brinkman equation as a model for flow in porous media,” *Physics of Fluids*, Vol. 30, No. 11, 1987, pp. 3329–3341.
- [44] Arquis, E. and Caltagirone, J., “Sur les conditions hydrodynamiques au voisinage dune interface milieu fluide-milieu poreux: applicationa la convection naturelle,” *Comptes Rendus de l’Acadmie des Sciences Paris II*, Vol. 299, 1984, pp. 1–4.
- [45] Angot, P., “Analysis of singular perturbations on the Brinkman problem for fictitious domain models of viscous flows,” *Mathematical methods in the applied sciences*, Vol. 22, No. 16, 1999, pp. 1395–1412.
- [46] Gazzola, M., Chatelain, P., Van Rees, W. M., and Koumoutsakos, P., “Simulations of single and multiple swimmers with non-divergence free deforming geometries,” *Journal of Computational Physics*, Vol. 230, No. 19, 2011, pp. 7093–7114.
- [47] Kevlahan, N. K.-R. and Ghidaglia, J.-M., “Computation of turbulent flow past an array of cylinders using a spectral method with Brinkman penalization,” *European Journal of Mechanics-B/Fluids*, Vol. 20, No. 3, 2001, pp. 333–350.
- [48] Mohd-Yusof, J., “Combined immersed-boundary/B-spline methods for simulations of ow in complex geometries,” *Annual Research Briefs*, 1997, pp. 317–327.
- [49] Verzicco, R., Mohd-Yusof, J., Orlandi, P., and Haworth, D., “LES in complex geometries using boundary body forces,” *Center for Turbulence Research, Proceedings of the Summer Program, Stanford University*, 1998, pp. 171–186.

- [50] Verzicco, R., Fatica, M., Iaccarino, G., Moin, P., and Khalighi, B., “Large eddy simulation of a road vehicle with drag-reduction devices,” *AIAA journal*, Vol. 40, No. 12, 2002, pp. 2447–2455.
- [51] Iaccarino, G. and Verzicco, R., “Immersed boundary technique for turbulent flow simulations,” *Applied Mechanics Reviews*, Vol. 56, No. 3, 2003, pp. 331–347.
- [52] Clarke, D. K., Hassan, H., and Salas, M., “Euler calculations for multielement airfoils using Cartesian grids,” *AIAA journal*, Vol. 24, No. 3, 1986, pp. 353–358.
- [53] Kirkpatrick, M., Armfield, S., and Kent, J., “A representation of curved boundaries for the solution of the Navier–Stokes equations on a staggered three-dimensional Cartesian grid,” *Journal of Computational Physics*, Vol. 184, No. 1, 2003, pp. 1–36.
- [54] Hu, X., Khoo, B., Adams, N. A., and Huang, F., “A conservative interface method for compressible flows,” *Journal of Computational Physics*, Vol. 219, No. 2, 2006, pp. 553–578.
- [55] Udaykumar, H., Mittal, R., and Shyy, W., “Computation of solid–liquid phase fronts in the sharp interface limit on fixed grids,” *Journal of computational physics*, Vol. 153, No. 2, 1999, pp. 535–574.
- [56] Borrvall, T. and Petersson, J., “Topology optimization of fluids in Stokes flow,” *International journal for numerical methods in fluids*, Vol. 41, No. 1, 2003, pp. 77–107.
- [57] Challis, V. J. and Guest, J. K., “Level set topology optimization of fluids in Stokes flow,” *International journal for numerical methods in engineering*, Vol. 79, No. 10, 2009, pp. 1284–1308.
- [58] Deaton, J. D. and Grandhi, R. V., “A survey of structural and multidisciplinary continuum topology optimization: post 2000,” *Structural and Multidisciplinary Optimization*, Vol. 49, No. 1, 2014, pp. 1–38.

- [59] LeVeque, R. J. and Li, Z., “Immersed interface methods for Stokes flow with elastic boundaries or surface tension,” *SIAM Journal on Scientific Computing*, Vol. 18, No. 3, 1997, pp. 709–735.
- [60] Pingen, G., Evgrafov, A., and Maute, K., “Topology optimization of flow domains using the lattice Boltzmann method,” *Structural and Multidisciplinary Optimization*, Vol. 34, No. 6, 2007, pp. 507–524.
- [61] Gobal, K., Grandhi, R. V., and Kolonay, R. M., “Continuum Sensitivity Analysis for Structural Shape Design Variables Using Finite-Volume Method,” *AIAA Journal*, Vol. 53, No. 2, 2014, pp. 347–355.
- [62] Mase, G. T., Smelser, R. E., and Mase, G. E., *Continuum mechanics for engineers*, CRC press, 2009.
- [63] Haftka, R. T. and Grandhi, R. V., “Structural shape optimizationa survey,” *Computer Methods in Applied Mechanics and Engineering*, Vol. 57, No. 1, 1986, pp. 91–106.
- [64] Dowding, K. J. and Blackwell, B. F., “Sensitivity analysis for nonlinear heat conduction,” *Journal of Heat Transfer*, Vol. 123, No. 1, 2001, pp. 1–10.
- [65] Szopa, R., Siedlecki, J., and Wojciechowska, W., “Second order sensitivity analysis of heat conduction problems,” *Scientific Research of the Institute of Mathematics and Computer Science*, Vol. 4, No. 1, 2005, pp. 255–263.
- [66] Sorli, K. and Skaar, I. M., “Sensitivity Analysis For Thermal Design And Monitoring Problems Of Refractories,” Begel House Inc., April 19-24, 2004, Norway.
- [67] Szabo, B. A. and Babuška, I., *Finite element analysis*, John Wiley & Sons, 1991.
- [68] Wickert, D. P., “Least-squares, continuous sensitivity analysis for nonlinear fluid-structure interaction,” Tech. rep., DTIC Document, 2009.

- [69] Deaton, J. D. and Grandhi, R. V., “Stiffening of restrained thermal structures via topology optimization,” *Structural and Multidisciplinary Optimization*, Vol. 48, No. 4, 2013, pp. 731–745.
- [70] Jain, A., Jones, N. P., and Scanlan, R. H., “Coupled flutter and buffeting analysis of long-span bridges,” *Journal of Structural Engineering*, 1996.
- [71] Arrigan, J., Pakrashi, V., Basu, B., and Nagarajaiah, S., “Control of flapwise vibrations in wind turbine blades using semi-active tuned mass dampers,” *Structural Control and Health Monitoring*, Vol. 18, No. 8, 2011, pp. 840–851.
- [72] Farhat, C., Van der Zee, K. G., and Geuzaine, P., “Provably second-order time-accurate loosely-coupled solution algorithms for transient nonlinear computational aeroelasticity,” *Computer methods in applied mechanics and engineering*, Vol. 195, No. 17, 2006, pp. 1973–2001.
- [73] Sotiropoulos, F. and Borazjani, I., “A review of state-of-the-art numerical methods for simulating flow through mechanical heart valves,” *Medical & biological engineering & computing*, Vol. 47, No. 3, 2009, pp. 245–256.
- [74] Kern, S. and Koumoutsakos, P., “Simulations of optimized anguilliform swimming,” *Journal of Experimental Biology*, Vol. 209, No. 24, 2006, pp. 4841–4857.
- [75] Lomtev, I., Kirby, R., and Karniadakis, G., “A discontinuous Galerkin ALE method for compressible viscous flows in moving domains,” *Journal of Computational Physics*, Vol. 155, No. 1, 1999, pp. 128–159.
- [76] Farhat, C., “CFD-based nonlinear computational aeroelasticity,” *Encyclopedia of computational mechanics*, Vol. 3, 2004, pp. 459–480.

- [77] Cheng, Y., Oertel, H., and Schenkel, T., “Fluid-structure coupled CFD simulation of the left ventricular flow during filling phase,” *Annals of biomedical engineering*, Vol. 33, No. 5, 2005, pp. 567–576.
- [78] Majumdar, S., Iaccarino, G., and Durbin, P., “RANS solvers with adaptive structured boundary non-conforming grids,” *Annual Research Briefs, Center for Turbulence Research, Stanford University*, 2001, pp. 353–466.
- [79] Peskin, C. S., “Flow patterns around heart valves: a numerical method,” *Journal of computational physics*, Vol. 10, No. 2, 1972, pp. 252–271.
- [80] Lee, C., “Stability characteristics of the virtual boundary method in three-dimensional applications,” *Journal of Computational Physics*, Vol. 184, No. 2, 2003, pp. 559–591.
- [81] Shin, S. J., Huang, W.-X., and Sung, H. J., “Assessment of regularized delta functions and feedback forcing schemes for an immersed boundary method,” *International Journal for Numerical Methods in Fluids*, Vol. 58, No. 3, 2008, pp. 263–286.
- [82] Roma, A. M., Peskin, C. S., and Berger, M. J., “An adaptive version of the immersed boundary method,” *Journal of computational physics*, Vol. 153, No. 2, 1999, pp. 509–534.
- [83] Peskin, C. S., “The immersed boundary method,” *Acta numerica*, Vol. 11, 2002, pp. 479–517.
- [84] Kreissl, S., Pinggen, G., and Maute, K., “An explicit level set approach for generalized shape optimization of fluids with the lattice Boltzmann method,” *International Journal for Numerical Methods in Fluids*, Vol. 65, No. 5, 2011, pp. 496–519.

- [85] Cross, D. M. and Canfield, R. A., “Local continuum shape sensitivity with spatial gradient reconstruction for nonlinear analysis,” *Structural and Multidisciplinary Optimization*, Vol. 51, No. 4, 2015, pp. 849–865.
- [86] Kamaraju, V. and Narasimham, R., *Linear Systems: Analysis And Applications, Second Edition*, I.K. International Publishing House Pvt. Limited, 2009.
- [87] Michler, C., Hulshoff, S., Van Brummelen, E., and De Borst, R., “A monolithic approach to fluid–structure interaction,” *Computers & fluids*, Vol. 33, No. 5, 2004, pp. 839–848.
- [88] Hu, H. H., Patankar, N. A., and Zhu, M., “Direct numerical simulations of fluid–solid systems using the arbitrary Lagrangian–Eulerian technique,” *Journal of Computational Physics*, Vol. 169, No. 2, 2001, pp. 427–462.
- [89] Van Loon, R., Anderson, P., Van de Vosse, F., and Sherwin, S., “Comparison of various fluid–structure interaction methods for deformable bodies,” *Computers & structures*, Vol. 85, No. 11, 2007, pp. 833–843.
- [90] Chen, S.-S., *Flow-induced vibration of circular cylindrical structures*, Vol. 414, Hemisphere publishing corporation Washington, DC, 1987.
- [91] Jendrzejczyk, J. and Chen, S., “Fluid forces on two circular cylinders in crossflow,” Tech. rep., Argonne National Lab., 1985.
- [92] Mittal, S. and Raghuvanshi, A., “Control of vortex shedding behind circular cylinder for flows at low Reynolds numbers,” *International journal for numerical methods in fluids*, Vol. 35, No. 4, 2001, pp. 421–447.
- [93] Tuncer, I. H., Walz, R., and Platzer, M. F., “A computational study on the dynamic stall of a flapping airfoil,” *AIAA paper*, Vol. 2519, pp. AIAA 98–2519.

- [94] Shyy, W., Lian, Y., Tang, J., Liu, H., Trizila, P., Stanford, B., Bernal, L., Cesnik, C., Friedmann, P., and Ifju, P., “Computational aerodynamics of low Reynolds number plunging, pitching and flexible wings for MAV applications,” *Acta Mechanica Sinica*, Vol. 24, No. 4, 2008, pp. 351–373.
- [95] Tuncer, I. H. and Platzer, M. F., “Computational study of flapping airfoil aerodynamics,” *Journal of Aircraft*, Vol. 37, No. 3, 2000, pp. 514–520.
- [96] Lian, Y., Ol, M. V., and Shyy, W., “Comparative study of pitch-plunge airfoil aerodynamics at transitional reynolds number,” *AIAA paper*, Vol. 652, pp. AIAA 2008–652.
- [97] Webb, C., Dong, H., and Ol, M., “Effects of unequal pitch and plunge airfoil motion frequency on aerodynamic response,” *46th AIAA Aerospace Sciences Meeting and Exhibit*, 2008, pp. AIAA Paper 2008–582.
- [98] Luersen, M., Le Riche, R., Lemosse, D., and Le Maître, O., “A computationally efficient approach to swimming monofin optimization,” *Structural and Multidisciplinary Optimization*, Vol. 31, No. 6, 2006, pp. 488–496.
- [99] Allen, J. and Smits, A., “Energy harvesting eel,” *Journal of fluids and structures*, Vol. 15, No. 3, 2001, pp. 629–640.
- [100] Shen, L., Zhang, X., Yue, D. K., and Triantafyllou, M. S., “Turbulent flow over a flexible wall undergoing a streamwise travelling wave motion,” *Journal of Fluid Mechanics*, Vol. 484, 2003, pp. 197–221.
- [101] Kim, Y. and Peskin, C. S., *Penalty immersed boundary method for an elastic boundary with mass*, Vol. 19, AIP Publishing, 2007.